UNIVERSITY OF LONDON THESIS

Degree PhD Year 2007 Name of Author BENEDETTINI Milena

The structure and the origin of the molecular gas along chemically rich outflows

Milena Benedettini

Thesis submitted for the Degree of Doctor of Philosophy
of the University of London

Department of Physics & Astronomy
UNIVERSITY COLLEGE LONDON

November 2006

ProQuest LLC
789 East Eisenhower Parkway
P.O. Box 1346
Ann Arbor, MI 48106-1346

I, Milena Benedettini, confirm that the work presented in this thesis is my own. Where information has been derived from other sources, I confirm that this has been indicated in the thesis.

Abstract

Bipolar outflows are ubiquitously present in Young Stellar Objects. They are the mechanism through which the accreting central object loses the excessive angular momentum and they play a major role in stopping the gravitational collapse and probably in fixing the final mass of the forming star. A few outflows show a rich molecular emission characterized by small ($d \leq 0.1$ pc), low velocity ($v \leq 10$km s^{-1}) clumps. The aim of this thesis is to investigate the origin and the nature of the low velocity molecular clumps by the use of a chemical model that simulates the clump formation and its subsequent interaction with the outflow, coupled with a radiative transfer model that reproduces the line profile for a direct comparison with the observations.

Different scenarios for the formation of the clumps have been investigated within a large range of physical conditions. The models have been compared with single dish observations of the clumps observed along the CB3 and L1157 outflows. The best models are those where the clump is formed, at least partially, before the advent of the outflow; with the advent of the outflow the clump undergoes a short period of non-dissociative shock and the consequent release of the icy mantle, together with the high temperature chemistry, leads to the observed chemical enrichment.

The structure of the molecular gas has also been investigated with high spatial resolution observations carried out with the Plateau de Bure Interferometer. The interferometric data confirm the results of the previous analysis: what is seen as a single molecular clump with size ≤ 0.1 pc by the single dish telescope when observed at high resolution is in fact a complex structure with sub–clumps of the order of 0.02 pc different both in the physical conditions and their chemical composition.

Acknowledgements

For me it is always difficult to express with words my feelings and the fact that I must use English does not help. However, I will try to acknowledge with simple words all the people that helped me to reach this point.

The first and biggest thank is to my supervisor, Serena Viti, for her constant support in these years. Despite the physical distance she has been always present when I needed her help. Our discussions have always been so instructive and and helpful that led me to have a clearer vision of the work. I am particularly grateful to her because she has done much more than her duty as supervisor such as hosting me during my visits in London (thanks also to Kaj) and taking care of some of the administrative matters.

I am indebted to Jeremy Yates for having provided me with his radiative transfer code; he was always willing to introduce in the code all the changes needed for my work. A similar thanks go to Claudio Codella for having provided me with the data of the CB3 outflow and for having answered to all my emails full of questions. Without their contribution this work would not have been possible. I am grateful to Rafael Bachiller for the Plateau de Bure data of the L1157 outflow that are precious to continue the work started in this thesis. An acknowledgment also go to Mike Barlow and David Williams for their helpful suggestions and kindness during our meetings.

I acknowledge Erina for helping me to convert some figures of the thesis in the right format and Stefano for his precious suggestions on how to use LaTeX.

Infine voglio ringraziare la tutta la mia famiglia perché hanno sempre condiviso le mie scelte incoragiandomi con il loro amore. Grazie Francesco perché mi aiuti a credere nel mio lavoro anche nei momenti di scoraggiamento.

Contents

List of Tables

List of Figures

Chapter 1

Introduction

1.1 Overview

Stars form in the dense cores of molecular clouds by the gravitational collapse of matter on a central accreting object. The dense envelope that surrounds the forming star prevents the possibility to directly observe it. We can only see the external dusty envelope or the large, powerful bipolar outflow driven by the obscured protostar. These mainly emit at infrared and millimetre wavelengths, a spectral range that is largely not accessible from the ground due to atmospheric absorption. Direct observations of star formation processes have become possible only in the last decades of the last century when the first near–infrared telescopes were built and the first infrared satellite (IRAS) was put in orbit. Since then a theory of the star formation process has been developed for isolated, low–mass stars. However, despite the enormous progresses done in the last few years, some of the most basic questions are still unanswered. In particular, the very early phases of star formation when both the infall and outflow processes are activated, are still poorly understood.

The project I carry out during my PhD deals with the study of chemically rich outflows. Outflows have a key role in the star formation process since they are the mechanism through which the accreting protostar loses the exceeding angular momentum and they plays a major role in stopping the gravitational collapse and fixing the final mass of the forming star.

The aim of this thesis is to develop a detailed physical and chemical model

to investigate the origin and the nature of the low-velocity, chemically rich molecular clumps associated with some low- and intermediate-mass protostellar objects. I will use a chemical model to simulate the clump formation and its interaction with the outflow. The aim is to determine whether those clumps are a direct consequence of the presence of the outflow or if they are pre-existing. The chemical model will then been coupled with a radiative transfer model that reproduces line profiles to directly compare with single dish and interferometric observations. In particular, I will analyze the clumps along the two outflows CB3 and L1157, for which extensive chemical investigation is on its way.

Understanding the nature of these clumps may have wider implications than just constraining their origin: there is now strong evidence, both observational and theoretical, that molecular clouds are clumpy on a scale of ~ 0.01 pc, and that most of these clumps dissipate, or are destroyed, on a timescale on the order of 10^6 yr (Falle & Hartquist, 2002). These clumps are generally too small to be detected in single dish studies, but they can be resolved in array telescope observations (e.g. Morata et al. 2003). If the pre-existing nature of the low velocity clumps observed along outflows is correct, they may indeed be a further evidence of the clumpiness of dark molecular clouds.

The structure of the thesis is as the follow. In this chapter I briefly describe the star formation process and the classification of Young Stellar Objects (YSO). In particular, I focus on the description of outflows: how they are observed, how the main physical parameters are derived, how they are driven, how their observational properties evolve with time. The main chemical processes at work in the shocked medium of the outflows are presented and the small molecular clumps along the outflow lobes are described. In Chapter 2 I present the chemical and the radiative transfer models used in the analysis. After a presentation of the general characteristic of these models, I describe in detail the two codes that are used: the UCL chemical model and the SMMOL radiative transfer model. In Chapter 3 the two scenarios for the clumps formation are described and molecular column densities are derived by use only of the chemical models. The results are compared with the column densities of molecular species observed with the IRAM-30m telescope in the clumps associ-

ated with the CB3 and L1157 outflows. A preliminary characterization of the physical and chemical structure of the clumps is then presented. In Chapter 4 the chemical model is coupled with the radiative transfer model in order to derive theoretical line profiles that are compared directly with the observed lines. The detailed modelling of the S1 clump along CB3 is presented and some conclusions about the structure and the formation of the low–velocity molecular clumps are derived. In Chapter 5 I present high spatial resolution observations of the B1 clump along the L1157 outflow carried out with the Plateau de Bure interferometer. These observations allow to investigate the small–scale structure of the clumps and to verify the hypothesis about the substructures present in the size implied by the single dish observations used in the previous analysis. In Chapter 6 I present the work done as preparatory science for the Herschel mission. Herschel is the European Space Agency far–infrared and sub–millimetre satellite that will be launched in 2008. Three projects on star formation where I have contributed are briefly described. In Chapter 7 the main conclusions are given and finally I describe the future work that will be done for the modelling of the interferometric observations of the clumps in the L1157 outflow.

1.2 How stars form

Star forms in Giant Molecular Clouds (GMCs). GMCs are condensations of gas and dust extended few tens of parsecs and located mainly along the galactic plane (Mizuno et al. 1994; Myers 1995). The distribution of matter inside the GMC is highly non uniform. Although the mean density is $\sim 10^2$ cm^{-3}, about 10% of the gas is concentrated in small, dense cores with density $\sim 10^4$ cm^{-3} and size ~ 0.1 pc (Benson & Myers 1989; Jijina et al. 1999). The process that from the diffuse gas of the GMC leads to the formation of a collapsing core is still unknown. In a schematic view we know that the gravitational collapse starts when the mass of the dense core is higher than a critical value called Jeans mass

$$M_J \propto G^{-3/2} a^3 \rho^{-1/2} \tag{1.1}$$

where G is the gravitational constant, ρ is the mean density and a is the sound speed $a = (kT/m)^{1/2}$. If only gravity is acting on the gas the typical time scale for the collapse in the GMC is the free-fall time

$$t_{ff} = \left(\frac{3\pi}{32G\rho}\right)^{1/2} \tag{1.2}$$

For typical mass $M \sim 10^4 - 10^5$ $M_\odot$ and size $R \sim 5 - 20$ pc, the free fall time of the GMC is $\leq 10^5$ yr. If all molecular gas collapsed on such time scales then the rate of star formation would be $\dot{M}_* > 100$ $M_\odot$ yr^{-1}. This value is much higher than the observed star formation rate of $2 - 3$ $M_\odot$ yr^{-1} (Myers, 1991a). This simple consideration shows that other forces in addition to gravity are acting in the GMC, delaying the collapse. Of the possible support mechanisms (rotation, magnetic field and turbulence), magnetic fields are believed to be the dominant agents to halt the collapse (McKee, 1999). In fact, the observed angular velocity of cloud cores is too small to halt the collapse at an early stage, while turbulence is believed to decay on very short timescales (1–2 free–fall times), thus being unable to provide a long term support to clouds and cores.

In the molecular clouds conditions, the ionized component is frozen to the magnetic field lines and cannot collapse without dragging along the magnetic field, thus enhancing the magnetic pressure. At a certain stage, magnetic pressure balances gravity and charged particles cannot collapse. Neutral species are coupled to the ionized ones via collisions and thus are indirectly affected by the presence of a magnetic field. In the direction parallel to the magnetic lines, support against collapse can be provided by Alfven waves. For a given field strength, there exists a critical mass above which the magnetic field is not able to provide support against gravity:

$$M_{Bcr} \sim 10^3 \mathrm{M}_\odot \left(\frac{B}{30\mu\mathrm{G}}\right)\left(\frac{R}{2\mathrm{pc}}\right)^2 \tag{1.3}$$

Inside molecular clouds, the ionization fraction is maintained only by cosmic rays and natural radioactivity, since the galactic ultraviolet radiation is entirely absorbed in the outermost skin. As a result, the ionization fraction is very low ($\leq 10^{-7}$, Guellin et al. 1982; Wootten et al. 1982), and the ion–neutral

collisions cannot completely prevent the neutral gas from drifting toward the core center. This process is called ambipolar diffusion (Mestel & Spitzer, 1956) and allows the cloud to contract up to the point when the central regions become magnetically supercritical and can collapse dynamically (Nakano 1979; Lizano & Shu 1989). These inner regions are characterized by a density distribution that closely resembles that of a singular isothermal sphere ($\rho \sim r^{-2}$). Once gravitational collapse starts, it quickly expands outward to encompass the entire core. Such inside-out collapse of a singular isothermal sphere can be computed semi-analytically (Shu, 1977) and the main results are that the collapse wave expands at the sound speed $a = (kT/m)^{1/2}$, and that the average mass accretion rate onto the central object is given by

$$\dot{M} = ma^3/G \tag{1.4}$$

In the conditions typical of dense cores, $\dot{M}$ has a numerical value of $\leq 10^{-5}$ $M_{\odot}yr^{-1}$.

Once the dense cores are formed, the conditions for gravitational collapse are more easily established. At this stage, however, the core rotation can no longer be neglected and it plays an important role in the future evolution. In fact, the collapsing material has a specific angular momentum that does not allow a direct accretion onto the central protostar, but instead it accretes on a small circumstellar disk that quickly expands in time (Mundy et al., 2000). However, in order to reach the central protostar, matter has to lose the excess angular momentum. This can be achieved in the accretion disk through a variety of processes: viscosity, MHD instabilities and ejection of material in a wind. The first two processes allow angular momentum transfer to the outer radii of the disk and a corresponding mass transport towards the inner regions close to the star. The last process removes angular momentum by ejecting out of the disk plane matter with high specific angular momentum, allowing material with low angular momentum to move towards the inner regions. The violent ejection of matter along the rotation axis give rise to bipolar outflows (Richer et al., 2000).

1.3 Classification of pre–Main Sequence Objects

During the first stages of star formation the protostar is deeply embedded in the molecular cloud and thus it is not directly observable. We can only see the light reprocessed from the dusty envelope. As the evolution continues, the combined action of the accretion along the disk and the ejection along the outflow disperses the circumstellar envelope and the star becomes visible first in the infrared and then in the optical with a spectrum similar to that of a star with an excess at infrared wavelengths due to the protoplanetary disk.

The evolutionary status of pre–Main Sequence (PMS) objects can thus not be derived by directly observing the stellar radiation. On the other hand, it can be estimated indirectly by observing the continuum, atomic and molecular emission of the circumstellar envelope or/and of the outflow. At the typical temperatures of PMS objects (T = 30 – 80 K) the dust emission peaks in the far infrared (FIR) between 50 – 200 μm. The warm circumstellar envelope is predicted to emit a rich FIR spectrum (Ceccarelli et al., 1996) where the prominent features are the water and carbon monoxide rotational lines and the atomic oxygen fine structure lines. Since most of the emission falls in the FIR (inaccessible from the ground), observations of PMS objects is a recent branch of astronomy, mainly linked to the advent of infrared telescopes such as IRAS and ISO (Infrared Space Observatory).

So far, the methods commonly used to classify PMS objects have been mainly based on the characterization of the shape of their spectral energy distribution (SED) at near and mid infrared wavelengths through the value of the spectral index

$$\alpha = \frac{dLog(\nu F_\nu)}{d\nu}. \tag{1.5}$$

Lada & Wilking (1984) first classified low–mass protostellar objects considering three different classes defined by the value of α in the range 2 – 10 μm (then extended to 25 μm with the IRAS mission). This classification was followed by the work of Adams et al. (1987) who associated to each class a different evolutionary stage. Successively André et al. (1993) introduced a new class of objects still younger than the previous classes. The net result of all these

works is the classification of low–mass PMS sources in four different classes (see Fig. 1.1); proceeding from the younger to the older they are:

- **Class 0**: since they are visible only at $\lambda > 10$ μm, the spectral index α cannot be derived. They are identified by the ratio between the sub-millimetre ($\lambda > 350$ μm) and the bolometric luminosity $L_{\rm submm}/L_{\rm bol} > 5{\times}10^{-3}$. They are newly formed protostars in the main accretion phase, when the mass of the central object is still less than that of the circumstellar material. The central source is completely obscured by the envelope. The spectrum is that of gray body with temperature $\sim$ 25 – 35 K. Strong and collimated outflows are associated with these objects which have ages $\leq 10^4$ yr.

- **Class I**: with $\alpha < 0$ between 2 and 25 μm. The spectrum steeply increases in the mid infrared due to the optically thick envelope. They represent protostars in the final phase of accretion when the stellar winds are dispersing the circumstellar envelope but usually they are not yet visible in the optical. The outflows associated with this class is usually less collimated and less energetic than those of Class 0. The typical age is between 10^5 and 10^6 yr.

- **Class II**: with $0 < \alpha < 2$ between 2 and 25 μm. The spectrum appears in the optical with an excess in the infrared due to the circumstellar disk. The infrared excess has a power law shape which is modelled with a passive disk spatially thin and optically thick where the spectral index depends on the thermal gradient. They are identified with the low–mass classical T Tauri stars and the intermediate–mass Herbig Ae/Be stars. The typical age is between 10^6 and 10^7 yr.

- **Class III**: with $\alpha > 2$ between 2 and 25 μm. The spectrum is that of a black body with a weak infrared excess due to the residual circumstellar material. These objects are approaching the Main Sequence and do not have an accretion disk or have only an optically thin disk. They are identified with the Weak T Tauri stars (WTT) and have typical age of $\geq 10^7$ yr.

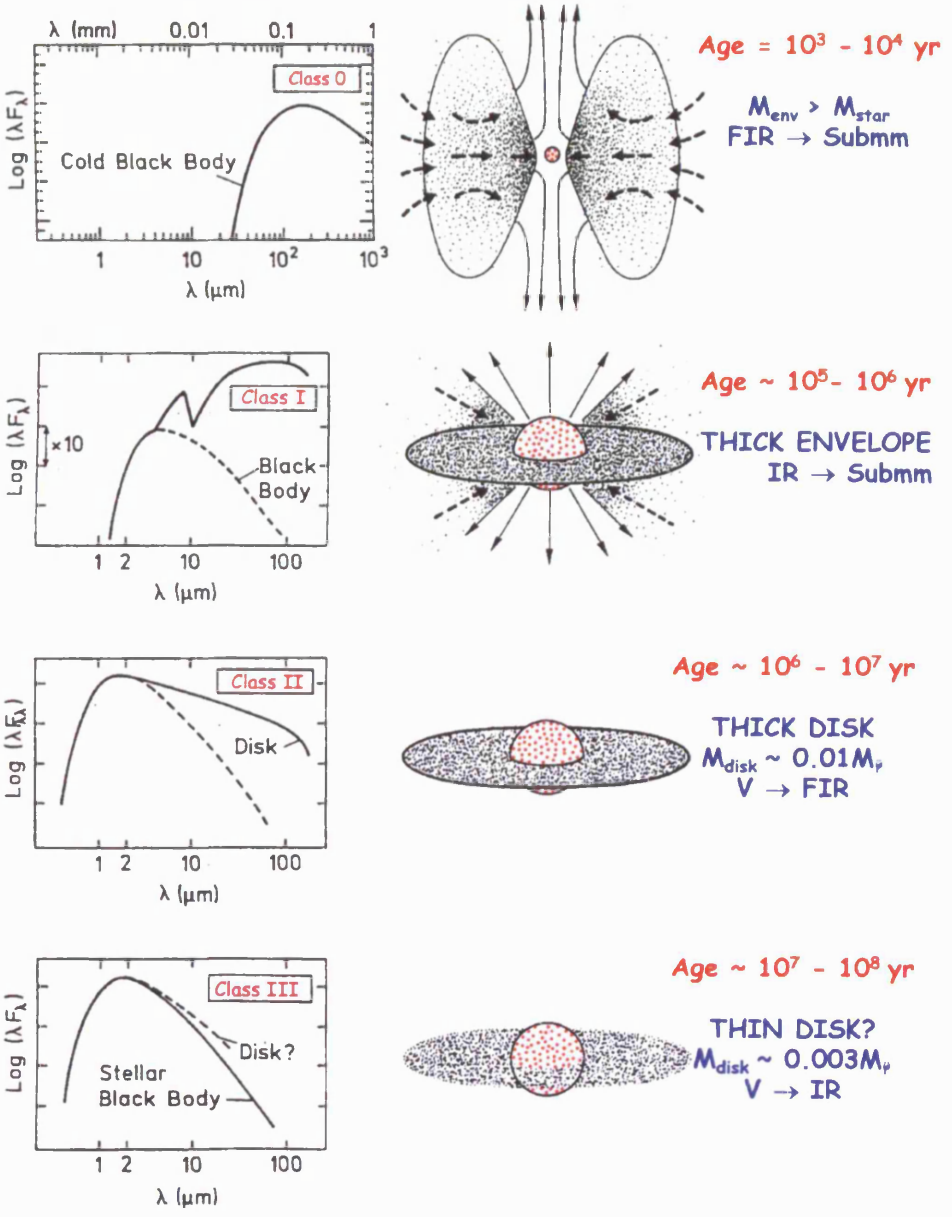

Figure 1.1: A scheme of the classification of the low–mass PMS objects, adapted from the original figure of André (1994).

1.4 High mass star formation

The scenario depicted in the previous sections does apply only to low mass stars. For stars with mass $M > 8$ $M_{\odot}$, the time scale of the accretion is longer than the time scale of the contraction so that they starts to burn hydrogen in their core while they are still accreting. At this stage the radiation pressure becomes stronger than the gravity and accretion is stopped. This means that in the classical inside out theory developed for low mass stars, massive stars could not form.

Two different scenarios have been proposed for high mass star formation. In the first scenario massive stars are formed by the coalescence of low mass stars (Bonnell & Bate, 2002). In the second one high mass stars form by accretion as low mass stars (Behren & Maeder 2001; Yorke & Sonnhalter 2002; Tan & McKee 2002) but with mass accretion rates of a couple of orders of magnitude higher ($\dot{M} \sim 10^{-5} - 10^{-3}$ $M_{\odot}yr^{-1}$) than the ones for low mass stars ($\dot{M} \sim 10^{-8} - 10^{-5}$ $M_{\odot}yr^{-1}$).

In the past there have been observational evidences in favour of both models. However recently, observations of collimated outflows tightly associated with rotating circumstellar, Keplerian disks or circumstellar, massive toroids (Cesaroni et al. 2005; Beuther et al. 2002b) as well as the development of models where the accretion through a disk or cavity eroded by the outflows leads to high mass accretion rates (Krumholz et al., 2005), strongly support the hypothesis that high–mass stars form through non–spherical accretion just as their low–mass counterparts do.

1.5 Outflows

In star formation the gravitational accretion onto the central object is associated with violent ejections of matter along the rotation axis. The material emerging from the protostar affects the surrounding molecular cloud, giving rise to bipolar lobes of accelerated material called outflows. Outflow have a key role in the star formation process since they are the mechanism through which the accreting central object loses the exceeding angular momentum. Outflows

have also a profound impact on their surroundings. Jets and winds create cavities in the parent cloud, inject energy and momentum into the surrounding clouds which in absence of massive stars may dominate the generation of the turbulence and cloud motions. The terminal shocks also drive a high temperature chemistry, thereby altering the chemical composition of the impacted medium. Outflows together with infall, contribute to disperse the parental molecular cloud, thus it is believed that it plays a major role in stopping the gravitational collapse and probably in fixing the final mass of the central object. The large size of the outflows (from 0.1 to few parsecs) makes them easily detectable, unlike infall that occurs on small scales (few hundreds of AUs) and is difficult to observe. Outflows are therefore the first observable signs that a star is born.

The first evidences of high–velocity molecular gas were discovered in the mid 70s by Zuckerman et al. (1976) and Kwan & Scoville (1976). They observed broad CO lines towards Orion KL and OMC–1, respectively. In the 80s more authors carried out systematic surveys of low mass protostars (Bally & Lada 1983; Edwards & Snell 1982; 1983; 1984) showing that outflows are ubiquitously present in YSOs since the earliest stage of the formation process. Fig. 1.2 shows a typical molecular outflow in the Class 0 protostar HH211.

1.5.1 Tracers of outflows

Flows from protostars proceed at high supersonic velocities producing strong shocks, which compress, heat and drag the ambient medium. This, in turn, cools mainly radiatively through the emission from the gas excited at different temperatures. A large range of excitation conditions and a significant chemical differentiation are present along the lobes of the outflows that thus emit over a wide range of wavelengths, from the ultraviolet to the radio. To have a comprehensive view of the outflow phenomenon a sampling of all the large range of excitation conditions along the flow is necessary. The main tracers are:

- ^{12}CO and ^{13}CO pure rotational lines in the millimetre range. They trace low temperature ($\sim$ 10 K) components and probe the large scale outflow

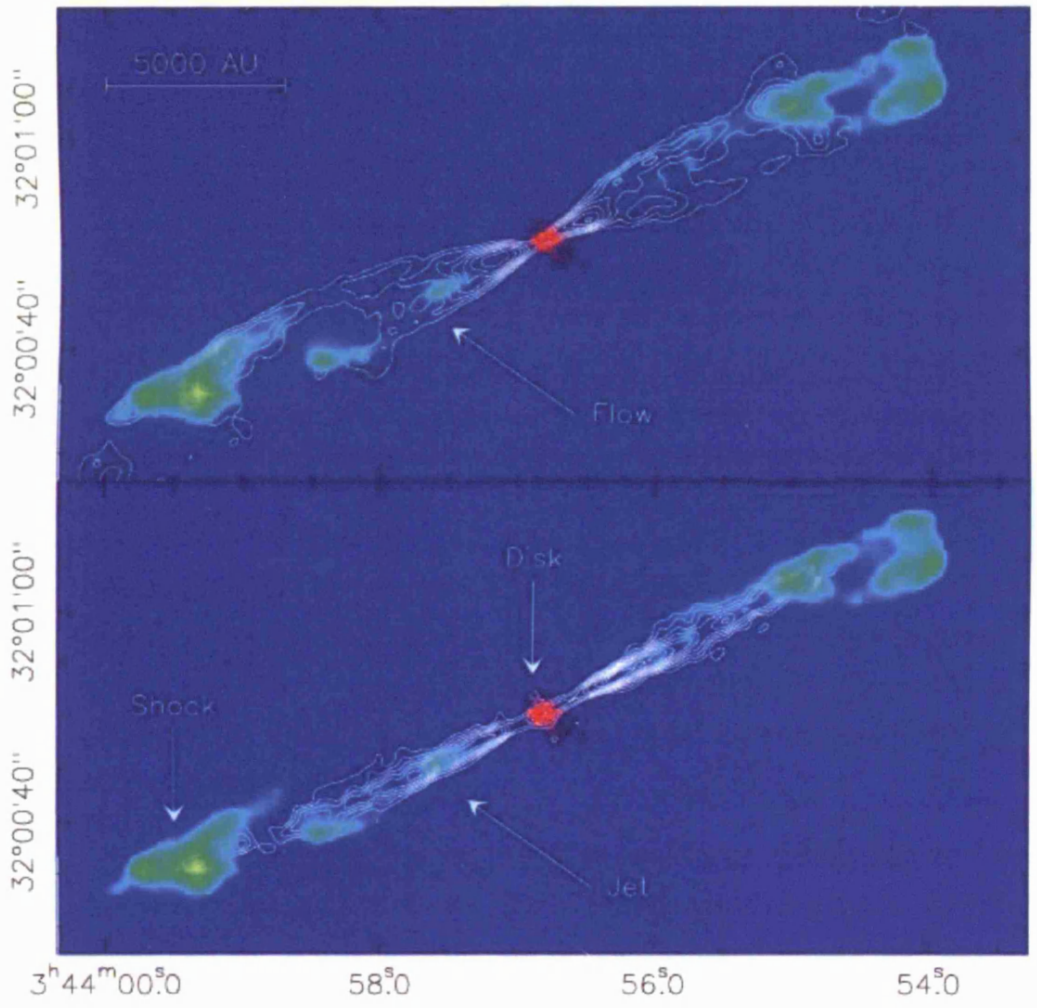

Figure 1.2: Bipolar molecular flow (top) and molecular jet (bottom) in the Class 0 source associated with HH211 (figure from Gueth & Guilloteau (1999)). The line contour plot shows the CO (2–1) emission (Gueth & Guilloteau, 1999), while the color image (in H_2 at 2.12 μm) traces the warm shock–excited gas (McCaughrean et al., 1994). The top panel shows the CO (2–1) low velocity component (v <10 km s^{-1}) and the bottom panel the high velocity component (v >10 km s^{-1}).

morphology and dynamics. The most commonly observed lines are those coming from the lowest energy transitions (J = 1 0 and J = 2 1) which are used to estimate the total mass and energy of the outflow (see Sect. 1.5.2). Molecular outflows traced by CO show a variety of shapes and sizes. Typical velocities are from few to tens of km s^{-1}.

- H_2 vibrational lines at excitation temperature of $\sim$ 2000 K and optical UV ionic emission lines at excitation temperature of $\sim 10^4$ K. They probe directly the shock front caused by the interaction of the collimated jet with the ambient medium. Jet regions with a low visual extinction are usually traced in strong optical lines such as Hα, [OI]6300, [SII]6731,6716 and [NII]6583. More embedded jets are best observed through near infrared H_2 and [FeII] transitions. Typical velocities are from tens to hundreds of km s^{-1}.

- Emission at FIR wavelengths from warm gas with excitation temperatures of 200–2000 K. The FIR spectral range is not accessible from the ground and it has been explored for the first time by the spectrometers on board ISO revealing the presence of an intermediate excited gas copiously emitting in the [OI], high-J CO, H_2O, OH lines.

- Emission of millimetre transitions from molecular species whose abundances are strongly enhanced by the shocks generated from the interaction between the supersonic flowing material and the surrounding gas (e.g. SiO, H_2S, CS, SO, CH_3OH). These lines trace the molecular jet with temperature of $\sim$ 100 K and typical velocities are from few to tens km s^{-1}. However, in few cases, a series of aligned SiO structures with velocities up to 100 km s^{-1} are observed.

1.5.2 Physical parameters of outflows

The best tracer to study large–scale molecular outflows is carbon monoxide. It is an abundant molecule with a simple level structure (linear rotator). Moreover, thanks to its low dipole moment, CO is easily excited and often thermalized. As the CO emission traces ambient gas swept up by the outflow over its

lifetime, CO observations provide a time integrated picture of the outflow activity. It is therefore a challenge to read the outflow history from the observed CO lines, and from there to infer the history of mass loss from the central YSO.

The observation of the two transitions between the lowest levels of ^{12}CO and one of ^{13}CO allows the estimate of the excitation temperature and the opacity of the gas from which it is easy to calculate the column density. Considering the two ^{12}CO transitions J = 1 0 and J = 2 1 the ratio R_1 between the observed radiation temperature is

$$R_1 = \frac{f_{12}[I_{\nu_{12}}(T_{12}) - I_{\nu_{12}}(T_{BG})](1 - e^{\tau_{12}})}{f_{01}[I_{\nu_{01}}(T_{01}) - I_{\nu_{01}}(T_{BG})](1 - e^{\tau_{01}})} \tag{1.6}$$

where f_{ij} is the beam filling factor of the J = j i transition, T_{ij} is the excitation temperature, T_{BG} is the temperature of the microwave background, ν_{ij} is the frequency of the transition, τ_{ij} is the optical depth and

$$I_\nu(T) = \frac{h\nu/T}{e^{h\nu/kT} - 1} \tag{1.7}$$

R_1 is a function of the excitation temperature and the line opacity, with a different behaviour in the two extreme cases of an optically thin or thick line. Assuming that $f_{12} = f_{01}$ and that the microwave background is negligible, in the optically thin case Eq. 1.6 becomes:

$$R_1 = 4e^{h\nu_{12}/kT_{12}} \qquad (\tau_{01}, \tau_{12} \ll 1) \tag{1.8}$$

In the optically thick case Eq. 1.6 becomes:

$$R_1 = 2\frac{e^{h\nu_{01}/kT_{01}} - 1}{e^{h\nu_{12}/kT_{12}} - 1} \qquad (\tau_{01}, \tau_{12} \gg 1) \tag{1.9}$$

Fig. 1.3 shows the two expressions as a function of T_{12}, assuming $T_{12} = T_{01}$ in the optically thick case. For optically thick emission, R_1 approaches asymptotically a value of unity for high temperature. For optically thin emission, R_1 approaches 4 for high temperatures and it is less than 1 for low temperatures ($T < 8$ K). Thus, a value of R_1 higher than one is the signature of optically thin emission.

In the case of optically thick lines it is necessary to calculate the optical depth. The optical depth can be derived by using the transition J = 1 0

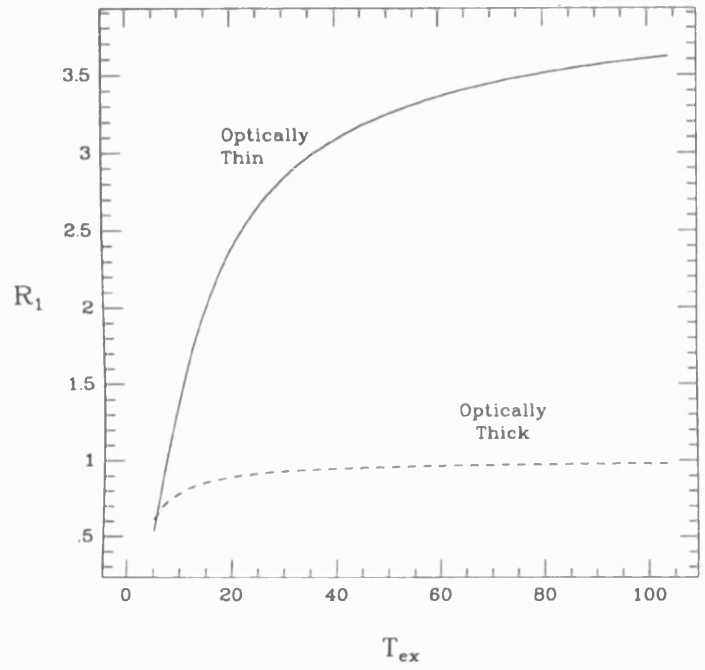

Figure 1.3: Plot of R_1 versus excitation temperature for the optically thin (continuum line) and the optically thick (dashed line) cases (figure from Levreault (1988)).

of ^{13}CO. R_2 can be defined as the ratio between the radiation temperature of the two transitions ^{12}CO (1–0) and ^{13}CO (1–0), analogous to R_1. Since we are dealing with the same transition in two closely similar molecules, the assumption of equal excitation is good. Assuming that the two beam filling factors are equal and that the ratio of the optical depth is simply the ratio of the abundances of the two molecules, R_2 assumes a simple expression in the two extreme cases. If both transitions are optically thin, then

$$R_2 = \frac{X(^{12}CO)}{X(^{13}CO)} = 90 \tag{1.10}$$

If the ^{12}CO (1–0) is optically thick (the ^{13}CO (1–0) is assumed always to be thin), then

$$R_2 = \frac{X(^{12}CO)/X(^{13}CO)}{\tau_{01}} = \frac{90}{\tau_{01}} \tag{1.11}$$

Any value of R_2 that is significantly less than the abundance ratio of ^{12}CO and ^{13}CO is indicative of optically thick ^{12}CO (1–0) emission. In reality the extreme cases are rare and Fig. 1.4 shows a more general diagnostic diagram

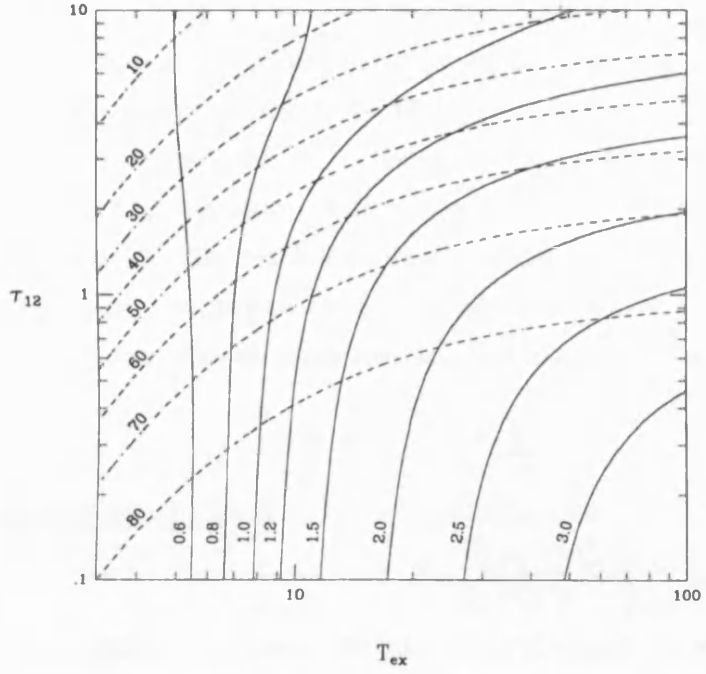

Figure 1.4: Contours plot of R_1 and R_2 as function of τ_{12} and T_{ex}. Solid contours are for R_1 and dashed contours are for R_2 (figure from Levreault (1988)).

for the two ratios. What are plotted are contours of R_1 and R_2 in the (τ_{12}, T_{ex}) plane under the assumption of equal beam filling factors and thermalization of the J = 0, 1, 2 levels of both ^{12}CO and ^{13}CO.

Once the excitation temperature and the opacity of the gas have been derived, it is easy to calculate the column density and other physical parameters for outflows. For the ^{12}CO (1–0) transition the CO column density is

$$N(CO) = 2.39 \times 10^{14} \int \frac{(T + 0.93)}{(1 - e^{-5.59/T})} \tau dv \ \text{cm}^{-2} \tag{1.12}$$

where the integration over the velocity (in km s^{-1}) is done in the velocity range of the non–Gaussian line wings. If one knows the CO abundance with respect to H_2, that for our galaxy is usually of the order of 2.8×10^{-4} (Cardelli et al., 1996), the total mass of the outflow can be derived:

$$M = \frac{N(CO)}{X(CO) 2 m_H A} \tag{1.13}$$

where m_H is the proton mass and A is the area of the outflow. Although the CO/H_2 ratio can be considered constant on large scale, it shows variations

on smaller scales (Sonnentrucker et al. 2002, Shinn et al. 2004), hence the assumption of the standard CO/H_2 ratio can introduce an error in the estimate of the mass and of all the other physical parameters correlated to it.

The CO transitions fall in the millimetre regime thus they can be easily spectroscopically resolved with the present telescopes. Knowing the velocity of the gas, the energetics of outflows can be derived summing the contribution over all the velocity channels (i). The momentum is

$$P = \sum_i M_i v_i \tag{1.14}$$

the kinetic energy is

$$E_{kin} = \sum_i \frac{1}{2} M_i v_i^2 \tag{1.15}$$

If one defines the mean velocity using the mass as weight

$$< v >= \frac{\sum_i M_i v_i}{\sum_i M_i} \tag{1.16}$$

the dynamical age of the outflow can be derived as the ratio between the size of the lobe and the mean velocity

$$t_{dyn} = \frac{R}{< v >} \tag{1.17}$$

Finally, it is possible to calculate the kinetic luminosity

$$L_{kin} = \frac{E_{kin}}{t_{dyn}} \tag{1.18}$$

and the momentum flux

$$F = \frac{P}{t_{dyn}} \tag{1.19}$$

Even if in principle it is possible to derive all the above parameters, they suffer considerable uncertainties. First of all, it is not easy to distinguish in the line profile the contribution of the outflow from that of the ambient component, which effectively means that one needs to define the right velocity range for the integration. Also the dynamical age is only a rough estimate of the age of the outflow. When clumps are present in the outflow, an alternative method to derive the age is to consider the ratio between the distance of the clumps and their velocity, assuming that the clumps are generated by episodic mass

loss of the central object, and that they travelled along the outflow till their present location. The biggest source of error comes from the difficulty to correctly derive the inclination angle of the outflow; this information is needed to correct the observed velocity along the line of sight and derive the true velocity. The inclination angle is usually estimated by eye from the CO map and thus it is highly uncertain. Another approach is to model the shape and the velocity field of the outflow lobes to obtain synthetic maps for comparison with the observations (Cabrit & Bertout, 1986). The magnitude of the error depends on the inclination of the outflow. If the outflow is mainly along the line of sight the correction for the velocity is small, since the velocity is inversely proportional to the sine of the inclination angle, while if the outflow is perpendicular to the line of sight the correction is larger.

1.5.3 An empirical outflow evolutionary sequence

In more then 20 years of investigations on outflows different characteristics have been discovered and attempts were made to classify the outflows on the basis of their observational properties. The first attempt used morphology (e.g. Bachiller & Tafalla 1988) and it was based on the collimation factor defined as the ratio between the major and the minor axes of the flow. Two classes were defined: the "classical" outflows that have a low collimation factor and the "high collimated" outflows with a high collimation factor. A more recent approach tries to explain the observational differences in the frame of an evolutionary sequence.

Outflows from Class 0 YSOs appear highly collimated (the prototypes are HH211 (Gueth & Guilloteau, 1999) and L1448 (Bachiller et al., 1990)), while outflows from Class I objects tend to be much less collimated. This suggests that molecular outflows lose part of their collimation as they evolve, starting as highly collimated bipolar systems and changing to classical outflows, losing an appreciable part of collimation. Outflow decollimation seems accompanied by the opening of a cavity in the parent cloud. In Class 0 outflows the cavity is narrow and has straight walls (e.g. L1157, Gueth et al. 1996) while in Class I outflows (e.g. L1151, Moriarty–Schieven & Snell 1988) the cavity is broader ($\sim$ 90 deg) and has almost parabolic walls. This is consistent with

the view of the outflow eroding the parent cloud and opening a broader and broader channel as time passes. Another possibility is that the jet component dominates the early times while in a latter stage a wider angle wind component appears, perhaps because a central channel along the outflow has been opened. However, very recent results, based on high spatial resolution interferometric observations, show that both a high velocity jet and a broad low velocity cavity can be simultaneously present also in very young outflows (Santiago-Garcia et al., 2006a).

Differences have been seen in the kinematic of the outflows. Class 0 outflows have an extremely high velocity (up to $\sim$ 100 km s^{-1}) gas along the axis, often in form of small condensation called molecular "bullets". This high velocity component is absent in more evolved outflows. The distribution of outflow wing intensity with velocity for a sample of 6 outflows (see Fig. 1.5) shows that all outflows have similar slopes at low velocities, with an average slope value of about -1.5. At higher velocities the slope of the distribution changes, becoming steeper and reaching values of the order of -4. The break point shifts to lower velocity as the age of the outflow increases (from $\sim$ 30 km s^{-1} in L1448 to $\sim$ 6 km s^{-1} in Mon R2). This means that as the outflow evolves, the amount of high velocity gas decreases. Also the energy of outflows decreases with time as testified by the correlation between the momentum flux and the amount of circumstellar mass, as traced by the millimetre flux (Saraceno et al., 1996). As the circumstellar matter is likely an indicator of age (mass decreases as age increases) the correlation suggests again that the outflow power decreases with time.

The change in the properties of outflows is not only observed at millimetre wavelengths but also in the FIR range. The observations carried out with the Long Wavelength Spectrometer (45 – 197 μm) on board ISO showed that the FIR luminosity due to the molecular emission (CO, H_2O, OH) is on average greater in Class 0 than in Class I sources, while the luminosity due to atomic lines ([OI]) is fairly constant in the two classes (Nisini et al., 2002). This result is interpreted in terms of an evolution in the modality of the interaction between the protostellar outflow and the circumstellar environment, with an increasing influence of the progressively less shielded interstellar FUV field.

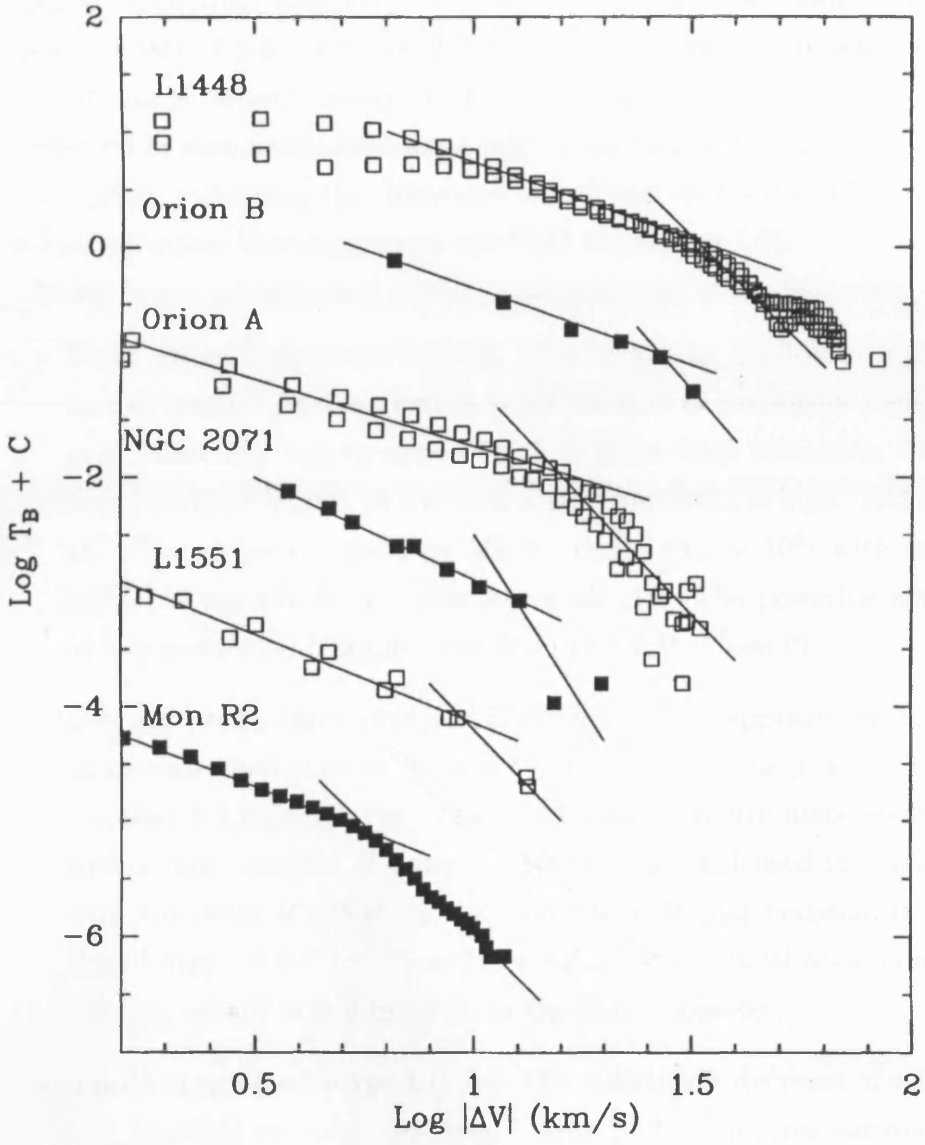

Figure 1.5: Log-Log brightness distribution with velocity for a series of outflows of different ages. Data from different authors compiled by Tafalla (1993).

During the Class 0 phase the impact of energetic flows with the environment gives rise to strong non-dissociative shocks (C-type shock, see Sect. 1.5.6) copiously emitting in molecular transitions, while during the Class I phase such impact produce less energetic shocks able to dissociate molecules (J-type shock, see Sect. 1.5.6). The trend of decreasing molecular emission is present also in Class II objects, indeed in Herbig Ae/Be stars the molecular emission is observed in rare cases and always only in the form of CO and OH (Giannini et al., 1999), indicating the dominant role of the unshielded FUV field from the central object that dissociates the H_2O to produce OH.

In summary, an empirical evolutionary sequence is the following:

- **First stage** (prototype L1448). The molecular outflow is highly collimated, almost jet-like, with a large fraction of extremely high velocity gas. Molecular bullets appear with extreme high velocities. The luminosity in the FIR due to the molecular component is high. SiO and H_2O abundances are increased by a large factor (up to 10^4) with respect to quiescent gas which indicates strong shocks. The powering source is a deeply embedded YSO not visible in the NIR (Class 0).

- **Second stage** (prototype L1157). The outflow appears less collimated and its terminal velocity is lower than in the previous phase. There is no evidence for high velocity bullets but the millimetre maps show regions with a large amount of warm ($\sim$ 100 K) gas condensed in small clumps with velocities of a few km s^{-1} and the molecular emission in the FIR is still high. A few molecules have enhanced chemical abundances. The exciting source is still invisible in the NIR (Class 0).

- **Third stage** (prototype L1551). The systematic decrease of collimation and terminal velocity continues. Clear shell structures surrounding an evacuated cavity with a reflection nebula appear. Optical Herbig-Haro objects are visible and no chemical anomalies are present. The molecular emission in the FIR is almost absent. Optical jets appear, with sizes up to a few pc. The exciting source is a Class I object.

In more evolved objects, such as Class II, the molecular outflow and the radio jet are rarely present while optical jets are observed (Hirth et al., 1997).

In fact, at this stage the circumstellar envelope has been dispersed and the initial part of the outflow becomes visible in the optical. Recent results on T Tauri objects show atomic micro jets in the form of a sequence of knots with spacing of the order of 500 AU (e.g. Dougados et al. 2000, Lavalley–Fouquet et al. 2000). More distant, faint knots are sometimes detected out to 0.1 pc, but no parsec–scale jets have been identified at this evolutionary stage. Observations with the Space Telescope Imaging Spectrograph on board the Hubble Space Telescope (HST) show that the initial part of the jet, at 0.2 – 0.3 arcsec from the source, is rotating in the region where the jet has been collimated but has not yet interacted with the environment (Coffey et al., 2004). The zone at the base of the outflow, where the jet is launched, has a size of the order of a few hundreds of AU, that requires sub–arcsecond spatial resolution in order to be resolved. Up to now this has been possible only in the optical with adaptive optics, integral field spectroscopy and HST. The extension of such kind of study to younger objects requires a next generation very high resolution imaging spectrometer at IR wavelengths, where the extinction is reduced, in order to be able to trace the most inner and embedded part of the young protostars.

Although an empirical time sequence has been defined, understanding how outflows evolve, and how their observed properties depend on the age of the associated protostar is still one of the open point of the modern astronomy. In fact, very recent results query the evolutionary sequence proposed in the 90s, proposing a new vision based on the chemical properties of outflows (Santiago-Garcia et al., 2006b).

1.5.4 Models of outflow acceleration

It is now clear that stellar jets, with speeds of 100 – 300 km s^{-1} and density of the order of 10^3 cm^{-3}, are responsible for accelerating much of the molecular gas in many of the youngest low–mass outflow systems. However, there is also good evidence for momentum being deposited into the flows by wind components with wider opening angles and this component becomes relatively more powerful as the flow ages. Indeed, jet–driven models (Masson & Chernin 1993; Raga & Cabrit 1993) are able to reproduce the shape of highly collimated

outflows and the mass distribution, while wind–driven models (Shu et al., 1991) are able to reproduce the shape of the classical outflows.

The momentum of the outflows, as estimated by CO observations, is typically a factor of 100 higher than the radiation pressure given by the bolometric luminosity of the central star (e.g. Lada 1985), which rules out radiative pressure as the acceleration mechanism of the outflows. On the contrary, the correlation between the momentum flux and the amount of circumstellar mass, as traced by the millimetre flux (Saraceno et al., 1996), suggests that the circumstellar envelope and/or the disk play a direct role in accelerating the outflows.

Different models have been developed proposing quite a number of efficient accretion–powered wind mechanisms from the stellar surface, disk or disk–magnetosphere boundary. The most efficient models use a strong magnetic field in the star or disk to drive the wind and to carry off angular momentum from the accreting gas. This wind is further collimated by magnetic or hydrodynamic processes (e.g. Mellema & Adam 1997), generating a high Mach number wind or jet with a speed of the order of 200 – 800 km s^{-1}. Centrifugally driven winds from disks threaded by open magnetic field lines provide the most efficient way of tapping the gravitational potential energy liberated in the accretion process to power the outflow. The fact that such winds automatically carry away angular momentum and thus facilitate (and possibly even control) the accretion process make them an attractive explanation for the ubiquity of the jets in YSOs. Such outflows are indeed easy to produce and maintain under a variety of surface boundary conditions. Numerical simulations have also verified the ability of such outflows to self–collimate and give rise to narrow jets, as well as a variety of other characteristics that are consistent with YSO observations. In these models only a small fraction of the accretion flow is ejected in the wind. A different scenario (Fiege & Henriksen, 1996) is that molecular flows are not predominantly swept up by an underlying wind but represent infalling gas that has been deflected into polar streams by magnetic forces. Only a small fraction of the infalling gas actually reaches the star to produce accretion luminosity and the outflow mass rate is higher than the infall mass rate. This scenario has been invoked in particular to explain

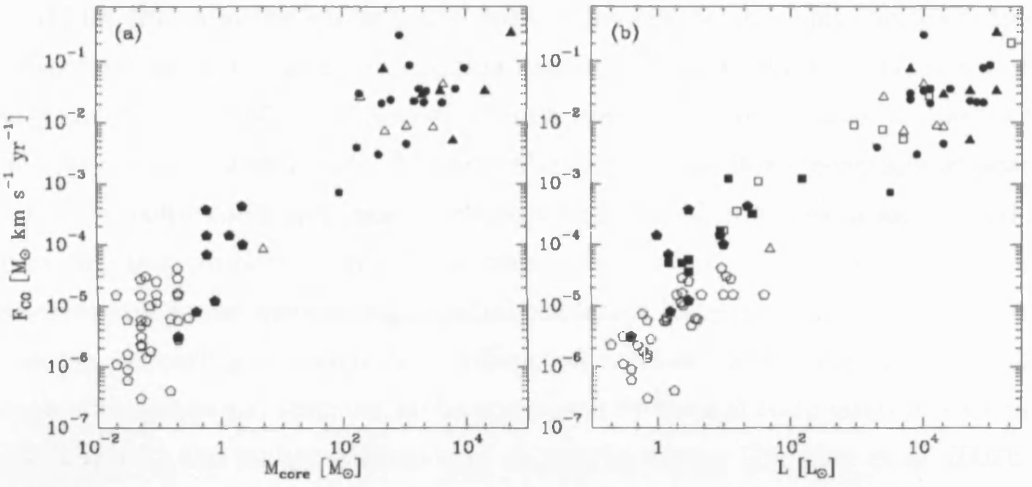

Figure 1.6: Outflow parameters correlations (figure from Beuther et al. 2002a): a) mechanical force versus core mass from 1.2 mm dust emission. b) Mechanical force versus bolometric luminosity. The dots are the objects from the sample of Beuther et al. (2002a), the open triangles are the sources at the near kinematic distance and the filled triangles are the sources at the far kinematic distance. The pentagons show data from Bontemps et al. (1996) and the squares are from Cabrit & Bertout (1992). Open squares and pentagons represent Class I sources and filled symbols Class 0 sources.

the large flow masses observed in flows from luminous sources.

1.5.5 Outflows from high mass stars

The scenario depicted above is valid for outflows generated by low mass protostars. The scenario of outflows powered by high–mass protostars, however, is less clear because of the intrinsic difficulties in observing these fast evolving and distant objects with a suitable resolution. Systematic studies at low angular resolution of the CO lines indicate that $\sim$ 80–90% of the observed massive star forming regions are associated with outflows (Zhang et al. 2001; Beuther et al. 2002a) and that massive outflows show physical characteristics similar to those of low–mass outflows. The correlation between the mechanical force and the mass of the millimetre core and with the bolometric luminosity is shown in Fig. 1.6 for both low and high mass outflows (Beuther et al., 2002a).

While this may be statistically correct for the relationship between the global flow energetics and the exciting source bolometric luminosity, it is not yet clear if the detailed properties of high mass flows are similar to those of the lower–mass counterparts. In particular, high–mass flows generally appear to be less collimated and more turbulent than flows from low–mass objects. However, this property could be a consequence of the fact that single dish observations do not have enough spatial resolution to resolve the flows. Indeed, systems appearing as single low collimated outflow, when observed with a single dish telescope, turn out to be composed by several collimated jets when observed with the higher resolution of an interferometer (Beuther et al. 2002b; 2003). Additionally, the fast moving, high excitation and highly collimated jet component usually observed in low–mass systems is much weaker or absent in high–mass flows (Shepherd et al. 1997; Shepherd 2003). Important differences in the physical structure of the flows have also been observed at millimetre wavelengths (Molinari et al., 2002). All these results suggest that simple scaling of low–mass flow models may not be applicable (Richer et al. 2000; Shepherd 2003).

Understanding the characteristics of outflows associated with high mass protostars is important also for understanding the formation of high–mass stars. In fact, the similarity of low– and high–mass outflows and the continuity of their physical parameters suggest that a similar mechanism is at work in the formation of low and high–mass stars, supporting the accretion models for high–mass star formation. On the other hand, the existence of multiple outflows seems to support the coalescence scenario. A more extended statistical study at very high resolution of high–mass outflows is needed to answer this question.

1.5.6 The chemistry of outflows

The propagation of supersonic flows within molecular clouds produces strong shock waves that compress and heat the gas, triggering chemical reactions that do not operate in quiescent environments. In addition, shock processing of the dust grains results in the injection of atoms and molecules in the gas phase. Thus the gas in the outflows shows a peculiar chemical composition. Table 1.1

Table 1.1: Comparison between chemical abundances in cold clouds and shocked outflows.

Molecule	Cold Cloud abundance	Outflow abundance	Ref.
H_2O	10^{-7}–10^{-8}	10^{-5}–10^{-4}	1,2
SiO	$<10^{-12}$	10^{-10}–10^{-6}	3,4
SO	$\sim 10^{-9}$	$\sim 10^{-7}$	5
CH_3OH	$\sim 10^{-9}$	$\sim 10^{-7}$	5
NH_3	$\sim 10^{-8}$	$\sim 10^{-6}$	6
HCN	$\sim 10^{-8}$	$\sim 10^{-7}$	5

References: 1 Snell et al. (2000), 2 Giannini et al. (2001), 3 Codella et al. (1999a), 4 Martin–Pintado et al. (1992), 5 Bachiller & Pérez–Gutiérrez (1997), 6 Tafalla & Bachiller (1995).

lists the typical abundance of several molecules in cold clouds and in shocked outflow regions.

Detection of molecular lines provides a useful tool not only to study the chemistry of outflows but also for estimating the physical conditions of the shocked component. Moreover, the cooling times of the shocked region are short, making the chemistry strongly time dependent so that the relative abundance of molecules can be used as chemical clocks to infer the age of the outflows. In particular, the sulphur–bearing species have been extensively used as chemical clocks in shocked sites such as outflows and hot cores (e.g. Charnley 1997; Wakelam et al. 2004; Codella et al. 2005).

During the interaction between the supersonic jet and the surrounding molecular cloud two types of shocks can occur: J–type (e.g. Hollenbach & McKee 1979) and C–type shocks (e.g. Draine et al. 1983). In J–type shocks there is a discontinuity in the physical parameters of the gas immediately behind the shock front: density, temperature and velocity jump to drastically higher values in the post shock gas. In C–type shocks, occurring at low velocity and moderate to low ionization, the physical parameters increase continuously

across the shock front. In J–type shocks the temperature reaches values as high as 10^5 K in the shock front so that the molecules are dissociated. However, when the gas cools the molecules reform and refractory elements (e.g. Si and Fe) are injected in the gas phase by thermal sputtering from the dust grains. The first molecule that reforms is H_2, which interacts with oxygen to produce the most important coolants: OH, H_2O, and CO. OH and H_2O are formed by the sequence:

$$O + H_2 \rightarrow OH + H$$
$$OH + H_2 \rightarrow H_2O + H$$

Carbon monoxide is formed predominantly by reaction of C^+ with OH

$$C^+ + OH \rightarrow CO + H^+$$

The very chemically active OH radical is crucial also for the chemistry of sulphur, nitrogen and silicon. When OH reacts with sulphur, SO is formed

$$S + OH \rightarrow SO + H$$

Sulphur oxide is slowly converted to sulphur dioxide in a reaction with OH

$$SO + OH \rightarrow SO_2 + H$$

When OH reacts with nitrogen, NO is formed

$$N + OH \rightarrow NO + H$$

Nitric oxide can reacts with atomic carbon to produce cyanogen

$$NO + C \rightarrow CN + O$$

which may reacts with molecular hydrogen to form HCN

$$CN + H_2 \rightarrow HCN + H$$

Finally, the reaction of OH with silicon produces SiO

$$Si + OH \rightarrow SiO + H$$

These reactions are endothermic and can be activated also in C–shocks in the thick gas layer where the temperature is increased to moderate values ($\sim$ 2000 K) and the molecules are preserved. Additionally, in C–shocks non–thermal sputtering due to dust–molecule or dust–dust collisions results in the injection of refractory and volatile species, mainly from grain mantles, into the gas phase.

In both J– and C–type shocks, moving away from the shock front, the gas cools down; hence reactions with high energy barriers will not operate and the chemistry is dominated again by the usual low–temperature reactions. Depletion of molecules onto the dust grains starts again to be important, reducing the abundance of some of the newly formed molecules. Nevertheless, the chemical composition of both the gas and the solid phase remains altered, maintaining a record of the passage of the shock wave. Chemistry is thus a powerful tool to trace the history of the shocked material and infer the age of outflows.

The chemical effects of shocks are better studied in outflows from Class 0 sources because these are particularly energetic and highly collimated. Large spectral surveys at millimetre wavelengths have been carried out in some outflows: NGC1333–IRAS4 (Blake et al., 1995), NGC1333–IRAS2 (Langer et al. 1996; Bachiller et al. 1998), L1157 (Bachiller et al., 2001), CB3 (Codella & Bachiller, 1999b), BHR71 (Bourke et al., 1997), CB34 (Codella et al., 2002). These outflows have a millimetre spectrum particularly rich in molecular emission and the fractional abundance of molecules such as SO, SO_2, SiO, CH_3OH, etc. are significantly enhanced (up to a factor of 10^4) with respect to the quiescent gas (see Table 1.1).

1.5.7 Molecular clumps along outflows

Small molecular clumps are often detected in association with outflows from low– and intermediate–mass protostars. In fact, two main kinds of clumps have been observed. The first type is the high–velocity clumps, the so–called molecular bullets, that are well defined entities travelling at velocities larger than 100 km s^{-1}. These bullets are observed in SiO in the lobes of the L1148 outflow (Bachiller et al., 1991), where they appear in pairs with the members

of a pair being symmetric in both position and velocity with respect to the star. These bullets are most likely associated with bow shocks formed by the outflow propagation (e.g. Dutrey et al. 1997). The molecular lines emitted by this kind of clumps are relatively weak, so their chemical composition remains unknown. The second type is the low velocity clumps, with dimensions not exceeding 0.1 pc and velocity of few km s^{-1} with respect to the v_{LSR}. These molecular clumps are characterized by a rich molecular emission from species (e.g. SO, SO_2, CH_3OH) usually unobserved along outflows. An example of such clumps can be found along the L1157 and CB3 outflows (Codella & Bachiller 1999b; Bachiller et al. 2001).

The origin of the low velocity clumps is not yet clear. Usually, these clumps are detected in pairs in the two lobes of the outflows in a quasi–symmetric position with respect to the central object. Hence, it is traditionally believed that these low velocity clumps are generated by episodic mass loss of the forming object. On the other hand, it may also be that, if the ISM is clumpy down to scales of $\sim$ 0.01 – 0.1 pc (e.g. Morata et al. 2003; Falle & Hartquist 2002), the clumps themselves are pre–existing and that the effect of the outflow is only to accelerate and shock them. Alternatively, it is possible, similarly to what is also suggested by Arce & Goodman (2001), that the clumps originate much closer to the source, in the envelope of the star, and then are swept away by the outflows. Arce & Goodman (2001) produced a model for the outflow driven by the young star IRAS 04239+2436 which appears very clumpy when observed in CO and ^{13}CO. The clumps resulted to be the product of the outflow sweeping up ambient gas rather than being pre–existing cloud clumps. However, their assumption is that the ambient gas is homogeneous, at a density of $\sim 5{\times}10^3$ cm^{-3}, and that the outflow will sweep–up a volume of $\sim$ 0.5 $M_\odot$, maintaining the same density of pre–existing cloud material so, effectively, from a chemical point of view, the clump is indeed pre–existing the outflow/star system as the final density was reached without the intervention of the outflow. In this picture the morphology of the swept–up ambient gas and not its high density is a manifestation of the episodic nature of the outflow.

An investigation of the origin and the structure of these low velocity, chemically rich clumps observed along outflows has been carried out in this thesis.

Chapter 2

The chemical and radiative transfer models

2.1 Chemical modelling

In the last decade chemistry has become a powerful investigative tool in the study of star formation. Indeed the formation of dense molecular condensations and eventually stars, involves large changes in the physical properties of the atomic and molecular gas. These changes significantly affect the chemical composition of the gas and dust inside the forming cores/stars. In particular, as the density increases atoms and molecules in the gas phase collide with the dust grains with greater frequency and if they stick with any reasonable efficiency, they will deplete from the gas phase. Thus the density gradient that results from the core condensation is accompanied by chemical gradients, with the inner parts of the core representing high density chemistry and the outer parts representing the original low density composition. High spectral resolution observations of molecular emission are extremely useful also for obtaining information on the kinematic inside molecular clouds. Finally, because chemistry controls critical physical processes in star formation such as the fractional ionization and cooling of the gas, a detailed understanding of the chemical composition of the gas and dust surrounding young stars is important and interesting in its own right.

The development of sensitive continuum and heterodyne arrays probing

the millimetre and sub–millimetre spectral ranges has led to an explosion of observations of molecular species and a scenario has emerged for the main chemical processes that occur during star formation (van Dishoeck & Blake 1998a and reference therein). In cold molecular cloud cores the chemistry is dominated by low–temperature, gas–phase, ion–molecule and neutral–neutral reactions leading to the formation of small radicals and unsaturated molecules (Rawlings et al. 1992; Ohashi et al. 1992; Suzuki et al. 1992; Howe et al. 1996; Pratap et al. 1997). During the cold collapse phase, the density becomes so high that most molecules accrete onto the grains and form an ice mantle (Teixeira et al. 1998; Chiar et al. 1998). Here the chemistry can be actively modified by surface reactions and through processing by ultraviolet photon, X rays, and cosmic rays. After the new star has formed, its radiation heats up the surrounding gas and dust and the icy mantles begin to evaporate into the gas phase (Ceccarelli et al., 1996). In addition, the outflows from the young star penetrate the surrounding envelope, creating high temperature shocks and lower temperature turbulent regions in which the icy mantles and more refractory material containing silicon can be returned to the gas. These freshly evaporated molecules can then drive a rich and complex chemistry in the gas (see Sect. 1.5.6). Finally, the envelope is dispersed by winds and, in the case of massive stars, ultraviolet photons, leading to the appearance of photon–dominated regions (PDR). Each of the different phases is best probed by prototypical molecular species and in Fig. 2.1 the characteristic molecules in each phase are reported.

Many models have been developed since 1940s to describe the chemistry in interstellar clouds (e.g. Millar & Nejad 1985; Bergin et al. 1995; Charnley et al. 2001; see van Dishoeck & Blake 1998a for a review). In the past, two different classes of chemical models can be found. *i)* The steady–state, depth dependent models, in which the abundances of the molecules do not change with time but are functions of the depth into the region: e.g. models for dense ultraviolet photon– or X ray–dominated regions near young stars (Hollenbach & Tilens, 1997). *ii)* The time–dependent, depth independent models, in which the abundances are computed as a function of time at a single position inside the cloud: e.g. models of dark pre–star forming clouds (Millar et al., 1991),

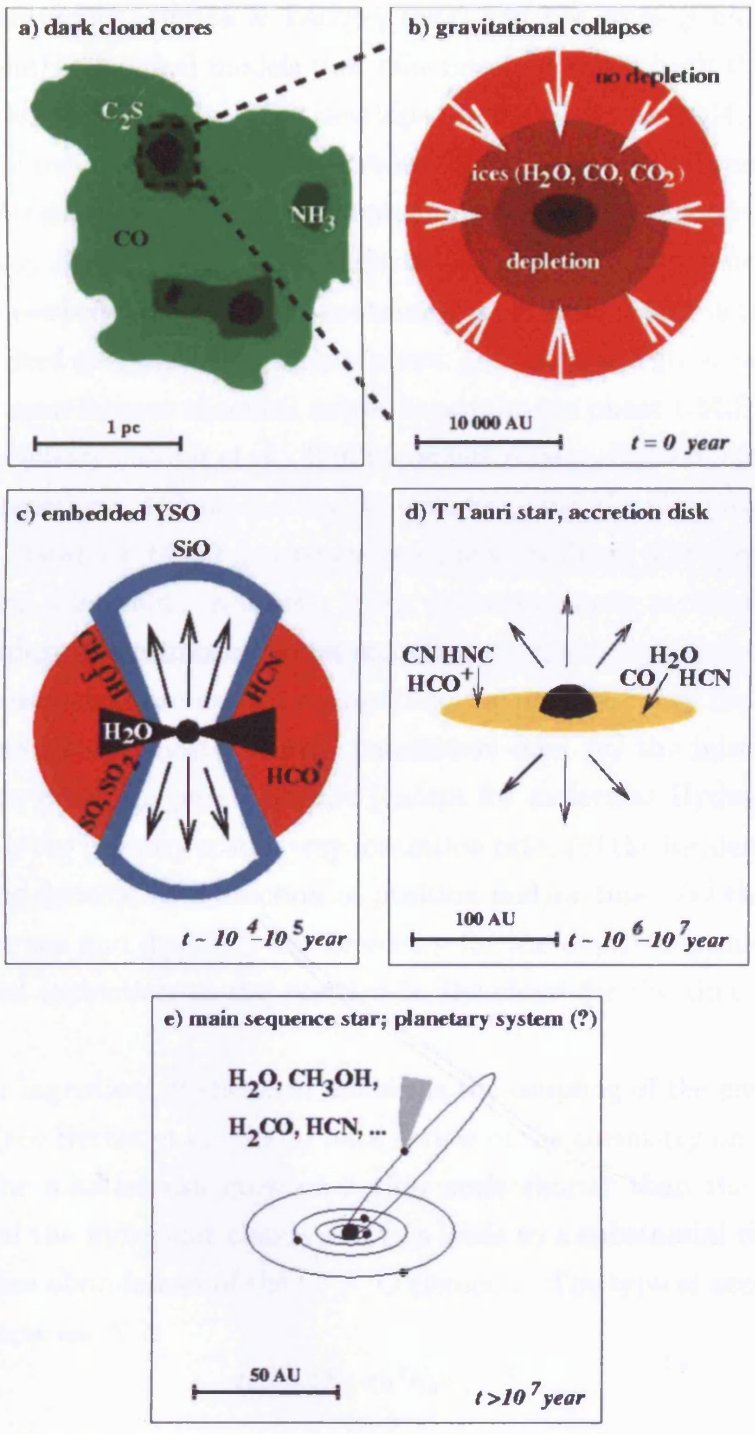

Figure 2.1: A schematic view of the low–mass star formation. Characteristic molecular species at each stage are shown (figure from van Dishoeck & Blake (1998a).

collapsing envelopes (Bergin & Langer, 1997) and hot cores (Charnley et al., 1992). Recently, chemical models that take into to account both the geometry and the time evolution have been developed (e.g. Viti et al. 2004).

Chemical models are based on databases listing the chemical reactions with their parameters. Starting from the first, simple pure ion–molecule, gas–phase networks (e.g. Bates & Spitzer 1951; Herbst & Klemperer 1973), nowadays sophisticated networks are available, containing more then 4000 reactions among several hundred species, including gas–phase, gas–grain and grain–surface reactions. The most famous chemical networks are the gas phase UMIST database for Astrochemistry (Millar et al., 1997) (the last release, Rate05, contains 4566 gas–phase reactions, 413 species and 12 elements) and the Ohio State University (OSU) database (4300 gas–phase reactions involving 430 species and 12 elements plus gas–grain reactions). Many authors compile personal databases collecting information from different sources.

Many parameters are needed as inputs to the models. They depend on the models, however the most common parameters are: *(a)* the initial chemical composition, usually a purely atomic (except for molecular Hydrogen) gas is assumed; *(b)* the primary cosmic–ray ionization rate; *(c)* the incident radiation field; *(d)* the density, as a function of position and/or time; *(e)* the temperatures of the gas and dust; *(f)* the geometry for the depth–dependent models or the visual extinction at the position in the cloud for the time–dependent models.

Another ingredient of chemical models is the coupling of the gas and grain chemistry (see Herbst et al. (2005) for a review of the chemistry on interstellar grains). The mantles can grow on a time scale shorter than the dynamical time scale of the molecular clouds and this leads to a substantial reduction of the gas–phase abundances of the C, N, O elements. The typical accretion time scale for a species X is

$$t_{ac} = (S_X \pi a^2 n_d v_X)^{-1} \tag{2.1}$$

where S_X is the sticking coefficient and it is close to unit for most species at very low temperature, v_X is the relative velocity of the species X with respect to the grains and $\pi a^2 n_d$ is the grain cross section per unit volume for a spherical grain of number density n_d. Assuming the classical grain dimension, $a = 1000$ Å and

density, $n_d = 1.3 \times 10^{-12} n_{H_2}$ cm^{-3} (Spitzer, 1978), and a sticking coefficient of unity, $t_{ac} = 3 \times 10^9 n_{H_2}^{-1}$ yr. In dense clouds, with $n_{H_2} > 10^5$ cm^{-3}, the accretion time scale becomes much shorter ($< 10^4$ yr) than the collapse time scale. As expected from this simple consideration, observational results confirm that in a cloud that is collapsing to form a star many elements are depleted below their solar or cosmic abundances (Caselli et al. 1999; Kramer et al. 1999; Tafalla et al. 2004). However, in parallel to the freeze–out, some mechanisms are at work to desorb or remove molecules from the grains and return then to the gas phase. Thermal evaporation is effective at high temperatures ($T \gg 20$ K), once the star has formed. Various other mechanisms have been proposed including spot heating due cosmic ray or X rays impacts and chemical desorption. The efficiency of these mechanisms depends strongly on the binding energy of the molecules on the grain surface. The grain chemistry is still not well understood and the current uncertainties regarding the surface reactions are the main source of error in chemical models

A proper theoretical treatment of the chemistry in star–forming regions ideally would benefit from the coupling of chemical models with multidimensional hydrodynamical models for all phases of the star formation process, including the collapse phase, the disk formation, the development of the bipolar outflow and the dispersion of the envelope. Such complete chemical–hydrodynamical codes require an enormous amount of computational power, so many models make simplifications on either the chemical or the dynamical side.

2.1.1 The UCL chemical model

The chemical model used in this work has been developed by Dr. Serena Viti. Since its origin (Viti & Williams, 1999a) the model has been applied to a variety of astrophysical objects: e.g. clumps ahead of Herbig–Haro objects (Viti & Williams, 1999a), hot cores (Viti et al., 2001), low–mass star forming cores (Viti, Natarajan & Williams, 2002), planetary nebulae (Redman et al., 2003), high–redshift galaxies (Lintott, 2005). All these applications are a modification of the basic model described by Viti & Williams (1999a).

The chemical network is modified from the UMIST database RATE95 and includes 221 species involved in 3194 reactions (Millar et al., 1997). It in-

Table 2.1: Initial gas phase elemental abundances with respect to the total number of hydrogen nuclei.

atom	abundance
H_2	0.5
He	0.14
O	2.14×10^{-4}
C	1.0×10^{-4}
N	6.0×10^{-5}
S	1.3×10^{-7}
Mg	7×10^{-9}

cludes both the gas–phase and grain–surface chemistry. The surface reactions included are described by Viti & Williams (1999), and are briefly described as follows: it is assumed that all species that can be hydrogenated on dust grain surfaces will be fully saturated, e.g. oxygen atoms are converted to H_2O and carbon atoms to CH_4, and retained on the surface. In addition, a small fraction of CO, 0.01% (as suggested by models such as those of Charnley et al. (1992)), is assumed to be converted to methanol on the surfaces of grains. The version of the model used in this thesis is single–point; however we can deal with a more complex geometry by breaking down the analyzed region into different points.

The model is time dependent and it follows the chemical evolution of the object. Usually, the evolution is divided in two phases. Firstly, the object is formed by the gravitational collapse from a diffuse cloud. The initial chemical composition is assumed to be purely atomic, apart from half of the hydrogen assumed to be molecular. The elemental atomic abundances are listed in Table 2.1 (Sofia & Meyer, 2001). The collapse is treated as a 'modified free–fall', as defined by Rawlings et al. (1992). The derivate of the density of the collapsing object with respect to time is given by:

$$\frac{dn}{dt} = B\left(\frac{n^4}{n_0}\right)^{1/3}\left\{24\pi G m_H n_0\left[\left(\frac{n}{n_0}\right)^{1/3} - 1\right]\right\}^{1/2} \tag{2.2}$$

where G is the gravitational constant, m_H is the hydrogen mass and n_0 the

initial mass. The parameter B may be thought of as a retardation factor which is < 1 if gas or magnetic pressure resists the collapse so that the collapse is slower than free–fall and is equal to unity for free–fall collapse. During the collapse phase, gas–phase chemistry and freeze–out onto dust grains with subsequent processing are assumed to occur. The collapse is terminated as the final density (treated as a free parameter) is reached or at a time (dependent on the density) at which a certain fraction of the gas–phase species have frozen as ices on the dust grains. In the second phase the formed object interacts with the surrounding environment, for example the gas is subjected to a flux of cosmic rays or to an external radiation field, or it undergoes a shock phase with a sudden rise of the temperature.

The output of the chemical model consists of the chemical abundances of all the considered species both in the gas–phase and on the grain as a function of time.

2.2 Radiative transfer models

A number of sophisticated, non–local radiative transfer codes have been developed for the interpretation of molecular line emission (e.g. Bernes 1979; Juvela 1997; Hogerheijde & van der Tak 2000; Ossenkopf et al. 2001). The applications of these codes range from protostellar environments to the circumstellar envelopes of late type–stars.

The radiative transfer problem is represented by a differential equation describing the intensity I along a photon path $\mathrm{d}s$, at frequency ν

$$\frac{\mathrm{d}I}{\mathrm{d}s} = \kappa - \epsilon I \tag{2.3}$$

where κ is the emission coefficient and ϵ is the absorption coefficient. Another way of writing Eq. 2.3 is

$$\frac{\mathrm{d}I}{\mathrm{d}\tau} = S - I \tag{2.4}$$

where $\mathrm{d}\tau = \epsilon \mathrm{d}s$ is the optical depth at the frequency ν and $S = \kappa/\epsilon$ is the source function and represents the emissivity of the medium per unit optical depth. Eq. 2.4 can be written in the integral form, which is the form that is

most often used in radiative transfer codes

$$I(\tau) = \int_0^\tau S(\tau')e^{\tau'-\tau}\mathrm{d}\tau' \tag{2.5}$$

where τ is the optical depth between the point where I is evaluated and spatial infinity along the line of sight. This integral is evaluated along all possible straight lines through the medium. In practice, this is a discrete sample of lines covering all directions as well as possible.

The emission and absorption coefficients are determined by the transition rates between the various levels and the population of these levels. For a transition from level i to level j (where the energy of level i is greater then that of level j) the emission and absorption coefficients are:

$$\kappa_{ij} = n_i A_{ij} \tag{2.6}$$

$$\epsilon_{ij} = n_j B_{ji} - n_i B_{ij} \tag{2.7}$$

where n_i and n_j are the population density for the i and j level and A_{ij}, B_{ji} and B_{ij} are the Einstein coefficients.

The source function for a particular transition S_{ij} is independent on the velocity if one assumes complete frequency redistribution, i.e. the frequency deviation from line center of absorbed and emitted photons are uncorrelated. The source function then becomes

$$S_{ij} = \frac{\kappa_{ij}}{\epsilon_{ij}} = \frac{n_i A_{ij}}{n_j B_{ji} - n_i B_{ij}} \tag{2.8}$$

The relative level populations n_i are determined from the statistical equilibrium equation

$$\sum_{j>i}[n_j A_{ji}+(n_j B_{ji}-n_i B_{ij})J_{ji}]-\sum_{j<i}[n_i A_{ij}+(n_i B_{ij}-n_j B_{ji})J_{ij}]+\sum_j[n_j C_{ji}-n_i C_{ij}] = 0 \tag{2.9}$$

where C_{ij} is the collisional rate coefficient and J_{ij} is the integrated mean intensity over the line profile

$$J_{ij} = \frac{1}{4\pi}\int I_\nu(\Omega)\mathrm{d}\Omega\mathrm{d}\nu \tag{2.10}$$

where Ω represents the spatial direction in which the intensity $I_\nu(\Omega)$ is measured.

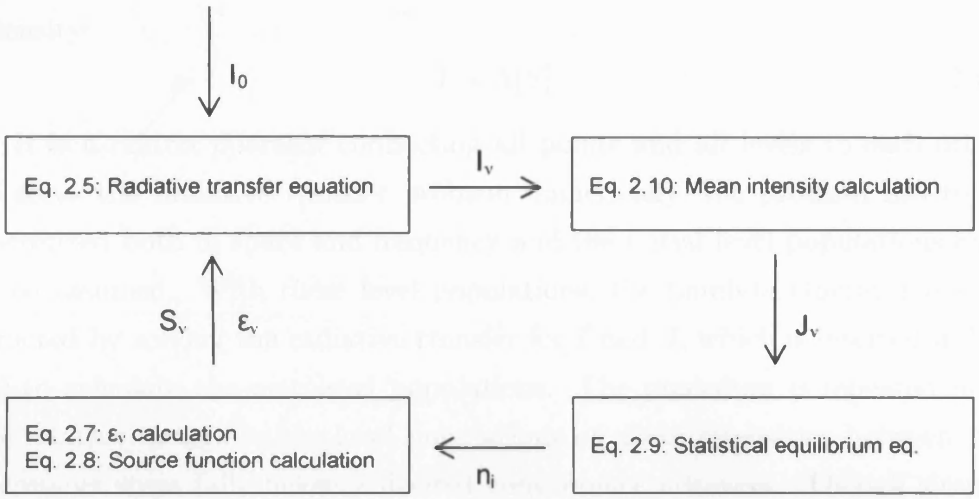

Figure 2.2: A Flow diagram of the molecular line radiative transfer problem (figure adapted from van Zadelhoff et al. (2002)). The arrows indicate the direction of the dependency of the equations. Several iterations are needed to calculate the true level populations.

Eqs. from 2.5 to 2.10 form a set of coupled equations. The way in which the quantities depend on each other is depicted in Fig. 2.2. The intensities are found by integrating the source function (Eq. 2.5). The source function and extinction coefficients depend on the level populations (Eqs. 2.6, 2.7). These in turn depend on the intensities (Eqs. 2.9, 2.10). To solve this set of equations one must determine the radiation field and the level populations simultaneously. Since the radiation field couples the level population at different spatial positions to each other through the transfer integral (Eq. 2.3), the only way of solving the system directly is through complete linearization and solving a huge matrix equation involving all level populations at all spatial positions. In practice, the evaluation of the matrix elements and the inversion of the problem consumes far too much CPU–time as well as memory and it is therefore beyond current computing capabilities. An alternative and much simpler way is to iteratively evaluate all equations, following the arrows as illustrated in Fig. 2.2. This method is called Lambda Iteration since the process of iteration can be mathematically written into a formalism involving the Lambda Operator. The Lambda Operator acts on the source function to generate the mean

intensity:

$$J = \Lambda[S] \tag{2.11}$$

It is a matrix operator connecting all points and all levels to each other. To solve the radiative transfer problem numerically, the problem has to be discretized both in space and frequency and the initial level populations have to be assumed. With these level populations, the Lambda Operator is constructed by solving the radiative transfer for I and J, which is inserted in Eq. 2.9 to calculate the new level populations. The procedure is repeated until the relative change in the level populations or mean intensities between two successive steps falls below a desired convergence criterion. Though simple, the principal disadvantage of the Lambda Iteration method is that it converges slowly at high optical depth and it appears to converge erroneously.

In order to speed up the convergence the Approximated/Accelerated Lambda Iteration (ALI) method has been developed (Scharmer & Carlsson 1985; Rybicki & Hummer 1991). This method is based on the definition of an approximated Lambda Operator, Λ^* so that

$$J = \Lambda^*[S] + (\Lambda - \Lambda^*)[S^n] \tag{2.12}$$

where S^n is the source function at the n^{th} iteration. A good choice for Λ^* is the diagonal part of the full Lambda Operator.

Another method consists in the linear perturbation of the radiation transport equation and the mean intensity equation (Eqs. 2.4 and 2.10), neglecting the second and higher order terms. The linearization greatly reduces the effect of high optical depth terms and allows rapid convergence. This method, called MULTI has been developed by Carlsson (1986) and modified by Harper (1994) to include spherical symmetry, S–MULTI.

The radiative transfer analysis requires accurate molecular data in the form of energy levels, statistical weights and transition frequencies as well as the spontaneous emission probabilities (Einstein coefficients) and the collisional rate coefficients. The JPL catalog (Pickett et al., 1998), the HITRAN database (Rothman et al., 2003) and the CDMS catalog (Müller et al., 2001) are the most famous databases where energy levels and transition strengths for a large number of molecular species are collected. The collisional rates

are more difficult to calculate and in the literature they are usually found for low temperatures and the lowest energy levels. The collisional rates for higher temperatures and higher levels are usually calculated extrapolating the low temperature data.

2.2.1 Spherical Multi–Mol

The radiative transfer code used in this work is Spherical Multi–Mol (SMMOL) and it has been developed by Dr. J. Yates. The code has been already used to model the molecular line emission of a variety of astronomical objects, e.g. infalling core (Rawlings & Yates, 2001) and the PDR and shocked gas in the Orion KL cluster (Lerate et al., in preparation). The model has been successfully benchmarked with similar models (van Zadelhoff et al., 2002).

SMMOL is based on the S–MULTI Approximate Λ–iteration (ALI) method and it solves multi–level non Local Thermodynamic Equilibrium (LTE) radiative transfer problem in both molecular lines and the dust continuum. It includes an empirical dust model (Mathis, 1990) and converges quickly for the optically thick line center. As a first step the code calculates the total radiation field and the level populations assuming LTE and the interstellar radiation field as input continuum (Black, 1994). It then re–calculates the total radiation field, checks for convergence and repeats the process until convergence is achieved. The adopted convergence criterion is $(n_i - n_{i-1})/n_i = 10^{-4}$. The space is discretized in 50 points and at each point the code generates the level populations and the line source functions. The emergent intensity distributions are then convolved with the telescope beam, so that the model directly predicts the line profiles for a given source as observed with a given telescope.

The input parameters of the models are: (*a*) molecular data including molecular mass, energy levels, transition frequencies, radiative rates and collisional rates; (*b*) dust data including size distribution, opacity law etc.; (*c*) physical data describing the object to model. This includes the radial dependency of the gas density, the fractional abundance of the molecule, the macro velocity, the microturbulent velocity and the gas (kinetic) and dust (thermal) temperatures. The molecular data needed for the calculation are taken from

the LAMBDA[1] public database (Schöier et al., 2005), except for the CH_3OH-A data which we obtained from Prof. D. Flower (private communication).

[1] http://www.strw.leidenuniv.nl/~moldata

Chapter 3

The chemical modelling of the low velocity molecular clumps along outflows

The work presented in this Chapter has been published in the paper by Viti et al. (2004). My major contribution to this work is presented in Sect. 3.3.

3.1 The low velocity molecular clumps in the CB3 and L1157 outflows

Most of the outflows are observable only in the low-J CO transitions. However, a few outflows, especially from Class 0 protostars, stand out because of their emission from molecular species, such as CS, SO, CH_3OH, SiO, etc., usually unobserved in classical outflows. In a few of these chemically rich outflows small molecular clumps (≤ 0.1 pc) are detected along the lobes. These clumps are at a relatively low velocity ($v \leq 10$ km s^{-1}) with respect to the v_{LSR} and have a rich molecular emission spectrum. The clumps are usually observed in pairs in the two lobes; hence it is generally believed that the clumps observed in outflows are generated by episodic mass loss of the driving protostar. However, to date, there is not a detailed modelling and understanding of the role of clumpiness in outflows. The aim of this thesis is to investigate the origin and

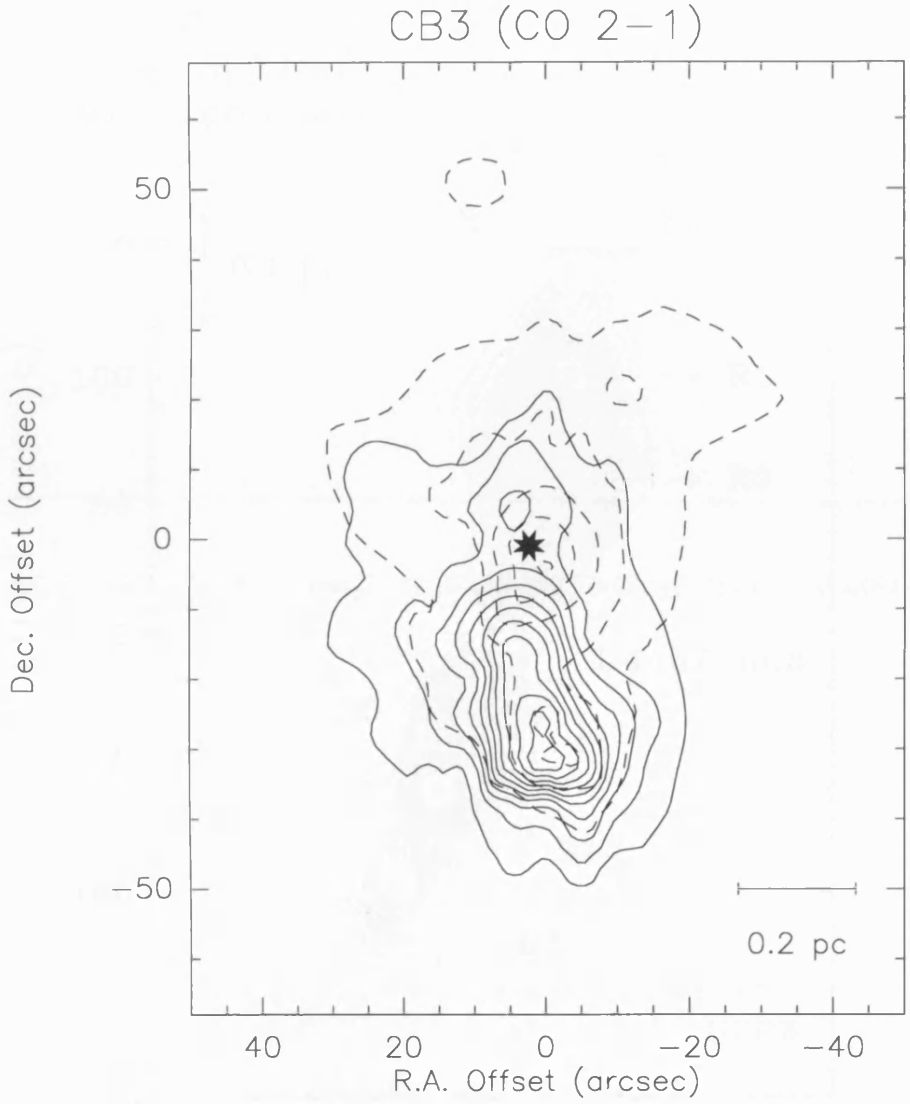

Figure 3.1: CO (2–1) map of the CB3 outflow (Codella private communication). Velocity intervals are form -58 to -40 km s^{-1} for the blue lobe (continuous line) and from -37 to -27 km s^{-1} for the red lobe (dashed line). First contour is 4 K km s^{-1} and the contour spacing is 6 K km s^{-1}. The empty circle at the top right shows the IRAM beam (HPBW), while the black star stands for the coordinated of the 1-1300 μm continuum emission source as measured by Launhardt & Henning (1997).

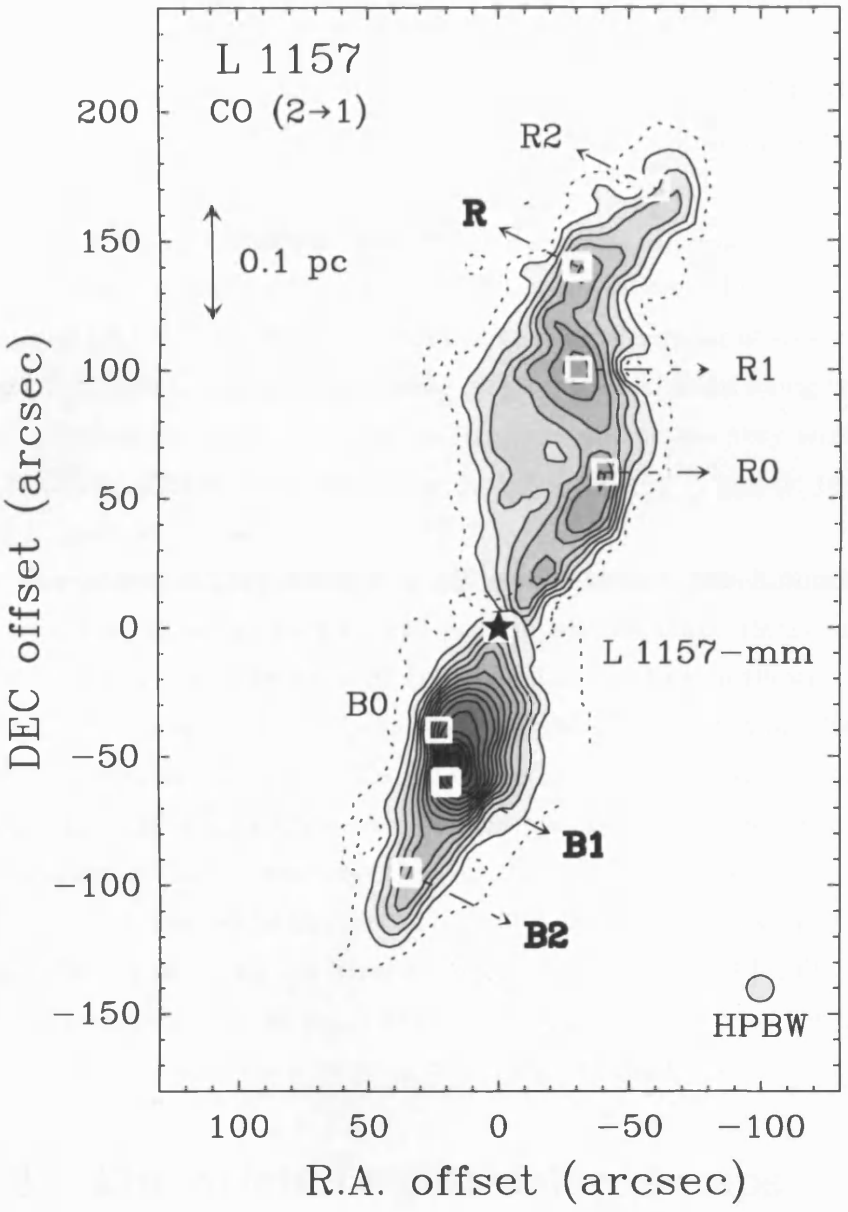

Figure 3.2: CO (2–1) map of the L1157 outflow (figure from Bachiller et al. (2001)). Velocity interval are form -20 to 2.7 km s^{-1} for the southern (blue) lobe and from 2.7 to 28 km s^{-1} for the northern (red) lobe. First contour and contour spacing are 11 K km s^{-1}. The white squares mark the position of the clumps and the star the position of the L1157–mm source.

the nature of the low velocity molecular clumps detected along outflows by the use of a physical and chemical model that simulates the clump formation and its subsequent interaction with the outflow.

In particular, we concentrate on two outflows, CB3 and L1157. CB3 is a Bok globule at a distance of 2500 pc (Launhardt & Henning, 1997) associated with star formation. It hosts an intermediate–mass YSO driving a 4 $M_{\odot}$ outflow with a mechanical luminosity of 5.6 $L_{\odot}$. In Fig. 3.1 the integrated line wings map of the CO (2–1) transition is shown. The outflow has been mapped with the IRAM 30–m telescope in quite a number of species (Codella & Bachiller, 1999b) and four molecular clumps are identified along the main axis. The physical conditions derived in the four clumps are very similar (Codella & Bachiller, 1999b) with density $\sim 5{\times}10^5$ - 10^6 cm^{-3}, kinetic temperature $\sim$ 100 K and size of the clump $\sim$ 0.12 pc.

The nearby L1157 outflow is associated with a low–luminosity (11 $L_{\odot}$) Class 0 star at a distance of 440 pc (Umemoto et al., 1992) and it is considered to be the prototype of the chemically active outflows. It has been extensively mapped at millimetre wavelengths (Bachiller et al., 2001), showing a rich molecular spectrum. The CO emission shows a clear bipolar structure (see Fig. 3.2) with six low velocity clumps located in the two lobes: three clumps are in the red lobe and three in the blue lobe. The best defined clump, called B1, is located in the blue lobe and it is has a density of $\sim 5{\times}10^5$ cm^{-3} (Bachiller et al., 2001), a kinetic temperature of 80 K (Tafalla & Bachiller, 1995), and a size $\sim$ 0.04 pc. The physical conditions derived for B1 show that apart from its size it is similar to the clumps along CB3.

3.2 The origin of molecular clumps

To investigate the origin of the low velocity molecular clumps detected along outflows, we used a physical and chemical model that simulates the clump formation and its interaction with the outflow. Two scenarios for the formation of the clumps have been investigated:

1. The clumps are pre–existing before the outflow. For example, they may be either the remnant material of the collapsing parent cloud or they may

be completely independent from the star formation process, but present homogeneously in the dark molecular cloud (e.g. Falle & Hartquist 2002; Morata et al. 2003; Garrod et al. 2005). In this scenario we observe these clumps in association with molecular outflows because, as the outflows travel through the molecular cloud, they interact with the clumps and shock them.

2. The cloud material is homogeneous and low in density but, as an episodic outflow forms, its interaction with this homogeneous material will lead to a compression and increase in temperature (with subsequent evaporation of the grains mantles) in localized region only, hence the observed clumpiness (e.g. Arce & Goodman 2001; 2002 and reference therein). In this scenario, the clumps are a direct manifestation of the episodic nature of outflows.

Note that these two scenarios do not necessarily exclude each other: in fact, the morphology of the regions where outflows and jets propagate have a very complicated geometry and structure by their very nature.

The chemical model used is the UCL model already presented in Sect. 2.2.1. As a reminder, the model is a two–phase calculation: phase I simulates the formation of the clumps from diffuse gas and phase II simulates the effect of the outflow on the gas and dust. The model is time–dependent and evolves for about 10^6 yr in phase I and for 10^5 yr in phase II. In scenario 1 we have investigated both a uniform and homogeneous clump and a clump with a density structure. In phase I the clump is formed by gravitational collapse from the diffuse gas within the molecular cloud. In phase II after the initial increase of the temperature to ($\sim$ 100 K), the temperature can remain constant or enter a shocked phase with a higher temperature $T \sim 1000$ K and then cools down to 100–200 K. In scenario 2, the outflow impacts on a dark molecular cloud, of density $\sim 10^4$ cm^{-3}, and induces the formation of clumps. In this case we use phase I of the model to simulate the formation of the dark cloud, and phase II to simulate the formation of the clumps due to the impact of the outflow. During phase II, the gas and dust temperatures increase to 100 K or the temperature enters a shocked phase with a higher temperature and

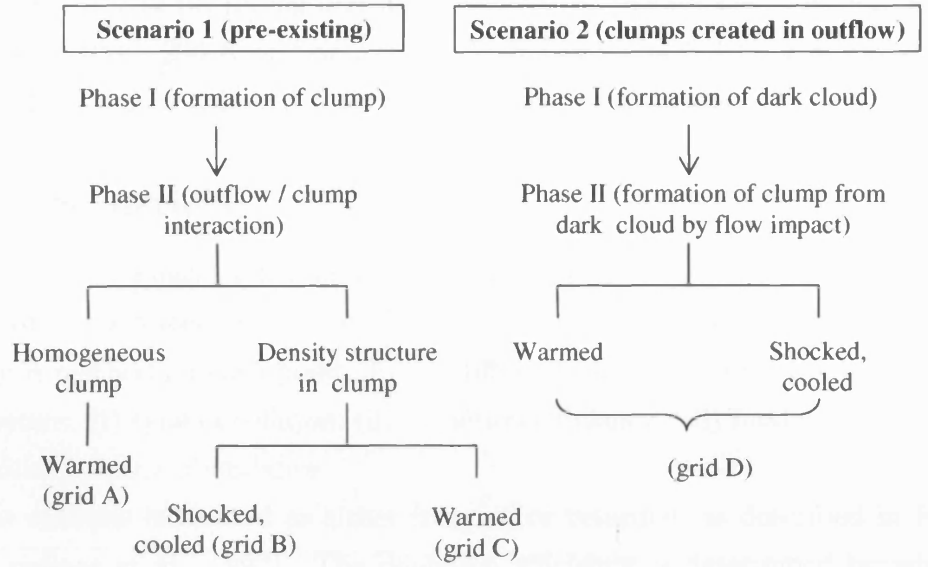

Figure 3.3: A flow diagram of the two scenarios as treated by the chemical model.

subsequent cooling.

In summary, four grids are considered:

- Grid A: a pre–existent clump at uniform single density warmed by the outflow.
- Grid B: a pre–existing clump with a density structure shocked by the outflow;
- Grid C: a pre–existing clump with a density structure warmed by the outflow;
- Grid D: a clump formed and warmed or shocked by the outflow impact;

In Fig. 3.3 a graphical scheme of the four grids is presented. For each grid different conditions are investigated, changing the model parameters within a reasonably large parameter space. To impose some constrains on the parameters range, we adopted the physical parameters derived by Codella & Bachiller (1999b) for the clumps observed along the CB3 outflow, namely a size for the

final clump of 0.12 pc, a final density of about 10^5 – 5×10^6 cm^{-3}, a final temperature of 100 – 200 K and an age of 10^5 yr (see Sect. 3.3.1).or retarded In Table 3.1 all the models and their main parameters are listed.

3.2.1 Scenario 1

In phase I of scenario 1 the clump is formed by gravitational collapse from the diffuse gas within the molecular cloud and it is halted when the final density is reached for each point. In the different models we vary the following parameters: (i) type of collapse, (ii) depletion efficiency, (iii) final density, and (iv) initial sulphur abundance.

The collapse is treated as either free–fall or retarded, as described in Eq. 2.2 (Rawlings et al., 1992). The depletion efficiency is determined by what fraction of the gas phase material is frozen on to the grains and undergoes hydrogenation. Several routes of hydrogenation for the most significant species (O, N, C, CO) have been explored. The freeze–out fraction is arranged by adjusting the grain surface area per unit volume, and assumes a sticking probability of unity for all species. The fraction of material on grains is then dependent on the product of the sticking probability and the amount of cross section provided per unit volume by the adopted grain size distribution. This product (FR in our terminology) was varied so that at the end of phase I, we would have different percentages of ices. Note that as the chemistry is time–dependent, different species form at different times and as a consequence the material frozen out on the grains at any one time is not representative of the whole gas but of selected species (in this case, we chose to monitor frozen CO). The final density is varied in the models from a lower limit of 10^5 cm^{-3} to an upper limit of 5×10^6 cm^{-3}. The initial relative abundance of sulphur is very uncertain (e.g., Ruffle et al. 1999); we chose the solar value as an upper limit and a factor of hundred lower than the solar value as a lower limit.

In this scenario we consider two possibilities: *i)* the clump has a uniform single density, i.e. the chemical model is a single–point model (Grid A), or *ii)* the density within the clump is not uniform so a density structure is present and the model is multi–point (grids B and C). In Grid B and C we adopted the density law derived by Tafalla et al. (2002) for starless cores

Table 3.1: List of the models and their parameters: presence (Y) or absence (N) of non–dissociative shock, final density, final temperature, percentage of freeze–out, initial sulphur abundance and other possible parameters that are different with respect to the other models, i.e. if the collapse is retarded (B=0.1) instead of free–fall (B=1), if all the H_2CO is converted in CH_3OH on ices and if the evaporation is time dependent (TD) instead of instantaneous. For Grid D models the density and temperature are the final ones (at $t = 10^5$ yr).

model	shock	n(H_2) 10^5 (cm^{-3})	T (K)	FR (%)	X(S) (10^{-7})	Note
A1	N	1	210	15	130	
A2	N	1	210	35	130	retarded collapse, B=0.1
A3	N	1	210	11	130	retarded collapse, B=0.1
A4	N	1	210	20	19	
A5	N	10	210	20	130	
A6	N	10	210	30	1.3	
A7	N	10	210	55	1.3	
A8	N	10	210	80	1.3	
A9	N	50	210	25	130	
B1	Y	5–10	110	40	1.3	
B2	Y	5–10	110	60	1.3	
B3	Y	5–10	110	60	1.3	$H_2CO \Rightarrow CH_3OH$
B4	Y	5–10	110	80	1.3	$H_2CO \Rightarrow CH_3OH$
C1	N	5–10	110	40	1.3	
C2	N	5–10	110	60	1.3	
C3	N	5–10	110	60	1.3	$H_2CO \Rightarrow CH_3OH$; TD evap.
D1	N	5–10	110	20	1.3	
D2	N	5–10	110	20	1.3	
D3	N	5–10	110	20	1.3	
D4	N	2.5–5	100	20	1.3	
D5	N	5–10	110	20	1.3	
D6	N	5–10	110	20	1.3	
D7	N	5–10	110	20	1.3	
D8	N	5–10	100	20	1.3	
D9	N	5–10	110	20	1.3	

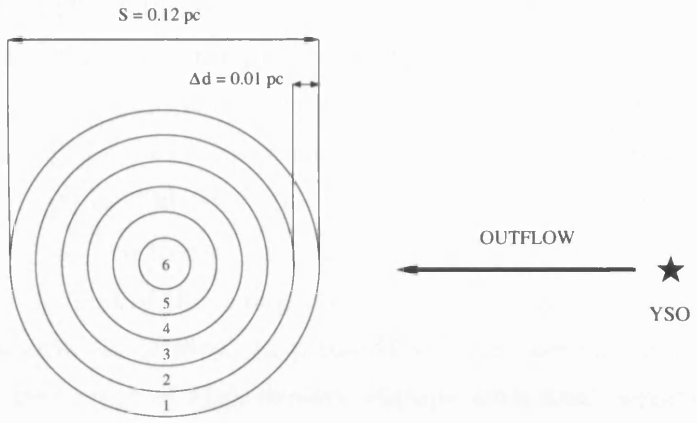

Figure 3.4: A schematic picture (not to scale) of the inhomogeneous clump modelled in Grids B, C and D. The chemical model is in 1–D, hence the chemistry is determined only along one symmetry axis. The geometry is then taken into consideration when estimating the column densities.

$$n(r) = n_o/(1 + (r/r)_o)^{\alpha} \tag{3.1}$$

where r_o and n_o are the largest distance from the center of the core and the peak density, respectively. α is the asymptotic power index and is taken to be $\sim$ 2.5 (see Table 2 in Tafalla et al. (2002)). The clump is divided into 6 shells differing in density, visual extinction, and distance from the (future) outflow. Fig. 3.4 shows a simplified, not to scale, graphical representation of the clump/outflow system.

In phase II the arrival of the outflow is simulated in two ways: *i)* the clump undergoes a non–dissociative shock (Grid B) where the grains are evaporated and where the temperature of the gas reaches 1000 K and stays at this temperature for a short period of time (150 yr or so, as in Bergin et al. (1999)), after which the clump cools down to 100 K; *ii)* the gas and dust temperature increases up to 100 – 200 K (grids A and C) with a subsequent evaporation of the grains which occurs either instantaneously or via time–dependent evaporation (model C3), as in Viti & Williams (1999a).

3.2.2 Scenario 2

Scenario 2 (Grid D) simulates the formation of molecular clumps along a molecular outflow as a direct consequence of the impact of the outflow on a dark molecular cloud. We adopt the density structure of Eq. 3.1 for this scenario as well. Phase I simulates the formation of a dark core from a translucent medium (n = 100 or 500 cm^{-3}) collapsing in free–fall until n= 10^4 cm^{-3} is reached. We chose the freeze–out parameter (FR) so that the abundances of key species at the end of the collapse were consistent with observations of dark clouds (van Dishoeck, 1998b). In phase II we simulate the arrival of the outflow and the formation of high density clumps with final density. We take as free parameters the outflow velocity and the initial distance of the dark cloud to the outflow. The models are listed in Table 3.2; the ranges of velocities and distances were determined by considerations of the values derived for CB3 (Codella & Bachiller, 1999b). Note, however that a high velocity outflow at a too close initial distance to the gas material would not give the clump the time to form and reach the high densities considered (models D2, D3, D6, D9). The density and temperature vary in the following way:

$$n = n_i(r/r_i)^{-3/2} \tag{3.2}$$

and

$$T(r) = T_o(r/r_o)^{-0.4} \tag{3.3}$$

where r_i is the initial distance, T_o is an estimate of the hottest gas ($\sim$ 100 – 200 K) and r_o is the closest (final) distance between the outflow and each shell within the clump that we are modelling, such that at $r_o = r$, $T(r) = T_o$. The initial distance varies of course from shell to shell; the distance between the edge of the clump (shell 1) and the outflow for each model is listed in Table 3.2. The temperature varies with time (and therefore with distance) as in Eq. 3.3 (see Rowan–Robinson 1980 and Viti & Williams 1999b).

Model D1 was also run with the addition of a non-dissociative shock phase (with a temperature of 1000 K for 100 yr, followed by cooling) during the formation of the clump, as in Grid B.

Table 3.2: Model parameters for Grid D. The model number is listed in column 1; column 2 and 3 are the velocity of the outflow and the initial distance between the cloud and the outflow, respectively.

Model	Velocity (km/s)	r_i (pc)
D1	2	0.1
D2	20	0.1
D3	100	0.1
D4	2	0.2
D5	20	0.2
D6	100	0.2
D7	2	0.4
D8	20	0.4
D9	100	0.4

3.3 Comparison between models and observations

The outputs from the chemical models are the fractional abundances with respect to the total number of hydrogen atoms of all atoms and species at each time step and depth. In order to compare the models with the single dish observations of the low velocity clumps the column density is used. In the following subsections we report the methods used to evaluate the column densities both from the chemical model and from the observed transitions. The chemical model is in 1–D, hence the chemistry is determined only along one symmetry axis. The spherical geometry of the clumps is then taken into consideration when estimating the column densities.

3.3.1 Observed column densities in CB3

The CB3 outflow has been mapped with the IRAM 30–m telescope in a number of species by Codella & Bachiller (1999b) and four molecular clumps were

identified along the main axis: N1 with on offset with respect to the driving source of (0″, +40″), N2 with offset (0″, +10″), S2 with offset (0″, -10″) and S1 with offset (0″, -30″). The clumps are shown in the CO (2-1) channel map (Fig. 3.5). Codella & Bachiller (1999b) derived the physical parameters of the gas by means of Large Velocity Gradient (LVG) or Local Thermodynamic Equilibrium (LTE) models. However, in their paper only mean values along the outflow are given. In order to have more precise values we calculated the physical parameters of the gas at the position of the 3 clumps: N2, S2 and S1. N1 is neglected because it is poorly defined. Codella & Bachiller (1999b) identified two main temperature components, one at $\sim$ 20 K, and another at $\sim$ 100 K. In order to take into account this range of temperatures, here we calculated the physical parameters using three reference values of the temperature 20, 100 and 200 K.

SO and SiO have been observed in three lines so an LVG model has been used to constrain the column densities as well as the kinetic temperatures ($T_{\rm kin}$) and the hydrogen densities ($n_{\rm H_2}$). The best fit models indicate $n_{\rm H_2}$ = (3 - 8) $\times$ 10^5 cm^{-3} and $T_{\rm kin}$ $\sim$ 100 - 200 K. For CH_3OH a rotation diagram has been used to estimate the rotational temperature T$\sim$20 K and its column densities N(CH_3OH) $\sim$ 3×10^{15} - 2×10^{16} cm^{-2} (Codella & Bachiller, 1999b). Gas density estimates have also been derived from the methanol emission patterns by measuring line intensity ratios, $n_{\rm H_2}$= 10^5 - 10^6 cm^{-3} (Bachiller et al., 1998). The values of the temperature, H_2 density and molecular column density are reported in Table 3.3. The column densities of the other molecules, observed in a single transition, have been estimated by assuming the lines to be optically thin and in LTE conditions. In this case the column density is given by the formula

$$N = 1.67 \times 10^{14} \frac{Q(T_{rot})}{\mu^2 \nu S} exp\left(\frac{E}{kT_{rot}}\right) \int T_{MB}\, dv \qquad (3.4)$$

where $Q(T_{rot})$ is the partition function, μ is the dipole momentum, ν is the frequency, S is the line strength and E is the energy of the upper level of the transition. The standard partition functions have been used. We calculated the column density for the three reference temperatures 20, 100 and 200 K. For the CO we consider only the case of the T=20 K because the line ratio

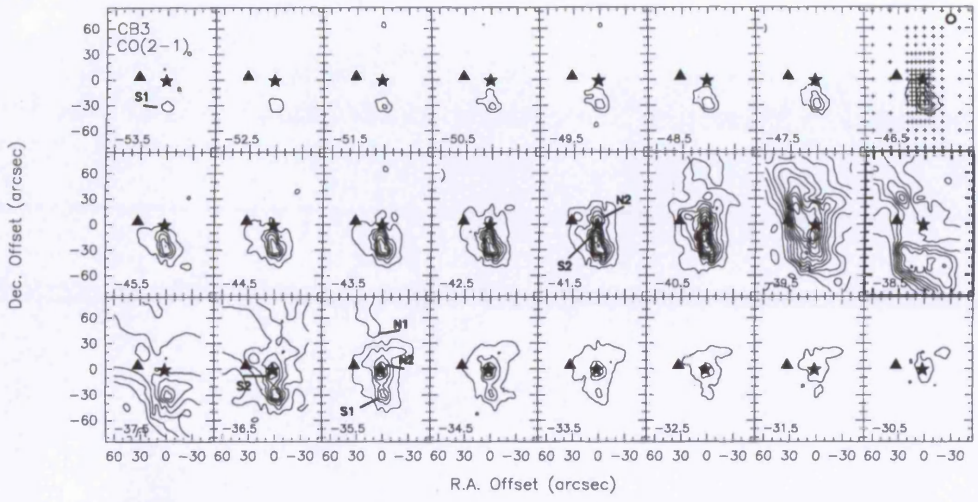

Figure 3.5: Contour map of the CO (2-1) emission towards CB3 (figure from Codella & Bachiller (1999b)). The star stands for the coordinated of the 1-1300 μm continuum emission source as measured by Launhardt & Henning (1997), while the filled triangle is for the coordinates of the NIR source (Yun & Ckemens, 1995). The empty circle in the top right of the panel shows the IRAM beam (HPBW), while the small crosses mark the observed positions. Contours range from 0.75 to 75.75 K km s^{-1} by steps of 2.5 K km s^{-1}. The four clumps are indicated.

Table 3.3: Physical parameters, i.e. column density, temperature and H_2 density derived in the three clumps of the CB3 outflow for SiO, SO and CH_3OH. 1.3(13) stands for 1.3×10^{13}, this notation will be used for other tables of the thesis.

Molecule	Peak	N (cm^{-2})	T (K)	n_{H_2} 10^5 (cm^{-3})
SiO	N2	1.3(13)	20	80
	"	1.3(13)	100	6
	"	1.3(13)	200	4
	S2	1.1(13)	20	50
	"	1.1(13)	100	8
	"	1.1(13)	200	5
	S1	1.7(13)	20	60
	"	1.7(13)	100	5
	"	1.7(13)	200	3
SO	N2	2.3(14)	20	20
	"	2.3(14)	100	4
	"	2.3(14)	200	3
	S2	9.3(13)	20	7
	"	9.3(13)	100	3
	"	9.3(13)	200	3
	S1	1.4(14)	20	80
	"	1.4(14)	100	8
	"	1.4(14)	200	8
CH_3OH	N2	3.0(15)	19	10
	S2	1.5(16)	16	10
	S1	9.3(15)	19	1

Table 3.4: Column densities derived by LTE calculations in the three clumps of the CB3 outflow.

Molecule	Peak	N (cm^{-2})	T (K)	Molecule	Peak	N (cm^{-2})	T (K)
CS	N2	5.1(13)	20	$H^{13}CO^+$	N2	2.3(12)	20
	"	1.4(14)	100		"	9.7(12)	100
	"	2.8(14)	200		"	2.0(13)	200
	S2	8.5(13)	20		S2	2.9(12)	20
	"	2.4(14)	100		"	1.2(13)	100
	"	4.7(14)	200		"	2.5(13)	200
	S1	5.0(13)	20		S1	<2.1(11)	20
	"	1.4(14)	100		"	<8.9(11)	100
	"	2.8(14)	200		"	<1.8(12)	200
H_2S	N2	5.9(13)	20	H_2CO	N2	2.6(14)	20
	"	2.2(14)	100		"	5.9(14)	100
	"	5.7(14)	200		"	1.4(15)	200
	S2	5.0(13)	20		S2	3.2(14)	20
	"	1.8(14)	100		"	7.2(14)	100
	"	4.8(14)	200		"	1.8(15)	200
	S1	<2.3(12)	20		S1	1.7(14)	20
	"	<8.4(12)	100		"	3.8(14)	100
	"	<2.2(13)	200		"	9.5(14)	200
SO_2	N2	6.7(12)	20	OCS	N2	<4.8(13)	20
	"	5.9(14)	100		"	<6.7(12)	100
	"	1.7(15)	200		"	<8.9(12)	200
	S2	7.9(13)	20		S2	8.3(14)	20
	"	6.9(14)	100		"	1.2(14)	100
	"	2.0(15)	200		"	1.5(14)	200
	S1	4.5(13)	20		S1	<4.8(13)	20
	"	4.0(14)	100		"	<6.7(12)	100
	"	1.2(15)	200		"	<8.9(12)	200
CO	N2	4.4(16)	20				
	S2	7.4(16)	20				
	S1	1.2(17)	20				

between CO (1–0) and (2–1) indicates an excitation temperature of 15 – 20 K for the high–velocity gas throughout the outflow. The values of the column density for all the observed molecular species derived by LTE assumption are reported in Table 3.4. As one can see from the table the uncertainty on the temperature means that the column densities are only accurate within a factor of 10.

Note that with LVG calculations it is not possible to separate the effects on the excitation of the density and temperature. Moreover, LVG calculations do not take into account any correction due to the different beam filling factors at the three wavelengths of the observed transitions. As discussed by Codella & Bachiller (1999b), if the source sizes were to be definitely smaller than the three beam widths, the LVG model would lead to an overestimate of the excitation conditions: $T_{\rm kin}$ and $n_{\rm H_2}$ should be reduced by factors of about 2, while the column densities by a factor of 10.

For the comparison with the models we decide to consider the mean value of the molecular column density calculated for the three clumps and the three temperatures.

The kinematic age of the outflow is estimated to be between 2×10^4 and 5×10^5 yr, and it has been derived by comparing the positions of the farthest clumps, with respect to the driving source, assuming that the material travelled from the center to its present location with a typical observed velocity of the SiO clumps, $\sim$ 2 km s^{-1}, and correcting for the projection effect, given an inclination to the plane of sky of 30 deg.

3.3.2 Theoretical column densities

The theoretical column densities are calculated using the following formula

$$N = XLnf \tag{3.5}$$

where X is the fractional abundance of the species, L is the length of the clump (assumed to be spherical), n is the density and f is the weighted beam dilution factor. This formula is valid for the single point models (Grid A). For the multi–point models (Grids B, C, and D) the column density is calculated

Table 3.5: Volume, radius and angular dimension of equivalent sphere for the 6 shells of the multi–point models of the CB3 clumps.

Shell	Volume 10^{50} (cm^3)	R_{eq} (pc)	θ_s (arcsec)
1	166.1	0.051	8.465
2	99.67	0.043	7.145
3	54.15	0.035	5.825
4	24.61	0.027	4.472
5	8.615	0.019	3.152
6	1.230	0.010	1.650

adding the contribution of each shell of the clump, using the formula

$$N = \sum_{i=1}^{6} X_i L_i n_i f_i \tag{3.6}$$

where i is an index indicating the shell, X_i is the fractional abundance of species in shell i, L_i is the length of each shell, n_i is the density in shell i and f_i is the weighted beam dilution factor of the shell. The beam dilution factor is defined as

$$f = \frac{\theta_s^2}{\theta_s^2 + \theta_b^2} \tag{3.7}$$

where θ_s is the angular dimension of the source and θ_b is the HPBW of the telescope. For sources much smaller than the beam $\theta_s \ll \theta_b$ and $f \rightarrow \theta_s^2/\theta_b^2$, while for sources much larger than the beam $\theta_s \gg \theta_b$ and $f \rightarrow 1$.

The angular dimension of the clumps observed in the CB3 outflow is ~10 arcsec (0.12 pc at a distance of 2500 pc) while the IRAM HPBW ranges between 10 and 25 arcsec. For single–point models, depending on the transition, the source can be smaller or greater than the telescope beam, while for multi–point models the beam dilution factor is always smaller than unity. In order to evaluate the dilution factor for the multi–point models we calculate the angular dimension of the equivalent sphere with a volume equal to the volume of the shell. The results are reported in Table 3.5.

Table 3.6: Column densities (in cm^{-2}) of selected species for some models from Grid A versus the column densities observed in CB3 (Column 6).

	A1	A4	A6	A8	Obs
CS	6.2(13)	1.2(13)	9.8(13)	1.1(14)	1.9(14)
H_2CO	1.1(16)	1.2(16)	3.5(16)	1.4(17)	7.3(14)
H_2S	1.8(17)	2.6(16)	1.1(18)	1.4(16)	2.6(14)
SO_2	4.1(16)	8.1(15)	1.1(19)	2.8(16)	7.5(14)
OCS	1.6(15)	2.5(14)	8.1(17)	1.6(14)	3.7(14)
SO	2.2(17)	3.2(16)	1.0(19)	3.8(15)	1.5(14)
CO	8.7(17)	8.7(17)	1.4(20)	9.8(18)	7.9(16)
CH_3OH	6.0(14)	8.0(14)	2.0(17)	2.9(16)	9.1(15)

3.4 Chemical model results

In this section we present the results of the chemical models for all the four grids and we compare them with the observations. We remember here that the observed column densities are the mean values of the column densities of the three clumps observed along the CB3 outflow for the three temperatures (20, 100, and 200 K).

3.4.1 Grid A

In Table 3.6 we list the column densities at 10^5 yr, estimated from some of the models of Grid A as compared to the observations, while Fig. 3.6 shows the column densities of selected species as a function of time for some models.

From the table it is clear that the models from Grid A do not fit the observations. This is probably a consequence of the oversimplification introduced by the one–density component.

Nevertheless, general trends do emerge from this simple grid of models:

1. a depleted sulphur initial abundance, rather than a solar one, is preferred; we note from our results that, apart from CS (whose abundance is mainly affected by the degree of depletion) other sulphur species, such as SO, are far too abundant if the initial sulphur is solar. A similar result has

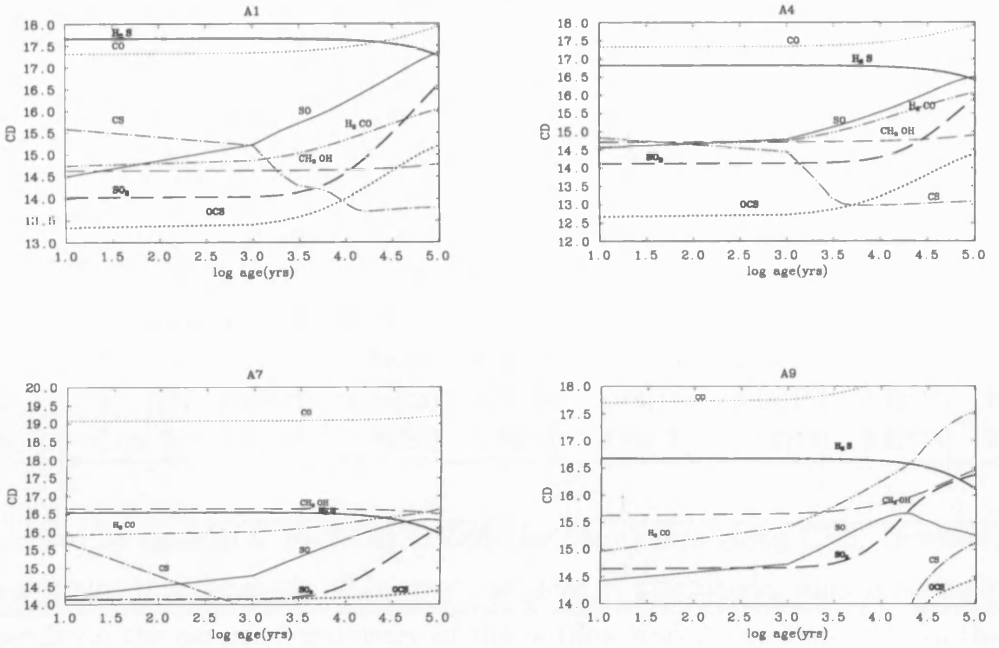

Figure 3.6: The column densities (in cm^{-2}, logarithmic scale) of a selection of species relative to hydrogen over time for selected models from Grid A.

been found also in previous studies (Caselli et al. 1994; Viti et al. 2003). Ruffle et al. (1999) suggested that the depletion of sulphur can be due to the fact that in a collapsing translucent clump a large fraction of the gas–phase sulphur is in the form of S^+. Ions collide more rapidly with grains and may stick more efficiently to them than neutrals; so, as a clump collapses, sulphur may become depleted in it more rapidly than elements that are not primarily ionized in translucent material.

2. Freeze–out on to grains must be effective at the densities considered here; probably at least half of the gas is depleted on to grain by the end of phase I.

3. None of the species seem to be particularly affected by the type of collapse employed; for simplicity we will then adopt a free–fall collapse for the remainder of our grids.

So far, we looked at the column densities at 10^5 yr, the kinematic age

Table 3.7: Column densities (in cm^{-2}) for selected models from Grids B, C, and D at $\sim 10^5$ yr vs observed column densities

	B1	B2	B3	C1	C2	D1	D8	Obs
CS	1.66(15)	1.24(15)	4.76(15)	5.79(13)	1 .60(14)	8.98(15)	9.64(15)	1.9(14)
H_2CO	2.32(17)	2.64(17)	1.73(17)	4.24(16)	1.20(17)	2.78(15)	2.74(15)	7.3(14)
H_2S	5.94(14)	5.97(14)	2.52(14)	4.00(15)	1.50(15)	4.90(13)	1.15(14)	2.6(14)
SO_2	5.64(15)	5.93(15)	2.59(15)	3.82(15)	6.56(15)	1.15(13)	2.13(13)	7.5(14)
OCS	1.61(14)	1.95(14)	6.15(13)	2.10(13)	2.71(13)	2.76(14)	2.77(14)	3.7(14)
SO	2.74(13)	3.21(13)	1.34(13)	8.89(14)	6.74(13)	2.43(13)	7.79(12)	1.5(14)
CO	1.11(18)	9.40(17)	1.16(18)	2.17(18)	1.56(18)	6.15(18)	6.32(18)	7.9(16)
CH_3OH	6.05(15)	6.40(15)	1.22(16)	5.48(15)	6.20(15)	2 .12(14)	2.62(14)	9.1(15)

estimated by Codella & Bachiller (1999b) for the clumps along CB3. However, this estimate may be easily off by over one order of magnitude, since it strongly depends on the assumed geometry of the outflow and it can thus vary in the 2×10^4 – 5×10^5 yr range (Codella & Bachiller, 1999b).

From Fig. 3.6, we can see that certain species, such as CS, H_2CO, and SO_2 are very time–dependent; so for example the SO_2 column density is close to the observed one if the clump is less than 10^4 yr old, while CS is best matched at later times (see Model A9); if the density is closer to 10^6 cm^{-3} and the sulphur initial abundance is low (models A7 and A9 in Fig. 3.6) SO is reasonably matched before 3000 yr. These brief considerations underline the importance of constructing a clump with a density structure since not only different species match observations at different densities, but also the degree of freeze out (which determines a great deal of the time dependent chemistry) is density dependent.

3.4.2 Grids B, C and D

As these grids share the same density structure, we discuss their trends together. The column densities for most models at 10^5 yr are listed in Table 3.7.

Table 3.7 shows that varying the percentage of gas depleted in the grains in Grid B (e.g. B1 vs. B2) does not significantly affect the abundances of most species, while in Grid C the abundance of sulphur–bearing species can vary by

up to one order of magnitude.

More significant differences are found between models from Grid B and those from Grid C, especially among the sulphur–bearing species; this is not surprising as sulphur–bearing species are known to be good tracers of high temperature gas (e.g. Hatchell & Viti 2002; Hatchell et a. 1998). We find that CS is as much as two to three orders of magnitude more abundant in Grid B than in Grid C models while H_2S, SO and OCS vary by two orders of magnitude at most; H_2S is the driving species for the sulphur chemistry: it is enhanced on the grains during freeze out (via hydrogenation of sulphur) and it is then evaporated and dissociated during phase II; since it is easily dissociated at high temperatures, it is, of course, more abundant in Grid C models (where the absence of a high temperature phase slows down its dissociation). A faster dissociation of H_2S in Grid B increases the abundance of other sulphur species, in particular we note OCS (an otherwise underabundant species). SO_2, on the other hand, does not seem to be affected as much.

We conclude that, if the clump is pre–existing, then we should be able to easily discern whether it has undergone a high temperature phase or not using sulphur–bearing species as tracers: moreover, if we assume that once the outflow has reached the clumps, non–dissociative shocks must occur, then sulphur–bearing species can indeed be used as chemical clocks in order to determine the age of the outflow/clump system, as proposed also by Codella & Bachiller (1999b) and Bachiller et al. (2001) for the high–velocity outflowing gas.

As expected, the differences between Grids B, C, and Grid D involve more species. In particular, we find that, apart from sulphur bearing species, CH_3OH is a good tracer of the different scenarios. CH_3OH is not easily made in the gas–phase and is thought to be mainly formed on the grains via hydrogenation of a fraction of CO (Millar & Hatchell, 1998) and possibly H_2CO. In a high temperature environment, CH_3OH has an alternative route of formation via water; in fact, we note from Table 3.7 that, at equal freeze out, methanol is higher in the models from Grid B than in those of Grid C (cf. B1 and C1), although at high freeze out they are comparable (cf. B2 and C2). This implies that a high abundance of CH_3OH depends more strongly on the amount of

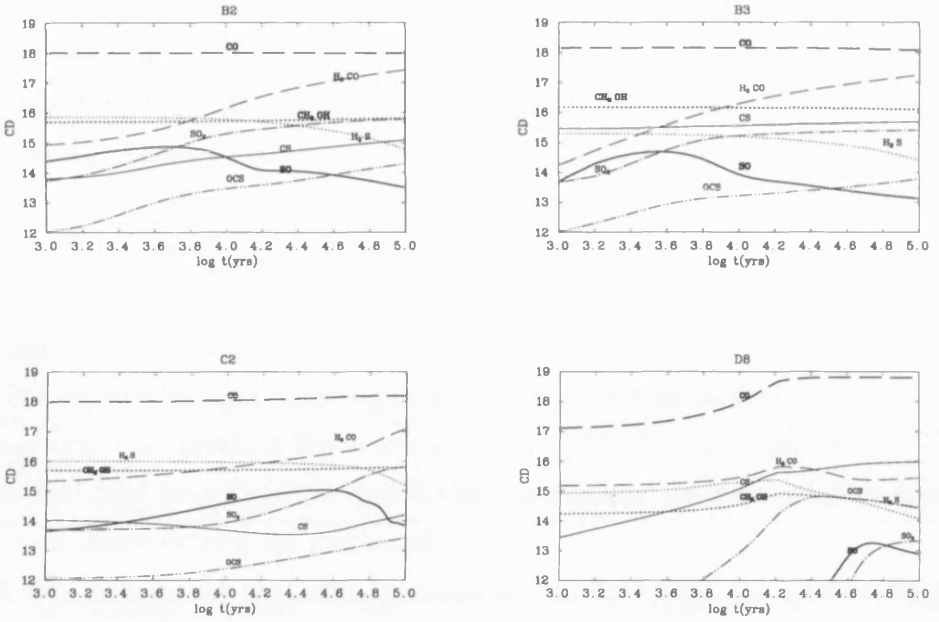

Figure 3.7: As in Fig. 3.6 for selected models from Grid B, C and D.

CO on the grains than on whether a high temperature phase has occurred.

For the same reason, Grid D models have a low abundance of CH_3OH as the formation of the clump took relatively little time, hence depletion and hydrogenation onto the grains was not very effective (Rawlings et al., 1992). If a high temperature phase is included for D1, the methanol abundance does indeed increase, but all the sulphur–bearing species increase by over one order of magnitude.

Methanol and sulphur–bearing species may therefore be the ideal candidates to determine whether the clumps originate as a consequence of the outflow or whether they are, at least partially, pre–existing.

Since the age of the observed gas is uncertain, we also show in Fig. 3.7 the behaviour of selected species as a function of time for some of the models listed in Table 3.7. The chemistries of some species, such as, in fact, the ones which show most discrepancies with the observations, are highly time dependent; for example, H_2CO, and some sulphur species, can be almost two orders of magnitude lower in abundances at early times.

3.5 Model comparisons with CB3

At first sight, from Table 3.6 and 3.7, it appears that none of the models succeeds in reproducing all the observed column densities within the observed uncertainty (taken to be one order of magnitude, see Sect. 3.3.1) at the estimated age of the outflow of 10^5 yr. However, some general considerations can be made. Results from Grid A suggest that a 0.12 pc clump at uniform density is a too simplified model and that a density structure is present inside the large IRAM beam.

Grid D fails to reproduce important species such as methanol and sulphur species and it is therefore the worse matching grid; Grid C improves over Grid D but still fails, in general, to match the observations for some sulphur species and, to a lesser extent, for methanol.

A first conclusion that can be made is therefore that the chemically rich clumps along CB3 can not be formed completely by compression of the gas due to the advent of the outflow. This, of course, implies that the high density of the clumps must have been reached before the advent of the outflow. This preliminary conclusion seems to be in contradiction with the conclusion by Arce & Goodman (2001) that the outflow clumps are the product of the sweeping up of ambient gas. However, their assumption is that the ambient gas is homogeneous, at a density of $\sim 5{\times}10^3$ cm^{-3}, and that the outflow will sweep–up a volume of ~ 0.5 M$_\odot$, maintaining the same density of pre–existing cloud material so, effectively, from a chemical point of view, the clump is indeed pre–existing the outflow/star system, as the final density was reached without the intervention of the outflow. In this picture the morphology of the swept–up ambient gas and not its high density is a manifestation of the episodic nature of the outflow.

Grid B models seem to be the best, in particular B2 gives the closest match with observations, within an order of magnitude (i.e. within the observed error bars, see Sect. 3.3.1): apart from CO, all species are well matched for t$\geq$ 10^4 yr, although H_2CO is definitely best matched at $t \leq 10^4$ yr. Although not obvious from Fig. 3.7 (but evident from Table 3.7), the CO abundance in Grid B is about half the value in Grid C, due to the presence of a high

temperature gas phase. However this difference did not increase by increasing the high temperature phase to 500 yr (models not shown), as opposed to 150 yr as assumed in Grid B.

In general, we find that the theoretical abundance of H_2CO is overabundant with respect to the observations. One of the formation routes for H_2CO is the hydrogenation of CO, HCO and HCO^+ on the grain mantles. We tried a model, B3 (also shown in Fig. 3.7), similar to B2 but where *i)* frozen H_2CO is converted into methanol (a possible hydrogenation), *ii)* frozen HCO and HCO^+ remain unaltered, upon depletion, *iii)* none of the carbon that freezes onto the grains hydrogenates into methane (unlike in previous models, where a percentage of carbon atoms became CH_4); the latter reaction is important because some of the H_2CO formed during the warm phase is formed by the reaction of water with CH_3 that comes from the dissociation of CH_4. We also computed a model, similar to B3, but with higher freeze out (B4, not shown in Fig. 3.7). Although the final (at 10^5 yr) fractional abundance of H_2CO is lower than in B1 or B2, we notice that in B3 and B4 the CS abundance is too high.

We can conclude therefore that the most likely scenario of the clumps observed along the outflow is a scenario where the clumps are pre–existing the advent of the outflow as a structure at high density, and undergo a high temperature phase (caused by a non–dissociative shock) when the outflow arrives.

There are several reasons why Grid B models do not always quantitatively match the observations: for example, so far we have only looked at the total column density as coming from the whole clump. However, as shown from the results of Grid A, we know that the clumps must be formed by several density components; the density structure adopted here is believed to be representative of low–mass starless cores (Tafalla et al., 2002) but it is likely that the density profile for the starless, small clumps considered here have a different structure. It is therefore worth making some general considerations on the possibility that different species are emitted from different components of the gas.

Fig. 3.8 shows, at two different epochs, the fractional abundances of selected species as a function of the density for the model B2. From this figure it

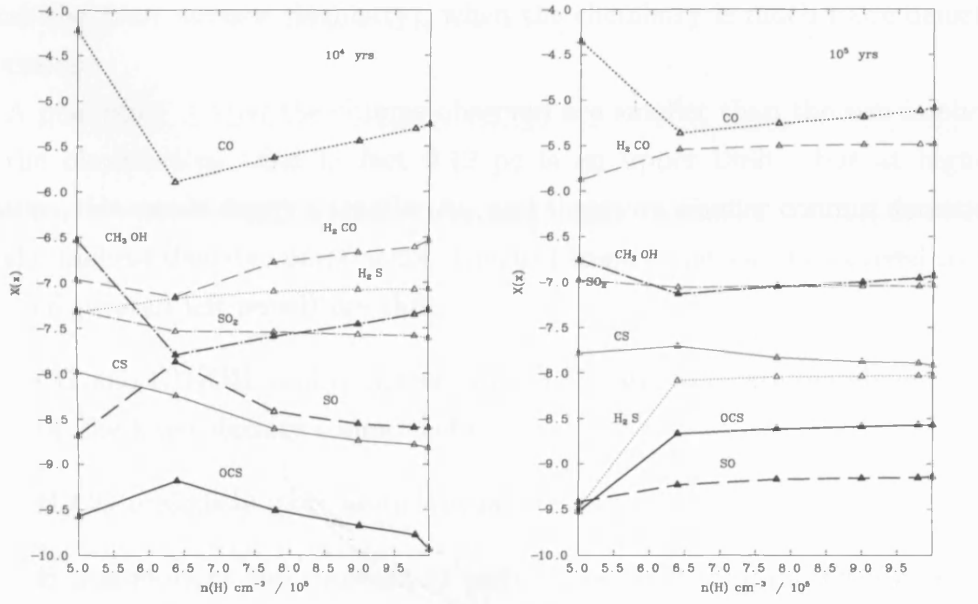

Figure 3.8: Fractional abundance of selected species as a function of density for Model B2 at 10^4 yr (left) and 10^5 yr (right). The diamond marks indicate the densities at which each shell was computed. The points are joined for clarity.

is clear that if the clumps are as old as 10^5 years the emission comes effectively only from a two-components density structure, one at $\sim 5\times10^5$ cm^{-3} and the other at $\sim 10^6$ cm^{-3}. It may be that some gas comes from a lower density component but our 'edge' (lower) density was determined by imposing a upper density of 10^6 cm^{-3} (as derived by observations, see above). In fact, if we look at CO it seems as it is indeed the lower density component that is inconsistent with the observations. Note that although from this figure it seems as if an homogeneous gas at 10^6 cm^{-3} would have matched the observations, this is not the case at earlier times, and overall during the collapse phase (which determines the grain surface chemistry), when the chemistry is much more density dependent.

A possibility is that the clumps observed are smaller than the size implied by the observations (and in fact 0.12 pc is an upper limit), but at higher density: this would imply a smaller A_V and therefore smaller column densities for the highest density components. General trends that can be derived from Fig. 3.8 (overall left panel) are that:

1. CO and CH_3OH, and to a lesser extent CS and SO_2, are mainly emitted by the lower density components.

2. H_2CO is slightly more abundant in the highest densities parts.

3. H_2S is more or less constant at early times, while SO and OCS seem to be highest at intermediate densities. At 10^5 years, H_2S is mainly emitted from the highest density component.

Finally, it is not excluded that each clump observed by Codella & Bachiller (1999b) does in fact contain substructures, not resolved in the single dish observations because of the large distance of the source.

3.6 Another test case: L1157

Here we briefly compare our models with the the clumps observed in L1157 outflow. This outflow will be the subject of a detailed study in Chapter 5. Bachiller et al. (2001) have mapped the bipolar outflow in many molecular

Table 3.8: Column densities (in cm^{-2}) of selected species for B2 and D2 versus the observed column densities of the L1157 clumps.

	B2	D2	L1157
CS	1.15(14)	3.07(15)	2.7(14)
H_2CO	4.96(15)	8.57(14)	3–8(14)
H_2S	1.94(15)	5.53(13)	3.9(14)
SO_2	6.92(14)	6.40(12)	3.0(14)
OCS	1.00(13)	1.15(14)	5(13)
SO	1.04(14)	3.64(12)	3.5(14)
CO	3.28(17)	2.10(18)	1.4(17)
CH_3OH	1.72(15)	1.17(14)	0.5–2.6(15)

emission lines with the IRAM–30m telescope and they found a very rich chemistry. In particular, they detect six small ($\sim$ 0.04 pc) clumps in the two lobes. The best defined clump, called B1, has a density of $(3 - 6)\times10^5$ cm^{-3} and a kinetic temperature of $\sim$ 80 K (Tafalla & Bachiller, 1995), so, apart from its size, it is comparable to the clumps along CB3 and can therefore be briefly compared with our model results. If the origin of these clumps is similar to those observed along CB3, then their smaller size supports the possibility that the clumps along CB3 are smaller than the size implied by the observations due to the distance of the outflow (L1157 is only 440 pc away while CB3 is at 2500 pc).

Table 3.8 compares the column densities (recalculated with Eq. 3.6 as if coming from a smaller size) of our best–matching model (B2) at 10^5 yr and of D2, with the derived column densities. Table 3.8 clearly shows that the match between B2 and the observations improves as the size of the clump is reduced. Grid D is still unable to match the methanol and most of the sulphur–bearing species confirming the results obtained for CB3.

3.7 Conclusions

A time–dependent chemical model of the chemically rich clumps observed along outflows has been presented. This preliminary study was aimed at finding some observable tracers that could help us understand the origin of the clumps with respect to the outflow. The models have been compared with the observations of the clumps observed along the CB3 outflow. The general conclusions are as follow.

1. The initial sulphur abundance of the gas forming the clump can not be solar. We find a depletion factor of $\sim$ 100, confirming the findings of other studies (Ruffle et al., 1999).

2. A substantial freeze–out must occur during the formation of the clump, regardless of its mode of formation.

3. Our models indicate that the most likely explanation for the outflow clumps is that they are pre–existing, meaning only that their high density is, at least partly, reached prior of the advent of the outflow. This does not exclude the general explanation that the outflow clumps are mainly made of swept–up ambient gas and that therefore the clumps are an indication of the episodic nature of outflows.

4. It is probable that, with the advent of the outflow, not only the temperature of the clumps increases and reaches the one observed, but also the clumps undergo a period of non–dissociative shock (and therefore high temperatures, $\sim$ 1000K).

5. The rich chemistry of the clumps observed along CB3, and L1157, seems to be a consequence of a pre–existing density enhancement (either uniform or already in clumps) and of its interaction with the outflow. The latter, most likely, shocks and accelerates the gas, and possibly, if episodic, induces its clumpiness. This is indicated by the high abundance of methanol and some of the sulphur–bearing species. In fact, these molecules are formed by a combination of freeze–out and surface reactions, and

shock chemistry (see Sect. 1.5.6): both are most efficient when the outflow compresses already dense material during its passage.

6. We find that it is not possible for the outflow clumps to have a uniform high density - a density gradient, in the size implied by single dish observations, is needed in order to account for the observed emission of most species.

7. At late times ($t > 10^4$ yr) H_2CO is always over–abundant by at least a couple of orders of magnitudes. This discrepancy is similar to that found for the clumps ahead of Herbig-Haro objects (Viti et al., 2003). These objects, however, do not share a common chemistry and we find no chemical reason why the abundance of H_2CO predicted by our models should be much larger than apparently observed. A possible explanation may be that the observed clumps are smaller than the size implied by the observations. In fact, when computing the theoretical column densities for smaller sizes (i.e. the clumps of the L1157 outflow), the match between theory and observations improves.

Chapter 4

A detailed modelling of the clump S1 in the CB3 outflow

The work presented in this Chapter has been published in the paper by Benedettini et al. (2006).

4.1 Limitations of the previous approach

In the previous chapter we modelled the low velocity clumps along outflows comparing the column densities derived from chemical models with the ones calculated from single dish observations along the CB3 and L1157 outflows. The shortcomings of such an analysis were that the estimations of the column densities derived from the chemical models, as well as those derived from the observations, suffer from high uncertainties due to the fact that some of the parameters required to calculate them may be unknown. In particular, to estimate the observed column densities, arbitrary assumptions have to be made regarding LTE conditions, excitation temperatures and the lines being optically thin. If more transitions of the same species are available, one can use a LVG model to derive the density and temperature of the emitting gas but even in such cases often the results have a large uncertainty because the observed line ratios are not always sensitive to the temperature or density. On the other hand, the theoretical calculation of column densities from the chemical model required knowledge of the geometry of the emitting region.

However, when dealing with small emitting regions, such as the low velocity clumps along molecular outflows, the observations (usually single dish with a spatial resolution of a few tens of arcsec) do not constrain such geometry.

4.2 The new approach

One way to reduce the number of arbitrary assumptions is to model directly the observed line emission using a radiative transfer model that predicts the line profile. Such a method has been already adopted by other authors for modelling the envelope of low mass protostars (Jørgesen et al. 2004; 2005; Schöier et al. 2002; Doty et al. 2004) and it was found to be a powerful tool to probe the physical and chemical structure of the protostellar envelopes as well as the age of the protostar. In this chapter we attempt such an approach by coupling the time dependent chemical model used in the previous chapter with the radiative transfer model SMMOL (Rawlings & Yates, 2001) described in Chapter 2.

A flow diagram of the method used to compare the observed data with the theoretical models is shown in Fig. 4.1. A first order estimate of the general physical conditions of the clump, such as the size, the density and the temperature, is derived from the observations and used to describe the physics of the phenomenon in the chemical model. The chemical model predicts the fractional abundances; these are given as input to the radiative transfer model together with the density, the temperature and the beam of the telescope, to produce the line profiles that are directly compared with the observed profiles. A χ^2 method is used to fit the profiles of several species and, where possible, of multiple transitions of the same species in order to define the best fit model and attempt to constrain the physical parameters of the emitting gas and the scenario for the formation of the clumps.

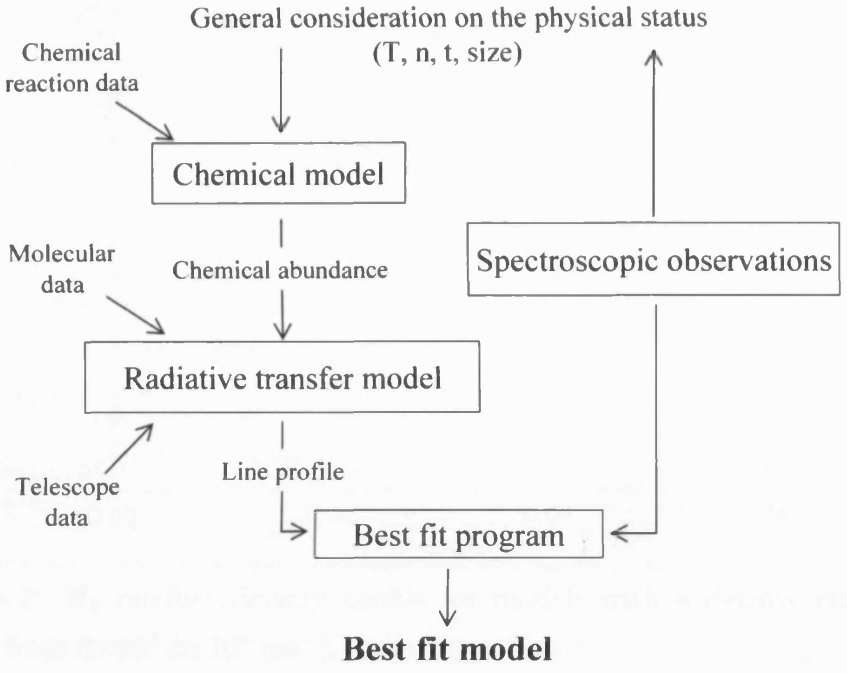

Figure 4.1: Flow diagram of the scheme applied to compare the observed data to the theoretical models in order to derive the best fit model.

4.3 Coupling of the chemical and radiative transfer models

The models used are the UCL time–depended chemical model and the SMMOL radiative transfer model presented in detail in Chapter 2. Since the two models have been developed separately, and they employ a different treatment of the geometry, their inputs and outputs are not compatible with each other. In particular, the output of the chemical model is a single file containing the fractional abundances of all the species, the density and the temperature for each time step. For the models with no uniform density (Grid B, C and D) the density structure has been modelled dividing the clump in 6 shells, thus for each model a file for each of the 6 points is produced. On the other hand, the SMMOL code requires as input for each molecule a single file per time step with at least 50 points along the radius of the clump with the relative density, temperature, chemical abundance and velocity, thus a regridding to account

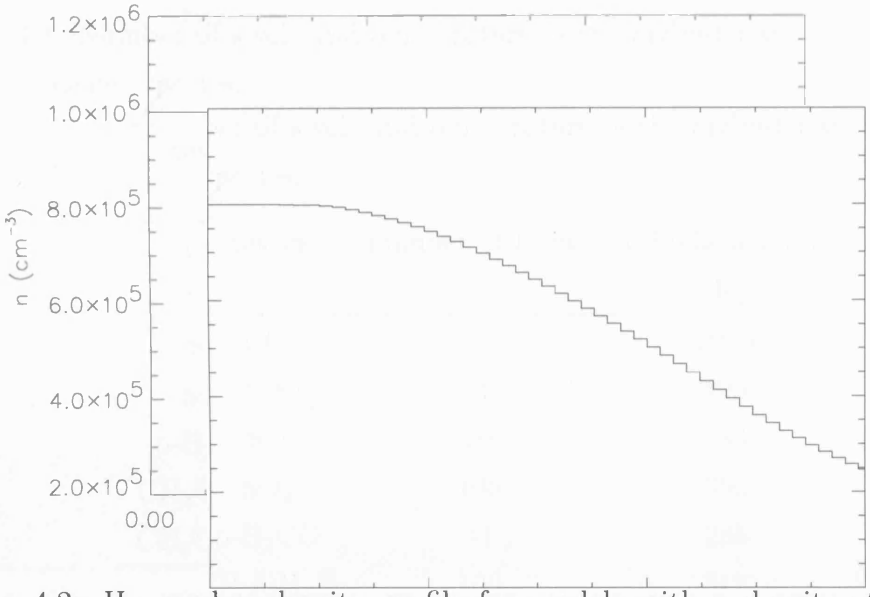

Figure 4.2: H_2 number density profile for models with a density structure ranging from 5×10^5 to 10^6 cm^{-3}.

for the different geometries of the two codes is required.

To reorganize the output of the chemical model in a format suitable for the radiative transfer model, two programmes were developed. The first program reads the output of the chemical model (one file for the single–point models and six files for the multi–point models) and extracts a selected set of species. As output it produces a file for each species with the chemical abundance, the density and the temperature and the turbulent velocity of each point and each time step. The second program reads this output and interpolates the fractional abundances, the density and the temperature of the 6 points to build a grid of 50 or 100 points following the profile of the clump. The output is a file for each species and each time step, that is used as input for the radiative transfer code. An example of the density profile for a model with a density structure ranging from 5×10^5 to 10^6 cm^{-3} is shown in Fig. 4.2.

Many tests have been done in order to solve the problems encountered in the coupling of the chemical and the radiative transfer models. In particular, spurious spikes were present in the profile of several lines for the models with density and temperature profiles. The tests demonstrated that the spikes were due to a too sharp variation of the physical parameters (density, temperature

Table 4.1: Number of levels and temperature of the highest level for the modelled molecular species.

species	number of levels	T(highest level) (K)
CO	31	1900
CS	21	493
SO	70	583
SO_2	198	356
p-H_2CO	41	285
CH_3OH–E	100	513
CH_3OH–A	89	523

and chemical abundance) between two adjacent points. We did several tests changing the number of points along the radius of the clump from 50 to 100 points and we find that for simple molecules, such as CO and CS, 50 points were sufficient while for more complex species, such as CH_3OH and SO_2, a denser grid was necessary in order for the radiative transfer code to correctly converge; in those cases a grid of 100 points was used.

Several tests were devoted to verifying that the number of energy levels for each molecule considered in the radiative transfer model was adequate for modelling the high temperature ($T \sim 100$ K) gas of outflows. In principle, to calculate the level populations one might want to consider as many energy levels as possible. In practice, the molecular data, especially the collisional coefficients, are known only for the lowest levels and the more levels one considers the more the calculation is time consuming. In fact, to correctly calculate the level populations at a certain temperature one can consider at least all the levels till the one whose energy is similar to the gas temperature. The list of the number of energy levels we used for each species together with the temperature of the highest level is reported in Table 4.1.

To correctly follow the evolution of the clump, the chemical model requires a dense sampling of the time; therefore it produces a large number of time steps, in our case 197 time steps covering 10^5 yr for phase II of the model.

However, the physical conditions between near time steps are very similar and it is unnecessary and much too time consuming to run the radiative transfer code for all the time steps. Therefore, the radiative transfer code has been run only for a selected subset of time steps of each chemical model, for a total of 19 time-steps starting from 10^3 yr after the formation of the clump to 10^5 yr.

Even if the time steps were reduced, the number of times that we needed to run the radiative transfer code for each time step, each model and each molecule was very high ($\sim$ 5000) hence we used a very powerful computer available at UCL, the Parameter Search Engine (PSE). PSE is a cluster of three Sun Microsystems SunFire V880 Servers, each SunFire V880 contains 8 UltraSparc III (750MHz) processors, 32 GB of memory and 0.8 GB of disk storage.

4.4 The best fit methods

Different methods can be used to compare the models with the observations. In particular three different χ^2 fits are defined:

1. **Line–shape fit**: the profile of the observed line is compared with the modelled line at similar spectral resolution. The χ^2 is computed summing the square deviations of the flux in each spectral bin whose size is equal to the spectral resolution of the observed line. The formula used is

$$\chi^2 = \sum_{i=1}^{N} \frac{[flux_{mod}(i) - flux_{obs}(i)]^2}{N} \tag{4.1}$$

   where i is the index of the spectral bin, N is the total number of the bins, $flux_{mod}(i)$ and $flux_{obs}(i)$ are the flux in the i^{th} bin for the modelled and observed lines, respectively.

2. **Integrated flux fit**: the total integrated flux of each line is compared with the integrated flux predicted by the model. The χ^2 is calculated summing the square deviation of the total line flux for different lines and it is normalized to the observed flux. The formula used is

$$\chi^2 = \frac{1}{N} \sum_{i=1}^{N} \left[\frac{Flux_{mod}(i) - Flux_{obs}(i)}{Flux_{obs}(i)} \right]^2 \tag{4.2}$$

where i is the index indicating the line, N is the total number of lines considered, $Flux_{mod}$ and $Flux_{obs}$ are the integrated line flux of the modelled and observed line, respectively.

3. **Blended lines fit**: for lines that are closely blended it is impossible to evaluate the contribution of the single lines to the total flux without arbitrary assumptions such as fixing the FWHM. In order to avoid to wrongly evaluate the contribution of the single lines, it is better to define a fit procedure that compares the total integrated flux of blended lines with the sum of the lines fluxes predicted by the model. The χ^2 is calculated summing the square deviation of the total flux of the blended lines and it is normalized to the observed flux. The formula used is

$$\chi^2 = \frac{1}{N}\sum_{i=1}^{N}\left[\frac{BlendFlux_{mod}(i) - BlendFlux_{obs}(i)}{BlendFlux_{obs}(i)}\right]^2 \qquad (4.3)$$

where i is the index indicating the group of blended lines, N is the total number of lines considered, $BlendFlux_{obs}$ is the total flux of the observed blended lines and $BlendFlux_{mod}$ is the sum of the model flux of the lines that are blended.

The first method can be used for any single line to derive the line profile that best reproduces the observed profile. The second method can be used to derive the model that best reproduces the integrated flux of all the observed lines at the same time. The third method is similar to the second but the sum of the flux of the blended lines is used instead of the flux of the single line and it must be used when it is not possible to deblend the observed lines. The second method has been adopted also by Doty et al. (2004) for a similar work that uses a chemical and a radiative transfer code to model the envelope of the protostar IRAS 16293–2422. The method turns out to be a powerful tool to probe the physical and chemical structure of the protostellar envelope as well as the age of the protostar. The first method is particularly thorough because it fits not only the total flux but also the line shape which, in the case of the outflow, may be non–Gaussian.

Given the large amount of models involved, the procedure that calculates χ^2 and identifies the best fit model has been automated, and the related software was developed as part of this thesis.

4.5 Modelling the clump S1 along CB3

The CB3 outflow has been presented in the previous chapter (see Sect. 3.2.2). Four molecular clumps were identified along the main axis with very similar physical parameters. We choose to fit the clump S1 of the CB3 outflow located in the southern lobe at an offset (0″,-30″) from the millimetre driving source since it is the best defined clump. In Table 4.2 we list all the species and the lines observed at the S1 position for which the molecular data (Einstein coefficients and collisional rates) exist and the radiative transfer code has been run. The integrated line flux and the FWHM of the lines are also given in Table 4.2. Since most of these lines have a Gaussian profile with similar width of about 10 km s^{-1}, we adopt a microturbulent velocity of 5 km s^{-1} in the radiative transfer modelling. This is equivalent to modelling the observed line profiles with a single Gaussian line with a fixed FWHM of 10 km s^{-1}. We assume a clump size of 0.12 pc as derived from the IRAM maps.

To model in detail the S1 clump the chemical models described in Chapter 3 were used but new models were computed also. In particular

- in Grid A a model with a density of 5×10^5 cm^{-3} was computed;
- a new grid, called Grid As, was introduced to represent a clump at uniform density that undergoes for a period a non–dissociative shock;
- in Grid B new models were computed for clumps with different temperatures and densities, i.e. clumps with a density profile ranging from 5×10^5 cm^{-3} to 10^6 cm^{-3} at a temperature of $T = 210$ K, clumps with a density profile from 2.5×10^5 cm^{-3} to 5×10^5 cm^{-3} and from 3×10^5 cm^{-3} to 6×10^5 cm^{-3}, with $T = 210$ K. Moreover, we added models with a different initial carbon abundance;
- in Grid C a model similar to C2 but with a higher temperature of T=210 K was computed.

Since most of the models from Grid D, where the clumps are formed by the compression of the incoming outflow, give unphysical results, here we restrict the analysis to models D1, D3, D4, D4–shock and D8 only.

Table 4.2: List of the molecules and transitions observed in the S1 clump of the CB3 outflow that are modelled with the radiative transfer code with the integrated line flux and the FWHM.

specie	line	ν (GHz)	$\int T_{mb} dv$ (K km s^{-1})	FWHM (km s^{-1})
CO	(2–1)	230.538	179.59	10.22
CS	(3–2)	146.967	16.94	8.61
SO	(6_5–5_4)	219.949	14.25	8.05
SO	(4_3–3_2)	138.178	14.76	9.25
SO_2	(3_{13}–2_{02})	104.029	1.21	10.00†
H_2CO	(3_{21}–2_{20})	218.760	5.29	10.33
CH_3OH	(5_0–4_0) A^+	241.791	16.94	11.51
CH_3OH	(5_{-1}–$_{-1}$) E	241.767	13.47	10.00†
CH_3OH	(5_0–4_0) E	241.700	5.03	8.29
CH_3OH	(3_0–2_0) A^+	145.103	20.47	10.00†
CH_3OH	(3_{-1}–2_{-1}) E	145.097	7.46	10.00†
CH_3OH	(3_0–2_0) E	145.094	16.94	11.51
CH_3OH	(2_0–1_0) A^+	96.741	1.12	10.00†
CH_3OH	(2_{-1}–1_{-1}) E	96.739	4.29	10.00†

† in the line Gaussian fit the FWMH of the line is fixed to 10 km s^{-1}

In Table 4.3 we list all the chemical models computed and their parameters: the name of the model (column 1), for the models already presented in Chapter 3 the name is the same; the presence (Y) or absence (N) of non–dissociative shock (column 2); the H_2 density of the clump (column 3), for models with a density profile we give the two extremes of the range; the final temperature (column 4); the percentage of gas depleted into grains at the end of the phase I (column 5); the initial sulphur abundance (column 6); the initial carbon abundance (column 7) and any other relevant parameters that were varied (column 8) such as the type of collapse simulated in phase I, if retarded instead of free–fall, the duration of the shocked phase if it is shorter, the percentage of CO converted into CH_3OH on the grain surfaces, the fact that all H_2CO is converted in CH_3OH on ices, the type of evaporation from the grains once the outflow approaches the clumps if time–dependent (TD) as in Viti & Williams (1999a) instead of instantaneous. For the models of Grid D we also give the velocity of the outflow.

All in all 39 chemical models were considered. For each model 19 time steps were selected and 6 molecular species were modelled so that the radiative transfer code was run 4446 times.

To fit the lines listed in Table 4.2 we used the χ^2 method that simultaneously fits the total integrated flux of the observed transitions of various species, see Eq. 4.2. In this formula the difference between the theoretical and observed flux is weighted with the observed flux instead of the error of the measurement because the uncertainties associated with the chemical models are higher than the errors of the observations, making it meaningless to use the error as the weight. Moreover, in this way we avoid giving the brighter lines a higher weight.

Table 4.3: List of the models and their parameters: presence (Y) or absence (N) of non–dissociative shock, final H_2 density, final temperature, percentage of freeze–out, initial sulphur abundance, initial carbon abundance and other possible parameters that are different with respect to the other models, i.e. if the collapse is retarded (B = 0.1) instead of free–fall (B = 1), if the shock phase is shorter (100 yr) that in the other models, if all the H_2CO is converted in CH_3OH on ices, the percentage of CO converted into CH_3OH on ices, and if the evaporation is time dependent (TD) instead of instantaneous. For Grid D models the density and temperature are the final ones (at $t = 10^5$ yr) and the velocity of the outflow is given.

model	shock	n(H_2) 10^5 (cm^{-3})	T (K)	FR (%)	X(S) (10^{-7})	X(C) (10^{-4})	Note
A1	N	1	210	15	130	1.0	
A2	N	1	210	35	130	1.0	retarded collapse, B=0.1
A3	N	1	210	11	130	1.0	retarded collapse, B=0.1
A4	N	1	210	20	19	1.0	
A5	N	10	210	20	130	1.0	
A6	N	10	210	30	1.3	1.0	
A7	N	10	210	55	1.3	1.0	
A8	N	10	210	80	1.3	1.0	
A9	N	50	210	25	130	1.0	
A10	N	5	210	30	130	1.0	
As1	Y	5	210	30	1.3	1.0	
As2	Y	1	210	30	1.3	1.0	
As3	Y	5	210	32	1.3	0.45	
As4	Y	5	210	30	1.3	1.0	short shock phase
B1	Y	5–10	110	40	1.3	1.0	
B2	Y	5–10	110	60	1.3	1.0	
B3	Y	5–10	110	60	1.3	1.0	$H_2CO \Rightarrow CH_3OH$
B4	Y	5–10	110	80	1.3	1.0	$H_2CO \Rightarrow CH_3OH$
B5	Y	5–10	110	60	1.3	1.0	$10\%CO \Rightarrow CH_3OH$
B6	Y	5–10	110	60	1.3	1.0	$20\%CO \Rightarrow CH_3OH$

Table 4.3: (continued)

model	shock	n(H_2) 10^5 (cm^{-3})	T (K)	FR (%)	X(S) (10^{-7})	X(C) (10^{-4})	Note
B7	Y	5–10	210	60	1.3	1.0	
B8	Y	2.5–5	210	40	1.3	1.0	
B9	Y	3–6	210	60	1.3	1.0	
B10	Y	5–10	210	20	1.3	1.0	
B11	Y	3–6	210	40	1.3	1.0	
B12	Y	2.5–5	210	60	1.3	1.0	
B13	Y	5–10	210	30	1.3	0.45	
B14	Y	5–10	210	35	1.3	0.45	
B15	Y	5–10	210	40	1.3	0.45	
B16	Y	5–10	210	15	1.3	0.45	
C1	N	5–10	110	40	1.3	1.0	
C2	N	5–10	110	60	1.3	1.0	
C3	N	5–10	110	60	1.3	1.0	$H_2CO \Rightarrow CH_3OH$; TD evap.
C4	N	5–10	210	60	1.3	1.0	
D1	N	5–10	110	20	1.3	1.0	$v_{outflow}$= 2 km s^{-1}
D3	N	5–10	110	20	1.3	1.0	$v_{outflow}$= 100 km s^{-1}
D4	N	2.5–5	100	20	1.3	1.0	$v_{outflow}$= 2 km s^{-1}
$D4_{shock}$	Y	5–10	100	20	1.3	1.0	$v_{outflow}$= 2 km s^{-1}
D8	N	5–10	100	20	1.3	1.0	$v_{outflow}$= 20 km s^{-1}

4.6 Single species fit

As first step we analyse each molecular species separately and in the next 6 subsections, we will present the results. In Sect. 4.7 we will attempt to fit all the species simultaneously.

In order to take into account the uncertainties in the parameters adopted in the models and the calibration errors of the observations, we assume that we obtain a good match to the models when the theoretical line flux differs by less than 10% from the observed flux.

Table 4.4: List of the best models for the two SO transitions, ordered by increasing χ^2, with the relative epoch, gas density, temperature, freeze–out and SO column density.

model	epoch (yr)	n(H_2) 10^5 (cm^{-3})	T (K)	FR (%)	N(SO) (cm^{-2})
B10	1×10^3	5–10	210	20	3.8×10^{14}
A10	5×10^3	5	210	30	6.4×10^{14}
B11	2×10^3	3–6	210	40	5.5×10^{14}
B9	3×10^4	3–6	210	60	5.3×10^{14}
B10	9×10^4	5–10	210	20	3.8×10^{14}
B7	8×10^4	5–10	210	60	3.6×10^{14}

4.6.1 SO

As already noted in the previous chapter, if in the chemical model we assume a standard solar initial abundance of sulphur (1.3×10^{-5}) the final abundance of SO is much higher than the observed one. Moreover the radiative transfer model produces strong self–absorption in the lines, which is not present in the observed line profile. The observed SO lines can be better reproduced assuming a depleted sulphur initial abundance of 1.3×10^{-7} as also indicated by previous studies (Viti et al. 2003; Ruffle et al. 1999).

Two lines of SO were detected towards the S1 clump and, due to the different excitation temperature of these lines (24 and 11 K), their ratio should allow to constrain the temperature of the gas. Indeed, the models with a temperature of $T \sim 200$ K are the only models that can reproduce the observed line ratio. In Table 4.4 we list all the models where both the two SO line fluxes differ $\leq 10\%$ from the observed fluxes, ordered by increasing χ^2. The SO column density in all the models ranges from 3.6×10^{14} cm^{-2} to 6.4×10^{14} cm^{-2}. The models from Grid B are the best ones, while models without a non–dissociative shock and models with low density ($n(H_2) < 3\times10^5$ cm^{-3}) do not seem to fit the SO lines at all. In Table 4.4 we note that models with equal input parameters but two different percentages of freeze–out (B10 and B7 or B9 and B11) can both fit the observed lines but at different epochs. In

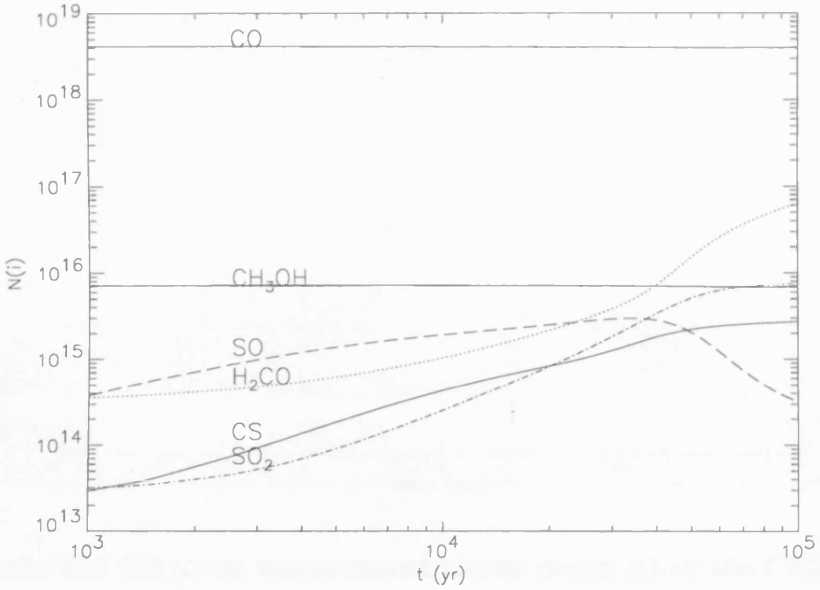

Figure 4.3: Column densities versus time for the B10 model.

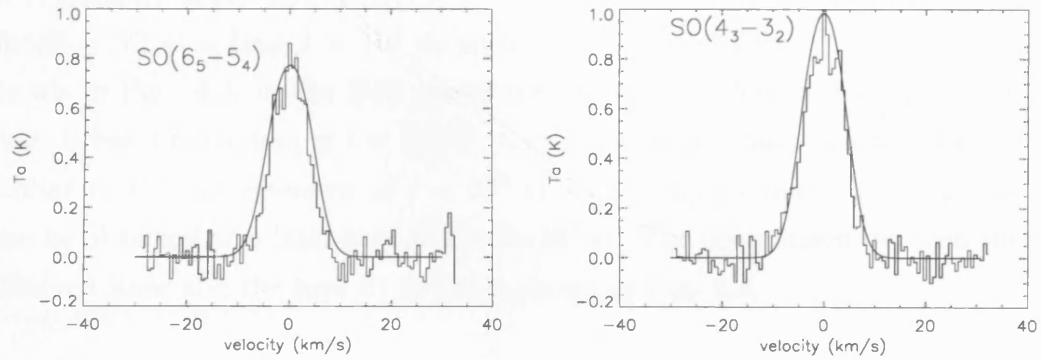

Figure 4.4: The two SO $(6_5–5_4)$ and $(4_3–3_2)$ lines observed in the clump S1 of the CB3 outflow (histogram) with the line profiles predicted by the best fit model B10 at $t = 10^3$ yr (continuous line).

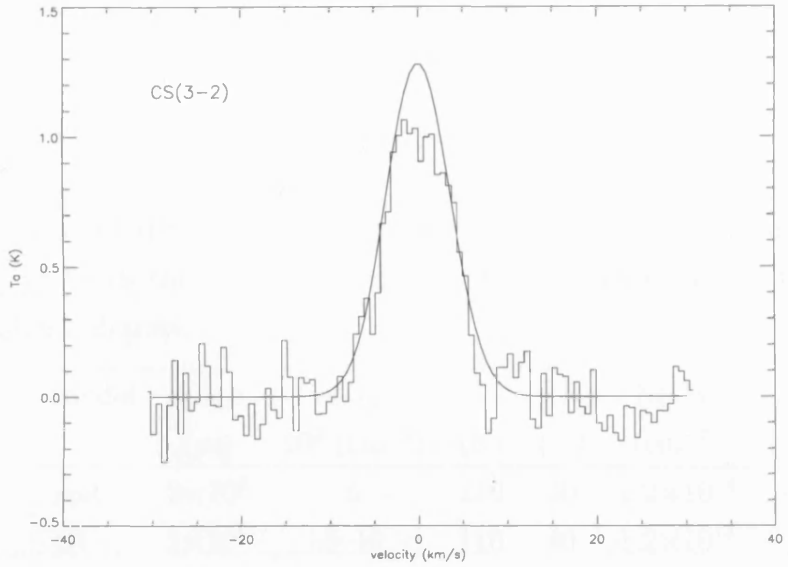

Figure 4.5: The CS (3–2) line observed in the clump S1 of the CB3 outflow (histogram) and the line profile predicted by the best fit model As1 at $t = 2{\times}10^3$ yr (continuous line).

particular, the models with the lower percentage of freeze–out fit the lines at an earlier epoch with respect to the models with higher freeze–out. The best fit is given by model B10 ($n(H_2) = (5\text{–}10){\times}10^5$ cm^{-3}, $T \sim 200$ K, FR = 20%, Shock = Y) at a time $t = 10^3$ yr with N(SO) $\sim 4{\times}10^{14}$cm^{-2}. However, as shown in Fig. 4.3, in the B10 model the SO column density increases with time, it has a maximum at $t = 3{\times}10^4$ yr and then it decreases again to a value similar to the one assumed at $t = 10^3$ yr. This implies that a good fit can also be obtained at a later time of $t = 9{\times}10^4$ yr. The comparison between the observed lines and the best fit model is shown in Fig. 4.4.

4.6.2 CS

Table 4.5 lists all the models that fit the CS (3–2) line. CS is a high density tracer and we find that at a fixed density it is also quite sensitive to the percentage of freeze–out, and in fact models with the same temperature and density but different freeze–out fit the line at different epochs. In 14 out of 39 models, at least a time can be found in which the flux of the CS (3–2) line

Table 4.5: List of the best models for the CS (3–2) transition, ordered by increasing χ^2, with the relative epoch, gas density, temperature, freeze–out and CS column density.

model	epoch (yr)	n(H_2) 10^5 (cm^{-3})	T (K)	FR (%)	N(CS) (cm^{-2})
As1	2×10^3	5	210	30	1.2×10^{14}
C1	1×10^5	5–10	110	40	1.2×10^{14}
A4	1×10^3	1	170	20	1.5×10^{14}
A2	3×10^3	1	210	35	1.3×10^{14}
B12	4×10^4	2.5–5	210	60	1.4×10^{14}
B10	5×10^3	5–10	210	20	1.6×10^{14}
D4	2×10^3	10	70	20	2.2×10^{14}
As1	1×10^3	5	210	30	1.1×10^{14}
C3	6×10^3	5–10	110	60	1.1×10^{14}
D8	2×10^3	10	70	20	1.6×10^{14}
B9	4×10^4	3–6	210	60	1.6×10^{14}
C3	5×10^3	5–10	110	60	1.2×10^{14}
B4	3×10^3	5–10	110	80	1.0×10^{14}
C2	4×10^4	5–10	110	60	1.0×10^{14}
B9	3×10^4	3–6	210	60	1.3×10^{14}
As1	3×10^3	5	210	30	1.3×10^{14}
C3	3×10^4	5–10	110	60	1.7×10^{14}
B8	1×10^4	2.5–5	210	40	1.0×10^{14}
As2	1×10^5	1	210	30	1.2×10^{14}

differs less than 10% from the observed flux and for 3 models, namely As1, C3 and B9, we find a range of times fitting the line (see Table 4.5). The models cover almost all the explored parameter space indicating that the CS (3–2) line alone can not be used to constrain the physical conditions of the clump, nor can it be used to discriminate among different scenarios of formation. Despite the different physical parameters, all the models in Table 4.5 have a similar CS column density: N(CS) $\sim 10^{14}$ cm^{-2}. The best fit model is model As1 ($n(H_2)$ = 5×10^5 cm^{-3}, $T \sim 200$ K, FR = 30%, Shock = Y) at a time t = 2×10^3 yr with N(CS) = 1.2×10^{14} cm^{-2}. The comparison between the observed line and the best fit model is shown in Fig. 4.5. One can see that the modelled line has a stronger peak than the observed line. This is likely due to the fact that the observed line has a FWHM slightly lower than the fixed value of 10 km s^{-1} assumed in the model; indeed the Gaussian fit of the line gives a FWHM = 8.61 km s^{-1} (see Table 4.2). Another possibility is that the line is weakly self–absorbed.

4.6.3 SO_2

Table 4.6 lists all the models where the SO_2 line flux differs $\leq$ 10% from the observed flux, ordered, as usual, by increasing χ^2. The SO_2 column density ranges from 2×10^{14} to 5×10^{14} cm^{-2}. We find that N(SO_2) is very sensitive to time and in all the models it increases by more than two orders of magnitude from $t = 10^3$ yr to $t = 10^5$ yr. However, we do not seem to find a good fit for times $> 10^4$ yr. At later times the modelled column density is usually higher than the observed one. Similar to the SO fits, the models from Grid B, As, and A with high H_2 density ($n(H_2) \geq 10^6$ cm^{-3}) give the best fits, indicating once again that the scenario where the clump is (at least partially) pre–existing the outflow is the most likely. All models from Grid D, C and A (with the exception of A8 and A9 – see below) produce a SO_2 line intensity very different from the observed one, by up to two orders of magnitude for model D4. One common characteristic of these models is the lack of a post–shock phase at high temperature, hence it seems that this species is indeed a good tracer of the presence of a non–dissociative shock. This is in agreement with theoretical models of C–type shocks (Pineau des Forêts et al., 1993) where the

Table 4.6: List of the best models for the SO_2 (3_{13}–2_{02}) transition, ordered by increasing χ^2, with the relative epoch, gas density, temperature, freeze–out and SO_2 column density.

model	epoch (yr)	n(H_2) 10^5 (cm^{-3})	T (K)	FR (%)	N(SO_2) (cm^{-2})
A9	6×10^3	50	210	25	2.5×10^{14}
B1	3×10^3	5–10	110	40	3.5×10^{14}
A8	2×10^3	10	210	80	2.6×10^{14}
B8	5×10^3	2.5–5	210	40	2.7×10^{14}
A8	3×10^3	10	210	80	2.7×10^{14}
B7	6×10^3	5–10	210	60	5.1×10^{14}
As1	9×10^3	5	210	30	2.1×10^{14}
B9	6×10^3	3–6	210	60	3.3×10^{14}
B3	1×10^3	5–10	110	60	3.8×10^{14}
A8	4×10^3	10	210	80	2.8×10^{14}
B11	7×10^3	3–6	210	40	3.5×10^{14}

abundance of SO_2 is seen to increase after the passage of the shock and SO_2 is the dominant form of sulphur in the post–shock region.

The best fit model is the model A9 ($n(H_2) = 5\times10^6$ cm^{-3}, $T \sim 200$ K, FR = 25%, Shock = N) at the epoch of $t = 6\times10^3$ yr. The comparison between the observed line and the best fit model is shown in Fig. 4.6. However, we think that it is unlikely that this model is correct because such high uniform density for a clump of 0.12 pc would imply a visual extinction of more than 1000 mags. Moreover, the initial sulphur abundance for A9 is solar. Probably, in the A9 model the absence of the non–dissociative shock is compensated by the higher initial sulphur abundance and the high density that lead to a SO_2 column density able to fit the line. As can be seen from Table 4.6 there are quite a number of models that can fit the SO_2 line. It is clear therefore that we can not use this line to deduce uniquely the physical characteristics of our clump. However, the SO_2 line does seem to trace a gas with a density between 3×10^5 and 10^6 cm^{-3} and a temperature between 100 and 200 K. The

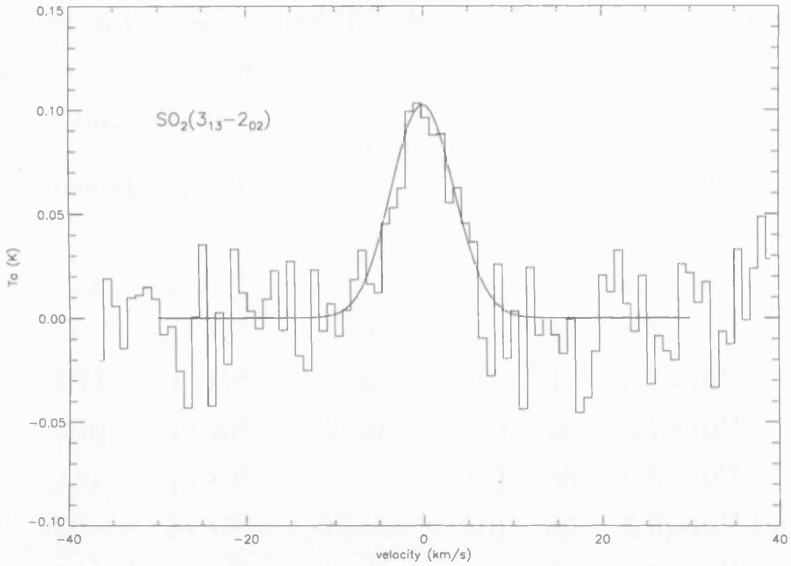

Figure 4.6: The SO_2 (3_{13}–2_{02}) line observed in the clump S1 of the CB3 outflow (histogram) with the line profiles predicted by the best fit model A9 at $t = 6{\times}10^3$ yr (continuous line).

freeze–out parameter is not constrained at all since in the models that fit the data the freeze–out parameter ranges from 25% to 80%. This is not surprising since SO_2 is a second generation species which forms after the dissociation of other sulphur–bearing species released from the grains (see Sect. 1.5.6).

4.6.4 H_2CO

Table 4.7 reports all the models that fit the observed flux of the H_2CO (3_{21}–2_{20}) line within 10%. Good fits can be obtained in models with non–dissociative shocks (Grid B and As). In the models without them (Grid A, C and D) the formaldehyde is usually overabundant. This is because this species is mainly formed by the reaction of oxygen with CH_3. In models with a non–dissociative shock, during the high temperature phase, the oxygen mainly interacts with neutrals to form OH and H_2O, thus there is less oxygen free to form H_2CO. H_2CO is one of the species most sensitive to time; indeed its abundance increases by more than one order of magnitude from $t = 10^3$ yr to $t = 10^5$ yr. A good fit can only be found for the very early epochs of $\leq 4 \times 10^3$ yr; if the

Table 4.7: List of the best models for the H_2CO (3_{21}–2_{20}) transition, ordered by increasing χ^2, with the relative epoch, gas density, temperature, freeze–out and H_2CO column density.

model	epoch (yr)	n(H_2) (10^5 cm^{-3})	T (K)	FR (%)	N(H_2CO) (cm^{-2})
As1	1×10^3	5	210	30	6.1×10^{14}
B3	1×10^3	5–10	110	60	6.5×10^{14}
B11	4×10^3	3–6	210	40	6.5×10^{14}
B10	4×10^3	5–10	210	20	5.1×10^{14}
As1	2×10^3	5	210	30	6.6×10^{14}
B8	3×10^3	2.5–5	210	40	6.0×10^{14}
B10	3×10^3	5–10	210	20	4.5×10^{14}

clumps evolve for more that 5×10^3 yr after the high temperature phase, the theoretical abundance of H_2CO is always overabundant with respect to the observations. Even in models where we allow conversion of H_2CO to methanol on the grains (B3 and B4) an acceptable fit can only be obtained at $t = 10^3$ yr for the B3 model (see Table 4.7). A lower H_2CO abundance can be obtained in models with a lower carbon initial abundance (these models will be presented in Sect. 4.6.6). Indeed a theoretical line flux that differs less than 10% from the observed flux is found in all the models from B13 to B16 still at early epochs $\leq 10^4$ yr (not shown in the Table 4.7).

The H_2CO column density in the selected models ranges from 4.5×10^{14} to 6.5×10^{14} cm^{-2} and the freeze–out parameter ranges between 20% and 60% while the temperature is $\sim$ 200 K, with the exception of the B3 model. The best fit model is As1 ($n(H_2) = 5\times10^5$ cm^{-3}, $T \sim 200$ K, FR = 30%, Shock = Y) at the time $t = 10^3$ yr and column density N(H_2CO) = 6.1×10^{14} cm^{-2}. In Fig. 4.7 the As1 model is plotted superimposed to the observed line spectrum.

4.6.5 CH_3OH

Methanol has always been considered a good tracer of the physical conditions of the emitting gas in star forming regions (e.g. Kalenskii et al. 1997; Leurini

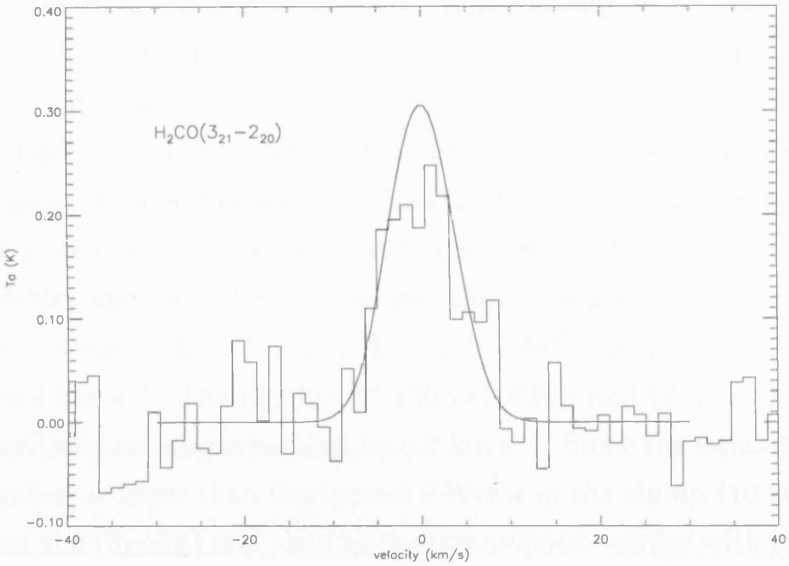

Figure 4.7: The H_2CO (3_{21}–2_{20}) line observed in the clump S1 of the CB3 outflow (histogram) with the line profiles predicted by the best fit model As1 at $t = 1{\times}10^3$ yr (continuous line).

et al. 2004). In particular, it has been used as a probe of density in high–density media (e.g. Menten et al. 1988) and a temperature estimate can be easily derived from the rotational diagram, if multiple transitions are available. Moreover, the presence of several transitions close in wavelength make it easy to observe more lines simultaneously, increasing the number of observational constraints and minimizing the relative calibration uncertainties.

The Boltzmann plot of the 8 methanol lines observed in the S1 clump gives a column density $N(CH_3OH) \sim 10^{16}$ cm^{-2} and a rotational temperature of only 16 K (Codella & Bachiller, 1999b), well below the 200 K we derived from the other molecules. However, in the physical conditions typical of outflows the gas is not in LTE condition and it is subthermally excited so that the rotational temperature estimated from the Boltzmann plot is below the kinetic temperature (Bachiller et al., 1995).

In the radiative transfer model the A and E types of methanol must be considered as separate species since the transition between the two symmetry states can not happen at a significant rate by radiative or collisional processes.

We assume the standard ratio of 1 between A and E methanol, as also suggested by the absence of a significant shift in the A and E transitions in the Boltzmann plot. This choice has also been verified a posteriori since we find that both A and E methanol lines have similar deviation with respect to the observed lines.

From Table 4.2 one can see that the (3_K–2_K) and (2_K–1_K) transitions are very close in frequency. The line rest frequencies of the CH_3OH (3_0–2_0) A^+ (145.103 GHz) and (3_{-1}–2_{-1}) E (145.097 GHz) transitions are separated by 12.4 km s^{-1}, those of the (3_{-1}–2_{-1}) E (145.097 GHz) and (3_0–2_0) E (145.094 GHz) by 6.2 km s^{-1}. The (2_0–1_0) A^+ (96.741 GHz) and (2_{-1}–1_{-1}) E (96.739 GHz) transitions are also separated by 6.2 km s^{-1}. Since the separation of the lines is similar or lower than the typical FWHM in the clump (10 km s^{-1}) we expect that the (3_K–2_K) and the (2_K–1_K) transitions overlap with each other. Indeed the lines at 145.1 and 96.7 GHz are blended; thus photons at these frequencies will see a higher optical depth than expected, because they are "seeing" the line profiles of neighboring transitions. The SMMOL code does not yet have a line–overlap facility, so our modelling of these blended methanol transitions is semi–quantitative. For this reason we consider as an acceptable fit for the methanol all the models that produce line fluxes that differ by less than 30% with respect to the observed flux, instead of 10% as used for the other species.

None of our models are able simultaneously to fit all of the 8 methanol transitions (5 lines of CH_3OH–E and 3 lines of CH_3OH–A). In particular, we find that in models where the higher energy transitions (5_K–4_K) are reproduced, the lower energy transitions (3_K–2_K and 2_K–1_K) are largely underestimated. Conversely, models that reproduce the lower energy transitions overestimate the transitions at higher energy. This could be a direct consequence of the effects of line–overlap in the (3_K–2_K and 2_K–1_K) transitions: the low energy transitions are simply "seeing" more optical depth than the higher energy transitions.

We did test, however, whether these inconsistencies are due to the incorrectness of our basic assumptions on the physical conditions in the clump; we computed further models where we assumed: *i)* a lower temperature of T = 20 K or *ii)* a smaller size of the clump of 0.06 pc. Again, there is no single

model able to fit both the lower and the higher energy transitions at the same time. Another possible explanation is that the high energy transitions trace a different component of the gas, possibly with different physical (and chemical) characteristics. Indeed the (5_K–4_K) lines seem to be fitted with models that produce a methanol column density of $\sim 5\times10^{14}$ cm^{-2} while the (3_K–2_K) and (2_K–1_K) lines are fitted by models that have a higher column density, N(CH_3OH) $\sim 5\times10^{15}$ cm^{-2}. Hence, we tried to separately fit the two components. For the high energy transitions (the 5_K–4_K lines) we find that most of the models that fit the lines belong to Grid D (see Table 4.8), indicating that these transitions may trace a gas compressed by the outflow (scenario D). Note that the models in Grid D have a lower abundance of methanol than the models in the other grids. This is due to a reduced amount of frozen material, since methanol is preferentially formed on the grains via hydrogenation of a fraction of CO and H_2CO: in the scenario depicted in Grid D the clump is formed by the compression of the outflow, and therefore the timescale available for freeze out is quite short. Moreover during the clump formation the temperature also increases, significantly slowing the freeze out. While it is possible that the high J transitions trace a newly formed clump (scenario of Grid D), it is also possible that this lower column density component simply traces a smaller component of the clump. To test this hypothesis we recomputed models A10 and As1 assuming a smaller clump size of 0.04, 0.05 and 0.06 pc instead of 0.12 pc. We found that both models A10 and As1 were able to fit the 3 CH_3OH lines of the (5_K–4_K) transition within 30% with a clump size of 0.05 pc (see Table 4.8).

As discussed above the three (3_K–2_K) lines and the two (2_K–1_K) lines are closely blended. Therefore to attempt a fit to the 5 CH_3OH lines of the (3_K–2_K) and (2_K–1_K) transitions, we decided to calculate the χ^2 considering the sum of the flux of all the blended lines rather than each line flux separately. i.e. using Eq. 4.3 rather than Eq. 4.2. We find that two of our models fit the 5 lines (see Table 4.9). The best fit model is B10 ($n(H_2)$ = (5–10)$\times10^5$ cm^{-3}, $T \sim$ 200 K, FR = 20%, Shock = Y) with a column density N(CH_3OH) = 7×10^{15} cm^{-2}. The best fit time is $t = 6\times10^4$ yr, although in B10 the methanol column density is quite constant in time so it is not possible to constrain the age of

Table 4.8: List of the best models for the 3 lines of the CH_3OH (5_K–4_K) transitions (both A and E type), ordered by increasing χ^2, with the relative epoch, gas density, temperature, freeze–out and methanol column density. The last 2 models have a smaller clump size of 0.05 pc

model	epoch (yr)	$n(H_2)$ 10^5 (cm^{-3})	T (K)	FR (%)	$N(CH_3OH)$ (cm^{-2})
D1	(9–10)×10^4	5–10	110	20	(4.2–4.8)×10^{14}
B12	(8–9)×10^3	2.5–5	210	60	(4.3–4.7)×10^{14}
D8	1×10^5	5–10	100	20	5.2×10^{14}
D4	7×10^4	3–5	100	20	4.3×10^{14}
A10	(1–10)×10^4	5	210	30	(1.2–1.5)×10^{15}
As1	(1–4)×10^3	5	210	30	1.5×10^{15}

Table 4.9: List of the best models for the 5 lines of the CH_3OH (3_K–2_K and 2_K–1_K) transitions (both A and E type), ordered by increasing χ^2, with the relative epoch, gas density, temperature, freeze–out and methanol column density.

model	epoch (yr)	$n(H_2)$ 10^5 (cm^{-3})	T (K)	FR (%)	$N(CH_3OH)$ (cm^{-2})
B10	6×10^4	5–10	210	20	7×10^{15}
C3	7×10^4	5–10	110	60	3×10^{15}

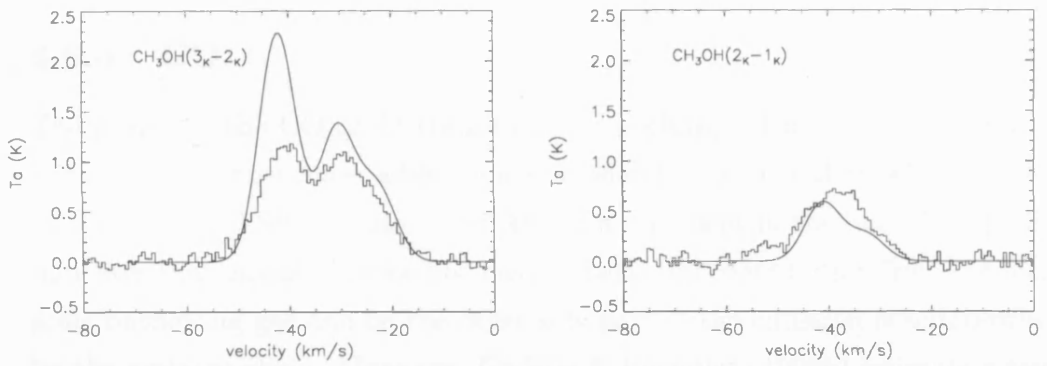

Figure 4.8: The CH_3OH (3_K–2_K) and (2_K–1_K) lines observed in the clump S1 of the CB3 outflow (histogram) and the line profile predicted by the best fit model B10 at t =6×10^4 yr (continuous line).

this component. In Fig. 4.8 we show the best fit model: although the total flux of the three blended (3_K–2_K) lines are still within the 30% of tolerance, we do not achieve a good fit for the CH_3OH (3_0–2_0) A^+ line at -41.5 km s^{-1}. We note that in all the models the ratio between the (3_0–2_0) A^+ and the (3_0–2_0) E lines is always higher (up to a factor of 1.5) than the observed value, indicating a systematic trend to overestimate the (3_0–2_0) A^+ irrespective of the model parameters. This is very likely due to the effect of line overlap that is not included in our radiative transfer model.

Despite the limitation due to the lack of the line–overlap effect in the modelling, our analysis seems to indicate the presence of two different methanol components: one with a lower column density of N(CH_3OH) $\sim$ 5×10^{14} – 10^{15} cm^{-2}, and possibly with smaller size, traced by the higher energy transitions, and another with a higher column density of N(CH_3OH) $\sim$ 7× 10^{15} cm^{-2} and probably at lower excitation conditions since it is traced by the lower energy lines. In our analysis we assume the same temperature for both components; this may be unrealistic but probably neither of the two components has a temperature less than 100 K, due to the presence of the outflow. The possibility of different components or substructures within the clump was already put

forward in the analysis presented in Chapter 3.

4.6.6 CO

The profile of the CO (2–1) transition in the clump S1 is very different with respect to the other lines: a blue non–Gaussian line wing and an selfabsorption at the ambient LSR velocity (-38.5 km^{-1}) are present in the line. This profile indicates that on one side the line has a substantial contribution from the large scale outflowing gas and on the other side part of the emission is selfabsorbed by the ambient cloud. Moreover, Codella & Bachiller (1999b) estimate a temperature of $\sim$ 20 K for the CO at all the line velocities and they find that the (2–1) line is optically thick, showing that the emission is dominated by the outer, colder part of the outflow rather than by the S1 clump. All of this makes it very difficult to evaluate the actual contribution of the molecular clump to the overall observed emission. For this reason we prefer not to consider the CO for the global fitting. However, it was decided to run the radiative transfer model also for this molecule in order to roughly evaluate whether the results for this species are in agreement with the others. For the fitting, we consider only the flux coming from the Gaussian core of the CO (2–1) line, neglecting the non–Gaussian line wings ascribable to the outflow.

In general we found that in all the models at higher density, i.e. $n(H_2) \geq 5{\times}10^5$ cm^{-3}, the CO line is more intense, by a factor 4–6, than the observed line. This disagreement could not be simply attributed to the lower temperature of the gas since the expected flux of the CO (2–1) line emitted by a gas at $T = 10$ K is more than one order of magnitude lower than the flux emitted by the same gas but at a higher temperature $T = 200$ K. Moreover, the theoretical CO (2–1) line flux for a gas with $n(H_2) \geq 5{\times}10^5$ cm^{-3} and $T = 20$ K is about a factor of 4 lower than the observed line.

In high mass star forming regions the C/O ratio is found to be lower than the standard value of 0.467. Hence we investigated the possibility of a reduced CO abundance by assuming a lower initial abundance of carbon. Models in Grid As and B with an initial carbon abundance of $4.5{\times}10^{-5}$ derived from the C/O ratio of 0.21 found in the Orion Bar (Walmsley et al., 1999) were computed. Again these models produce a CO (2–1) which is too strong with

Table 4.10: List of the best models for the CO (2–1) transition, ordered by increasing χ^2, with the relative epoch, gas density, temperature, freeze–out and CO column density.

model	epoch (yr)	n(H_2) 10^5 (cm^{-3})	T (K)	FR (%)	N(CO) (cm^{-2})
B11	9×10^4	3–6	210	40	5.5×10^{17}
B8	1×10^5	2.5–5	210	40	4.0×10^{17}
A2	1×10^5	1	210	35	4.9×10^{17}
A9	3×10^3	50	210	25	6.6×10^{17}
A1	4×10^4	1	210	15	4.5×10^{17}
A4	4×10^4	1	210	20	4.5×10^{17}

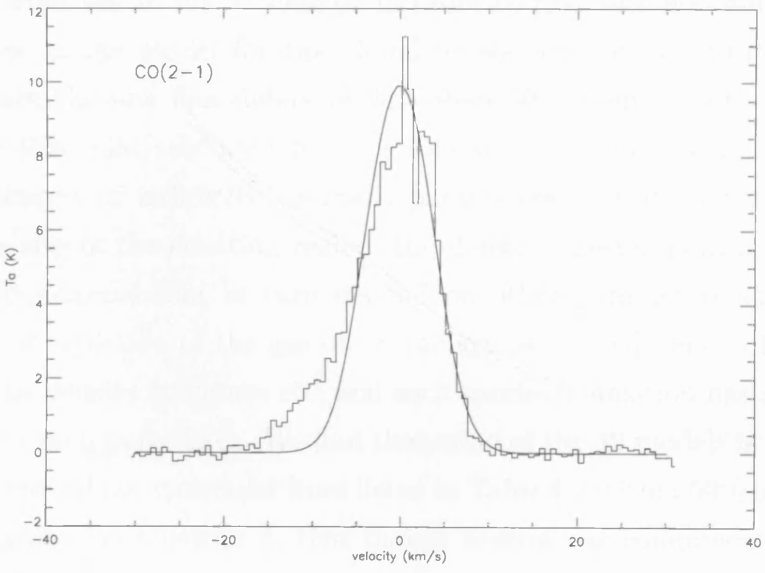

Figure 4.9: The CO (2–1) transition observed in the clump S1 of the CB3 outflow (histogram) with the line profile predicted by the best fit model B11 at $t = 9\times10^4$ yr (continuous line).

respect the observation.

The models that better reproduce the observed flux are listed in Table 4.10. These models all have a low density ($n(H_2) \leq 6\times10^5$ cm^{-3}) and a low freeze-out (FR $\leq$ 40). The only exception is model A9; however the best fit age for this model is only $t = 3\times10^3$ yr, the same model predicts a line brighter than observed by a factor 3.6 at the later epoch $t = 10^5$ yr. The CO column density from the best models is in the range of (4–7)$\times10^{17}$ cm^{-2}. The best fit model is model B11 at time t=9$\times10^4$ yr, with $n(H_2)$ = (3–6)$\times10^5$ cm^{-3}, $T \sim$ 200 K, N(CO) = 5.5$\times10^{17}$ cm^{-2} and freeze-out 40%. In Fig. 4.9 the best fit model is plotted superimposed on the observed line.

4.7 Multi species fit

In the previous section it was shown that, if one considers each species separately, it is indeed possible to find a very good fit for each species.

We now attempt to find a model that simultaneously fits all the molecular transitions observed in the S1 clump. In order to take into account the large uncertainties in the model for the global fit we consider acceptable all the models where the line flux differs by less than 50% from the observed flux. We choose this relatively high level of tolerance because the line emission depends, directly or indirectly, on many parameters that are not well known such as the size of the emitting region, the density, the temperature and the chemical abundances that in turn depend on other parameters such as the percentage of depletion of the gas on to the grains, the efficiency of chemical reactions, the density structure etc, and each species/transition has a different sensitivity to each parameter. We find that none of the 39 models is able to fit simultaneously all the molecular lines listed in Table 4.2 within 50% indicating, as also suggested in Chapter 3, that indeed several gas components exist in the IRAM–30m beam.

In order to identify the different components we consider different groups of molecules. Firstly, we consider all the sulphur–bearing molecules i.e. CS, SO, SO_2. None of the 39 models are able to fit all four observed lines. In particular, while several models fit both the CS and SO transitions (see Table

Table 4.11: List of the best models for the SO (6_5–5_4), SO (4_3–3_2) and CS (3–2) lines, ordered by increasing χ^2, with the relative epoch, gas density, temperature and freeze–out.

model	epoch (yr)	n(H_2) (10^5 cm^{-3})	T (K)	FR (%)
B9	3×10^4	3–6	210	60
As1	1×10^3	5	210	30
B4	2×10^3	5–10	110	80
B12	2×10^4	2.5–5	210	60
B12	3×10^4	2.5–5	210	60
As1	2×10^3	5	210	30
A1	2×10^3	1	210	15

4.11) the same models do not fit the SO_2 (3_{13}–2_{02}) line that is usually fitted at the earlier times of $t < 10^4$ yr (see Table 4.6). The best fit model for CS and SO is the model B9 at a time of $t = 3\times10^4$ yr. The line profiles of this model are shown in Fig. 4.10. However, at that time, the SO_2 line is eight times more intense than the observed emission as can be seen in Fig. 4.11 where the column density of the species is plotted versus time. In the same model the SO_2 line can however be fitted at an earlier time, $t = 6\times10^3$ yr, when the column density is N(SO_2) = 3×10^{14} cm^{-2}. Since in most of the models the SO_2 abundance increases significantly with time, the fact that the SO_2 (3_{13}–2_{02}) line is fitted at early epochs (see Table 4.6) indicates that a low quantity of SO_2 is needed to fit the line. A low column density of SO_2 can be obtained not just by having a low chemical SO_2 abundance but also by assuming a smaller size for the clump. In fact, a smaller component in the clump has been already suggested by the analysis of the methanol lines and also in Chapter 3. As was done for methanol, we test this possibility considering the chemical models A10 and As1 with a smaller clump size of 0.04, 0.05 and 0.06 pc. In the A10 models the SO_2 abundance is always lower than that in the As1 model due to the lack of a high temperature phase in the former model. The A10 model does not succeed in fitting the observed SO_2 (3_{13}–2_{02}) line. On the contrary, a

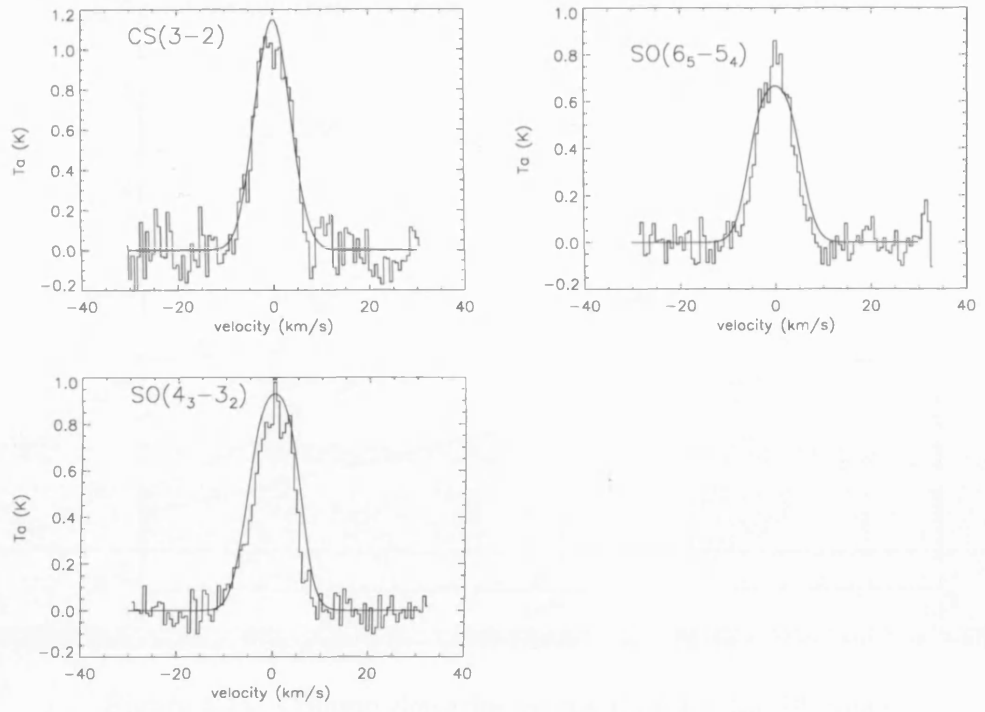

Figure 4.10: The CS and SO lines observed in the clump S1 of the CB3 outflow (histogram) with the line profile predicted by the best fit model B9 at $t = 3{\times}10^4$ yr (continuous line).

very good fit can be obtained if one assumes a size of 0.05 pc for the model As1 at the epoch $t = 4{\times}10^4$ yr. At this epoch, the model As1 also fits the 3 higher energy lines of methanol (see Fig. 4.12), as already shown in Sect. 4.6.5. The same model does not fit the CS and SO lines. We therefore conclude that SO_2 and the higher energy methanol (5_K–4_K) lines may be emitted from a smaller gas component with a size of ~ 0.05 pc, $n(H_2) \sim 5 \times 10^5$ cm^{-3} and $T \sim 200$ K. This component is associated with emission at high excitation of molecules produced in high temperature gas, thus it could trace the zone of stronger interaction between the outflow and the clump.

Next we attempt to fit simultaneously the CS and SO transitions together with the 5 lower energy transitions of CH_3OH (3_K–2_K) and (2_K–1_K). We find no models able to fit simultaneously the 3 species within 50% of the observed value. In fact, from the fitting of the single species (see Sect. 4.5) we see that

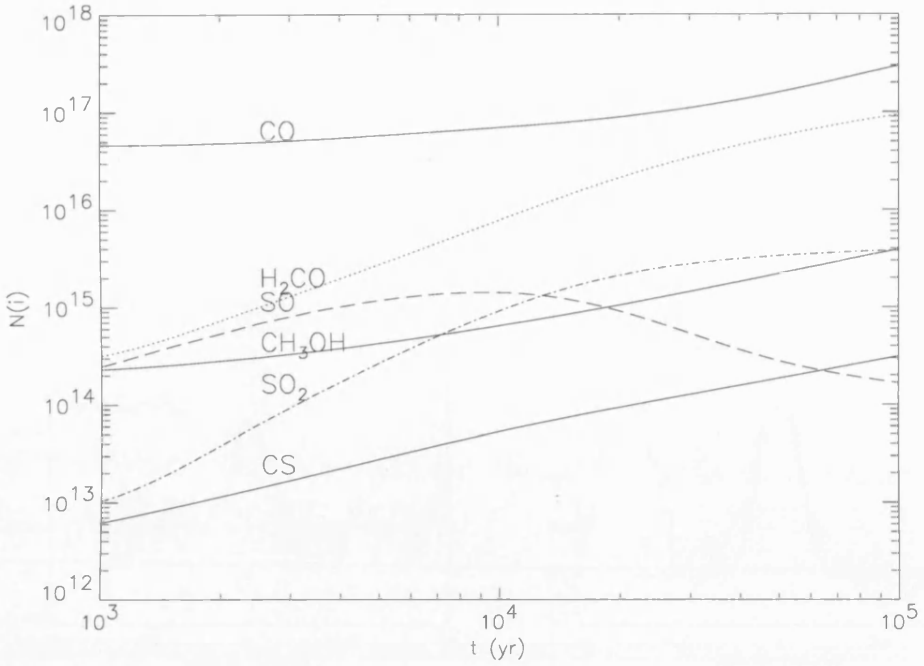

Figure 4.11: Column densities versus time for the B9 model.

the low energy methanol lines seem to trace a slightly higher density (model B10 with $n(H_2) = (5\text{–}10)\times10^5$ cm^{-3}) than the CS and SO component (model B9 with $n(H_2) = (3\text{–}6)\times10^5$ cm^{-3}), but at the same temperature ($T \sim 200$K) and at a very similar time (6×10^4 yr and 3×10^4 yr, respectively). However, the difference in the density is not so relevant, considering also the high uncertainties in the model especially for methanol because of the line overlap effects, and it is likely that the low energy transitions of CH_3OH are associated with the same extended gas component traced by CS and SO.

Finally, we check whether the H_2CO (3_{21}–2_{20}) line could be associated with one of the two identified components. We find that the B9 model with clump size of 0.12 pc at $t = 3\times10^4$ yr predicts a line about 25 times brighter than the observed one. Indeed, as said in Sect. 4.4, assuming a size of 0.12 pc the H_2CO can be fitted only at very early epochs ($t \leq 4\times10^3$ yr) while for more evolved times all the models predict far too much H_2CO. On the other hand, if we consider the smaller component, i.e. an As1 model at 4×10^4 yr with a clump size of 0.05 pc, the theoretical intensity is only 3 times higher than the observed one, while at the early epoch of 2 $\times10^4$ yr a very good fit (within

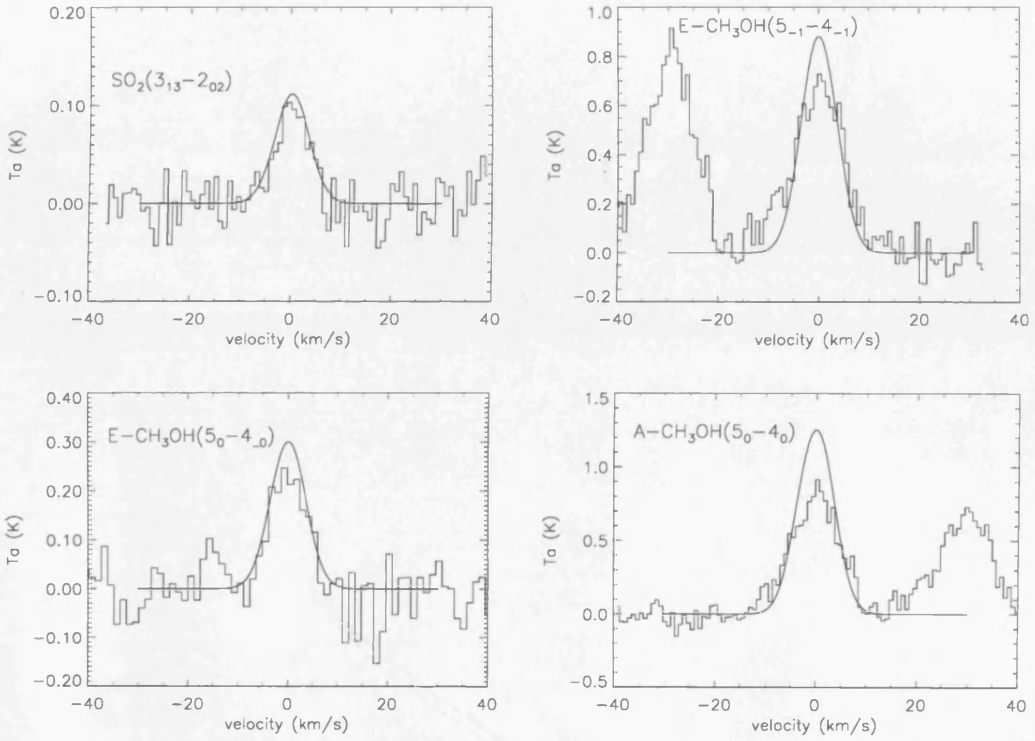

Figure 4.12: The SO_2 (3_{13}–2_{02}) and CH_3OH (5_K–4_K) lines observed in the clump S1 of the CB3 outflow (histogram) with the line profile predicted by the best fit model As1 at $t = 4{\times}10^4$ yr (continuous line). The size of the clump is $d = 0.05$ pc.

20%) to the observed line is obtained. Although a global fit of the H_2CO, SO_2 and high–J CH_3OH lines cannot be obtained within the tolerance of 50%, it is likely that H_2CO does not trace the whole clump but is associated with the smaller gas component and it is probably emitted by a region even smaller than 0.05 pc.

As already explained in Sect. 4.6.6, the CO (2–1) line is dominated by the outer, colder part of the outflow rather than by the S1 clump. Hence the CO (2–1) line is not included in the global fit to the S1 clump. However, it is worth evaluating if for the best fit model the contribution of the clump to this line is negligible as expected if the emission is dominated by the outflow rather than the clump. Indeed, in the B9 model, fitting CS and SO, the predicted CO (2–1) flux is only 23% of the observed flux.

We find that some species are very sensitive to time, such as sulphur–bearing molecules, in agreement with several previous studies (Hatchell et a. 1998, Viti et al. 2001, Wakelam et al. 2005, Codella et al. 2005), and they can therefore be used to determine the age of the S1 clump. We fit both the components of the clump with the same age $\sim (3\text{–}4)\times10^4$ yr which is similar to the dynamical age of the S1 clump estimated from the SiO emission ($t \sim 10^5$ yr, Codella & Bachiller 1999b). Note however that our starting point (t=0) in all scenarios is set to be when the outflow starts interacting with the surrounding environment, hence the age we derive is not necessarily the age of the outflow.

4.8 Conclusions

From the above analysis we can conclude that the coupling of a time–dependent chemical model with a radiative transfer code proved to be a powerful tool in constraining the physical and chemical parameters of the gas, especially when more than one transition of the same molecule is detected. In fact, we find that more than one model is able to fit the line emission of single species whilst a multi–line and multi–species analysis was able to constrain some of the physical parameters of the clump.

Different scenarios for the formation of the clump have been investigated within a large range of physical conditions. Our results show that most of the

observed lines can not be fitted by models from the scenarios A, C and D. On the contrary, the models from scenario B or As seem able to reproduce most of our data. This is consistent with the findings from Chapter 3 where a preliminary analysis was done using only the chemical model. The main conclusion of this work is that the observed dense clumps are, at least partially, formed prior to the advent of the outflow. The advent of the outflow on such clumps leads to a short phase of high temperature (T $\sim$ 1000 K) followed by fast cooling down to temperatures of $\sim$ 200 K.

In addition to the large–scale outflowing gas traced by the non–Gaussian wings detected in the CO (2–1) line, we identify two other components inside the large IRAM–30m beam (HPBW = 10 - 29 arcsec). The extended component (d = 0.12 pc) is traced by CS and SO and probably by the lower energy transitions (3_K–2_K) and (2_K–1_K) of CH_3OH. This component is not uniform in density but has a density structure in the range 3×10^5 - 10^6 cm^{-3}. The second component is more compact, with size $\sim$ 0.05 pc and density $n(H_2) \sim 5\times10^5$ cm^{-3}, and it is traced by SO_2, H_2CO and the (5_K–4_K) CH_3OH lines. For both the components we estimate a similar temperature ($T \sim$ 200 K) and time ($t \sim 3\times10^4$ yr) from when the clump has started to interact with the outflow. Since the compact component is traced by the higher energy transitions of CH_3OH, it is probably at higher excitation and may trace the zone of stronger interaction between the outflow and the clump. However, the analysis of the CH_3OH data needs to be confirmed by modelling the data with a radiative transfer code that takes into account the effects of line–overlap (Gray & Yates, in prep). Moreover, a more realistic density and temperature profile for the low-velocity molecular clumps along outflows is necessary. The real structure of the molecular clumps can be detected with high spatial resolution interferometric observations of clumps closer to us than CB3.

Chapter 5

Interferometric observations of the L1157 outflow

The work described in this Chapter has been presented as a poster at the Congress *Science with ALMA: a new era for Astrophysics*, Madrid, 13 – 17 November 2006 and is the basis for a paper in preparation.

5.1 The necessity of high spatial resolution observations

From the analysis of the CB3 outflow clumps in the previous chapters, it is clear that the size of the clumps derived from single dish observations is an upper limit of the real size and that it is not possible for the clumps to have a uniformly high density in a 0.12 pc radius. A density gradient is needed in order to account for the observed emission of most species. That the typical size of the low–velocity clumps is smaller than $\sim$ 0.1 pc is also supported by the fact that the match between the chemical models and the single dish observations improves in L1157 where the size of the clump is reduced to 0.04 pc due to its lower distance (see Sect. 3.6). This is because the larger the size the worse the approximation of a single–density component becomes.

In chapters 3 and 4 the density structure of the clumps was modelled by the density profile derived for starless cores (Tafalla et al., 2002). However

there is no observational evidence that the clumps associated with CB3 and L1157 have a similar density structure to starless cores. Moreover, the outflow clumps show basic differences with respect to the starless cores, for example in the temperature (starless cores have temperature $\leq$ 10 K) and in the chemical structure (in starless cores several species such as CO and CS are depleted in the core center). A direct evidence of the real structure of the outflow clumps can only be achieved through very high spatial resolution observations using an interferometer. Unfortunately, the CB3 outflow is too far (d = 2500 pc) for the interferometric observations to be useful to resolve the small scale structure of the clumps. L1157 is clearly the better target as its distance is only 440 pc.

In fact, in the literature high spatial resolution observations of the blue lobe of the L1157 outflow can be found for: SiO (Zhang et al. 1995; Gueth et al. 1998), NH_3 (Tafalla & Bachiller, 1995) and CS (Zhang et al., 2000). These data reveal a richer structure than can be seen in the observations with the single dish IRAM–30m telescope. In particular, the CS, which is usually used as a density tracer, reveals that the clump B1 breaks into smaller clumps with size of the order of 10 – 15 arcsec (0.02 – 0.03 pc).

A map of the blue lobe of the L1157 outflow has been produced by Pérez–Gutiérrez (1999) in his PhD thesis. In Fig. 5.1 the integrated emission for the four lines HCN (1–0), CH_3OH (2_K–1_K), HC_3N (11–10) and OCS (7–6) observed with the Plateau de Bure Interferometer are shown. The maps with better signal to noise (HCN (1–0) and CH_3OH (2_K–1_K)) show a richness in structure. The B1 and B2 clumps results formed by smaller clumps and new small condensations are detected, one between B1 and B2, one between B1 and B0 and one at north–west of B1 observable also in OCS and marginally in HC_3N. All these clumps are also visible in the NH_3(3,3) map of Tafalla & Bachiller (1995).

These observations however are not sufficient to derive the physical conditions of the clumps. For this reason we applied for time with an interferometer to observe the brightest clump of the blue lobe, B1, in a selected sample of density and temperature sensitive species at a spatial resolution better than the observations of Pérez–Gutiérrez (1999). We were awarded 3 runs of observations with the Plateau de Bure Interferometer.

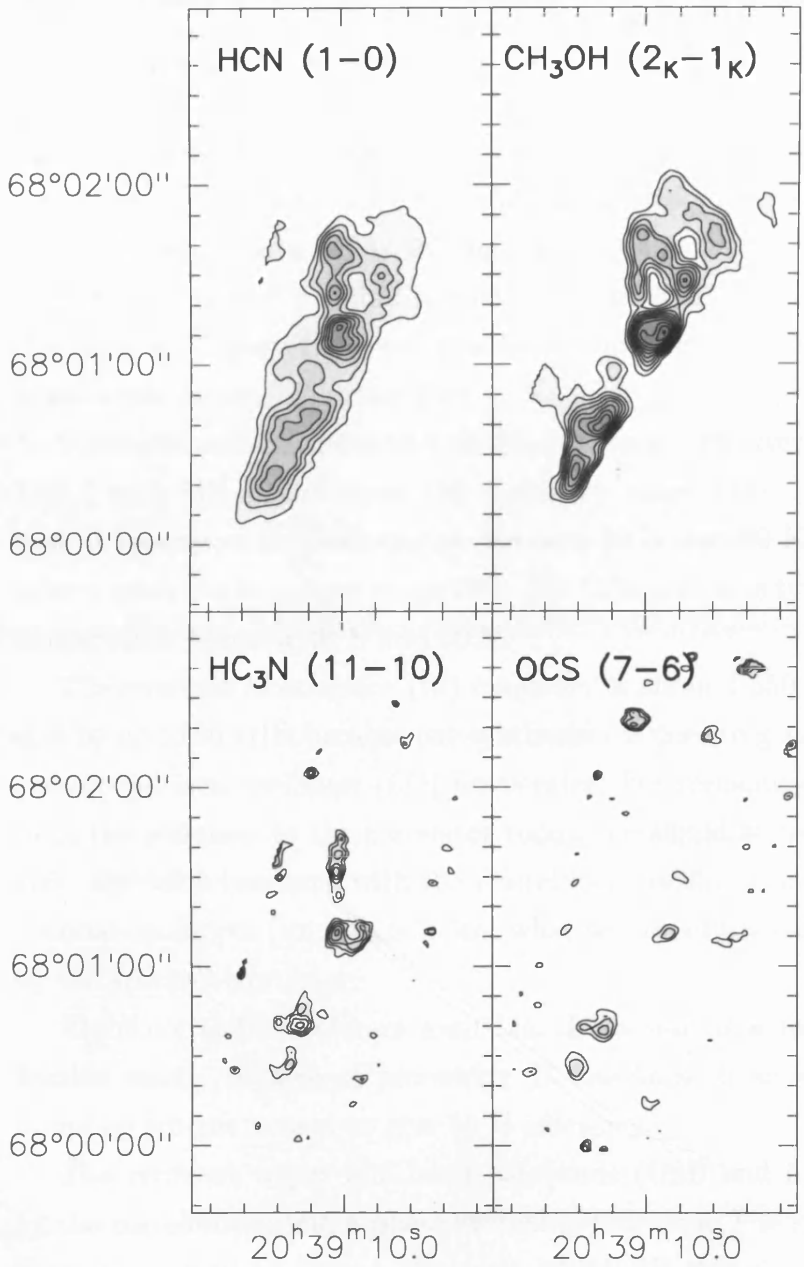

Figure 5.1: Interferometric images of the blue lobe of the L1157 outflow (figure from Pérez–Gutiérrez (1999)). The contours are: for HCN (1–0) first contour 2.5 Jy beam^{-1} km s^{-1}, levels 2 Jy beam^{-1} km s^{-1}; for CH_3OH (2_K–1_K) first contour 4 Jy beam^{-1} km s^{-1}, levels 1.5 Jy beam^{-1} km s^{-1}; for HC_3N (11–10) first contour 0.4 Jy beam^{-1} km s^{-1}, levels 0.15 Jy beam^{-1} km s^{-1} and for OCS (7–6) first contour 0.15 Jy beam^{-1} km s^{-1}, levels 0.05 Jy beam^{-1} km s^{-1}.

5.2 The IRAM Plateau de Bure Interferometer

The Plateau de Bure Interferometer consists of six antennas of 15-meter diameter, that can be positioned on 30 stations arrayed along a "T" shaped track. The north–south arm is 232 m long, and the almost east–west oriented arm extends 216 m west and 192 m east of the intersection. The angle between the arms is 75 deg. Each antenna is a 15 m diameter Cassegrain telescope constructed largely of carbon fiber.

The antennas are equipped with dual–frequency receivers at 1.3 and 3 mm. The 3 mm SIS mixers cover the frequency range 81 – 115 GHz and have typical receiver noise temperature between 30 K and 50 K. The 1.3 mm SIS mixers cover the frequency range 205 – 250 GHz and have typical receiver noise temperature between 40 K and 60 K.

The receivers interference (IF) frequency is about 1.550 GHz, slightly variable by up to 50 MHz because one synthesizer is used to generate both the first and second local oscillator (LO) frequencies. For transmission through cables from the antennas to the correlator room, the signal is down converted to a 100 – 680 MHz baseband with the second local oscillator in each antenna. Additional oscillators (third LOs) select what section of the baseband is analyzed by the spectral correlator.

Eight correlator units are available. Each unit is a totally independent, flexible entity, capable of processing 15 baselines (6 antennas). Full 2–bit sampling scheme is used to give 88 % efficiency.

The receivers upper and lower sidebands (USB and LSB) are separated by the correlators using a phase switching technique.The sideband gain ratio depends on receiver tuning, the ratio USB/LSB changing typically between < 0.01 and 5.0.

Each interferometer "configuration", the 6 antennas on given stations, simultaneously provides 15 baselines (or *uv*–tracks). There are 4 primary configurations with 6 antennas that can be combined to produce maps with different angular resolution. The actual angular resolution depends also on the frequency and the elevation of the source, few example are:

- in the compact configuration D, where the sensitivity is maximum, the angular resolution at 40 degree of declination is 4.87 arcsec at 85 GHz and 1.80 arcsec at 230 GHz;
- in the CD configuration suited for mosaic observations at medium resolution the angular resolution at 40 degree of declination is 3.54 arcsec at 85 GHz and 1.31 arcsec at 230 GHz;
- in the highest resolution AB configuration the angular resolution at 40 degree of declination is 1.69 arcsec at 85 GHz and 0.63 arcsec at 230 GHz.

5.3 Observations and data reduction

We observed the bright B1 clump (R.A. (J2000) $20^h39^m9^s.5$; dec (J2000) $68°01'15''$) in the blue lobe of the L1157 outflow between September and November 2004 with the aim to reveal its small scale structure. The correlator units were configured in order to observe simultaneously CS (2–1) at 97.981 GHz and CS(5–4) at 244.935 GHz. These lines are usually optically thin and can be used to derive the gas density (Cesaroni et al., 1991). Moreover, we observed the CH_3OH (5_K–4_K) transitions at 241.791 GHz to obtain a good estimate of the temperature. The ^{34}SO (3_2–2_1) at 97.71 GHz and CH_3OH (2_1–1_1) A^- at 97.583 GHz are automatically covered by the setting of the autocorrelator units that were configured in order to have a resolution of 0.5 km s^{-1} at 3 mm and 0.8 km s^{-1} at 1.3 mm. In order to detect gradients of the physical conditions inside the clump, the CD configuration was used with 6 or 5 antennas (5D+6Cp) obtaining a spatial resolution of the order of 3 arcsec at 97 GHz and 1 arcsec at 240 GHz.

An interferometer produces the visibility i.e. the Fourier transform of the product of the primary beam patterns of the antennas and the brightness distribution of the observed source. The antennas, receivers, cables, and correlators all introduce modifications to this visibility so that a calibration process is necessary to recover the signal of the source from the visibility. This process is quite complex; it consists of a number of steps: some are done in real time

Table 5.1: Journal of the observations.

transition	freq. (GHz)	Δv (km s^{-1})	synthetized beam (arcsec × arcsec)	rms (Jy beam^{-1})
CH_3OH $(2_1–1_1)A^-$	97.583	0.5	3.14×2.82 (P.A.=69°)	0.003
^{34}SO $(3_2–2_1)$	97.715	0.5	3.14×2.81 (P.A.=69°)	0.003
CS (2–1)	97.981	0.5	3.11×2.79 (P.A.=70°)	0.009
CH_3OH $(5_K–4_K)$	241.791	0.8	1.08×0.91 (P.A.=118°)	0.008
CS (5–4)	244.935	0.8	1.14×0.97 (P.A.=118°)	0.008

during the data acquisition, i.e. atmospheric calibration, antenna calibration, gain of the receivers; the other steps, such as band pass calibration, phase calibration, amplitude calibration and flux calibration are performed after the data acquisition.

Calibration needs the observation of other sources close to the target. In our observations, the phase and amplitude calibrations are achieved by observations of the quasar 2037+511 and the Seyfert galaxy 1928+738, which are close to L1157 on the sky. The band pass of the receivers were calibrated by observations of the quasar 2145+067 (25 and 30 Sept.) and 1928+728 (24 Nov.) and the flux scale was derived from observation of the star MWC 349.

The data were calibrated and analyzed with the GILDAS software, the images were produced using natural weighting and the artifacts caused by the incomplete coverage of (u, v) space are eliminated by the CLEAN routine.

The details of the observations are summarized in Table 5.1.

5.4 Results

5.4.1 3 mm data

The 3 mm observations have been performed with excellent weather conditions. The mapped zone of about 40×40 arcsec^2 around the B1 clump, reveals a rich structure with the detection of several sub–clumps traced by different species. The identified sub–clumps are listed in Table 5.2 with their coordinates.

The CS (2–1) map is shown in Fig. 5.2. The B1 clump is resolved in three

Table 5.2: Clumps identified in the zone of 40×40 arcsec^2 around the B1 clump of L1157 outflow.

clump	R.A.(J2000)	dec (J2000)
	h m s	$\circ$ $'$ $''$
B1a	20 39 10.0	68 01 13.6
B1b	20 39 08.8	68 01 10.0
B1c	20 39 10.4	68 01 07.0
B1d	20 39 09.2	68 01 04.4
B4	20 39 07.7	68 01 28.0
B5	20 39 10.5	68 01 23.1

sub–clumps that we label B1a ($20^h39^m10^s.0$, $68°01'13''.6$), B1b ($20^h39^m08^s.9$, $68°01'09''.7$), and B1c ($20^h39^m10^s.4$, $68°01'07''.4$). The sub–clumps are located in a clear arch-shaped form with B1c showing the strongest emission. We detect also a diffuse component that is elongated in the south direction similarly to what is seen in the SiO map by Gueth et al. (1998). The elongated feature is clearly visible in the channels map (Fig. 5.3) in the -4.4 km s^{-1} channel. In the B1a position a second velocity component is identified in addition to the main component centered at 0 km s^{-1}. As one can see from the the channel map (Fig. 5.3), the second component peaks at -11.4 km s^{-1} and extends up to -16 km s^{-1}. This component is also present in the SiO (3–2) line observed by (Bachiller et al., 2001). A new clump not revealed by the previous single dish observations (Bachiller et al., 2001), labelled B5 ($20^h39^m10^s.5$, $68°01'23''.1$), is detected north of B1. The shape of the B5 sub–clump changes with the velocity, it is circular at blue velocities and becomes elongated toward B1 at velocities greater than 0 km s^{-1}. As in B1a the emission in B5 starts at -16 km s^{-1} a velocity bluer than the typical terminal velocity of the map of $\sim$ -8 km s^{-1}.

In the CH_3OH (2_1–1_1) A^- line two sub–clumps have been detected in the B1 position B1b ($20^h39^m8^s.8$, $68°01'10''.6$) and B1c ($20^h39^m10^s.6$, $68°01'06''.1$). The emission has a round shape clearly brighter toward B1b without the elongated structure toward the south detected in the CS map. The peak position of the B1b clump seems to be shifted toward the south at higher velocity (see

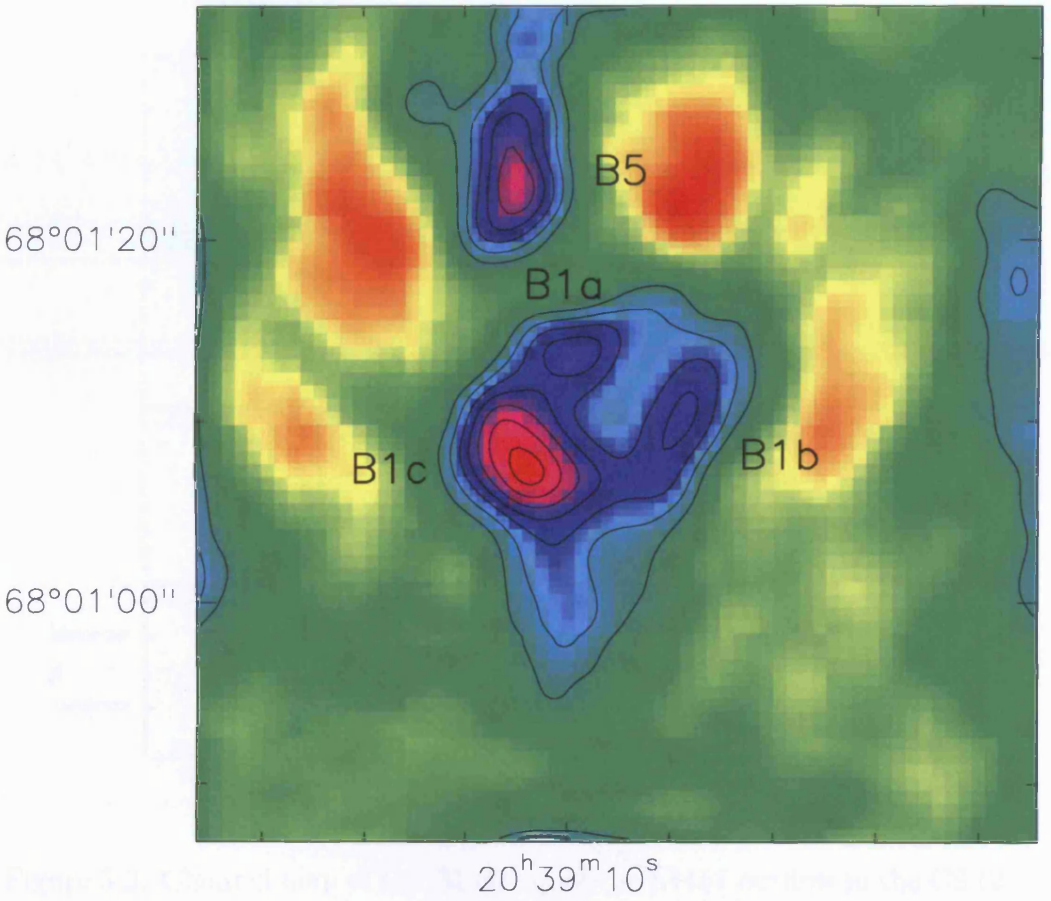

Figure 5.2: Map of the B1 clump of the L1157 outflow in the CS (2–1) line at 97.98 GHz. First level is 0.027 Jy beam^{-1} (3σ), level steps are 0.02 Jy beam^{-1}.

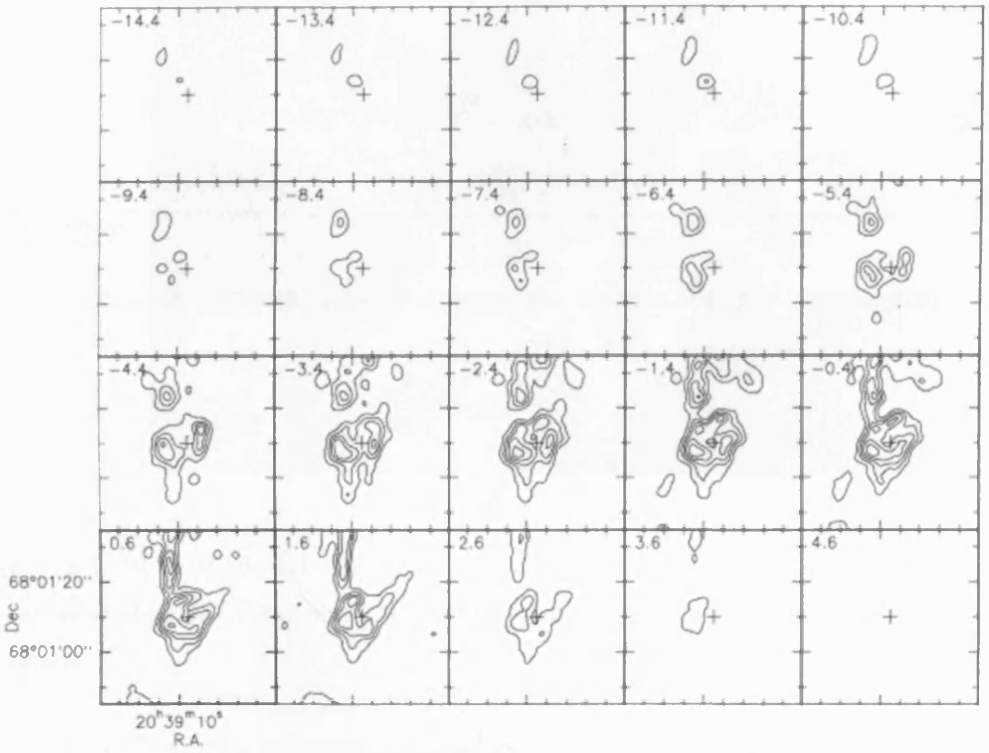

Figure 5.3: Channel map of the B1 clump of the L1157 outflow in the CS (2–1) line at 97.98 GHz. First level is 0.05 Jy beam^{-1} (3σ), level steps are 0.07 Jy beam^{-1}.

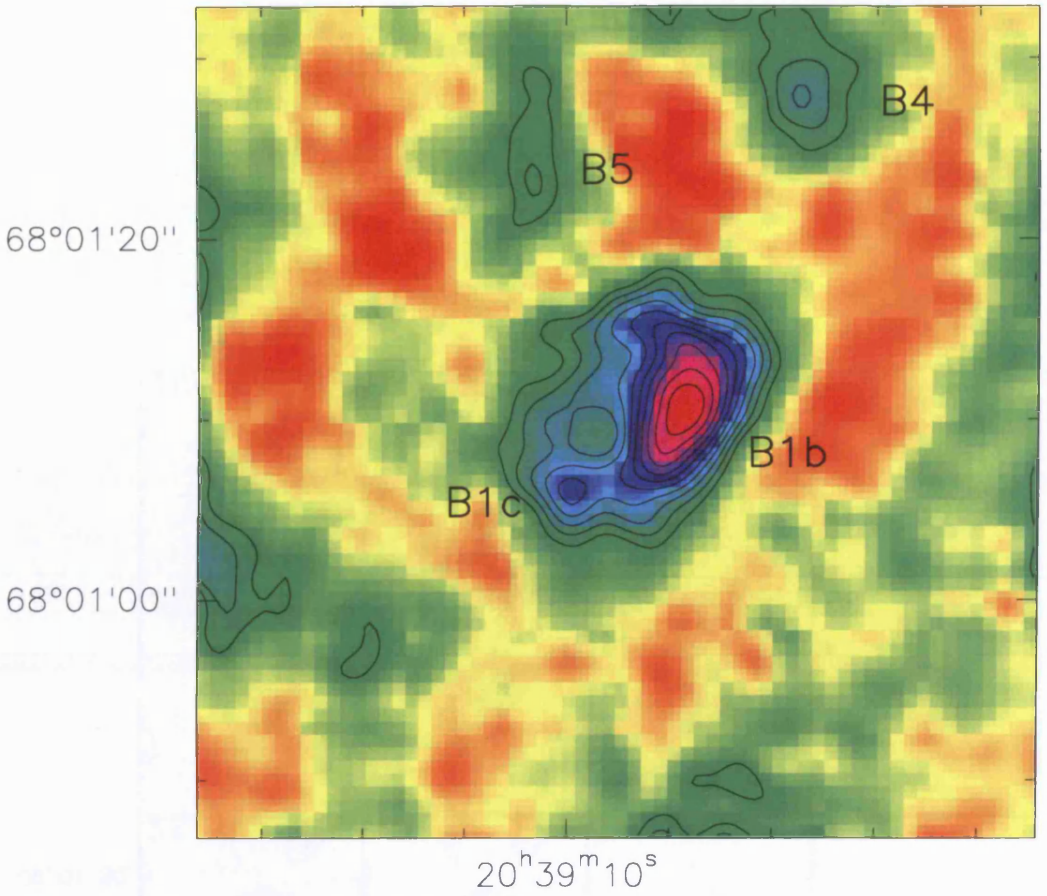

Figure 5.4: Map of the B1 clump of the L1157 outflow in the CH_3OH (2_1–1_1) A^- at 96.582 GHz. First level is 0.009 Jy beam^{-1} (3σ), level steps are 0.005 Jy beam^{-1}.

Fig. 5.5). Indeed, the emission peaks at an offset of (-5″,3″) with respect to the center of the map in the -3 km s^{-1} channel and at an offset (-5″,-6″) in the 5 km s^{-1} channel. In the northern part of the map two clumps are detected, B5 ($20^h39^m10^s.3$, 68°01′24″), visible also in CS, and B4 ($20^h39^m07^s.7$, 68°01′28″) north–west of B1.

The quality of the ^{34}SO map (see Fig. 5.6) is worse than the other two maps due to the lower signal of the line; however three sub–clumps are clearly detected: the two already detected in CS and CH_3OH, B1a ($20^h39^m10^s.5$, 68°01′12″.1) and B1b ($20^h39^m08^s.7$, 68°01′09″.2) and a new one, B1d ($20^h39^m09^s.2$, 68°01′04″.4), at an intermediate position between B1b and B1c.

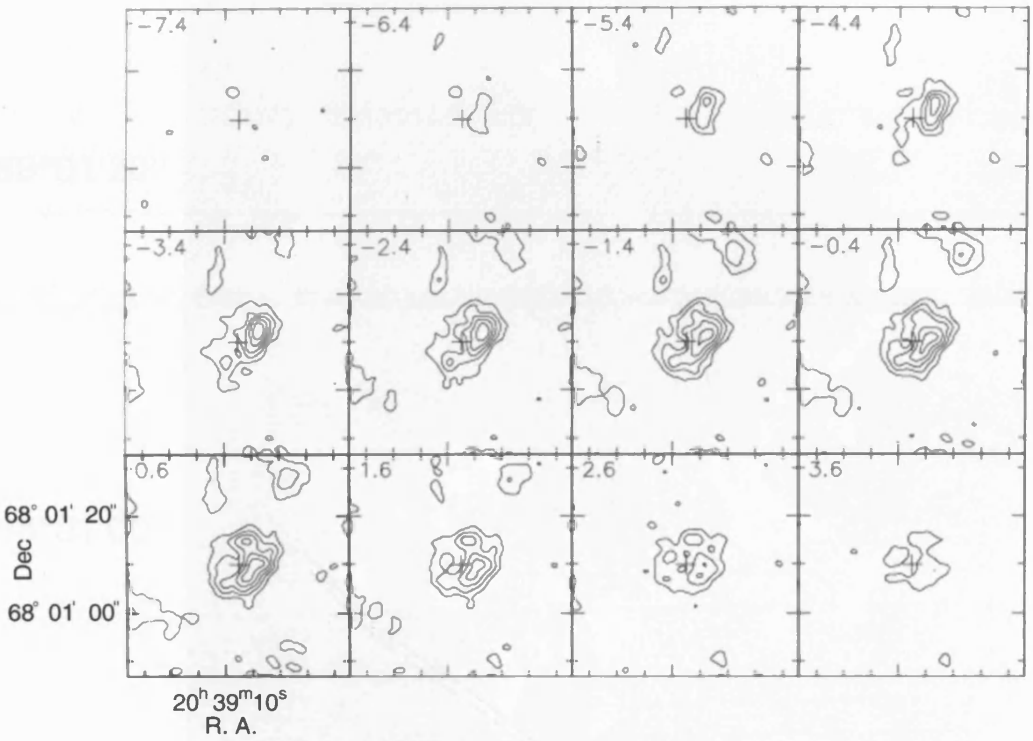

Figure 5.5: Channel map of the B1 clump of the L1157 outflow in the CH_3OH (2_1–1_1) A^- at 96.582 GHz. First level is 0.01 Jy beam^{-1} (3σ), level steps are 0.015 Jy beam^{-1}.

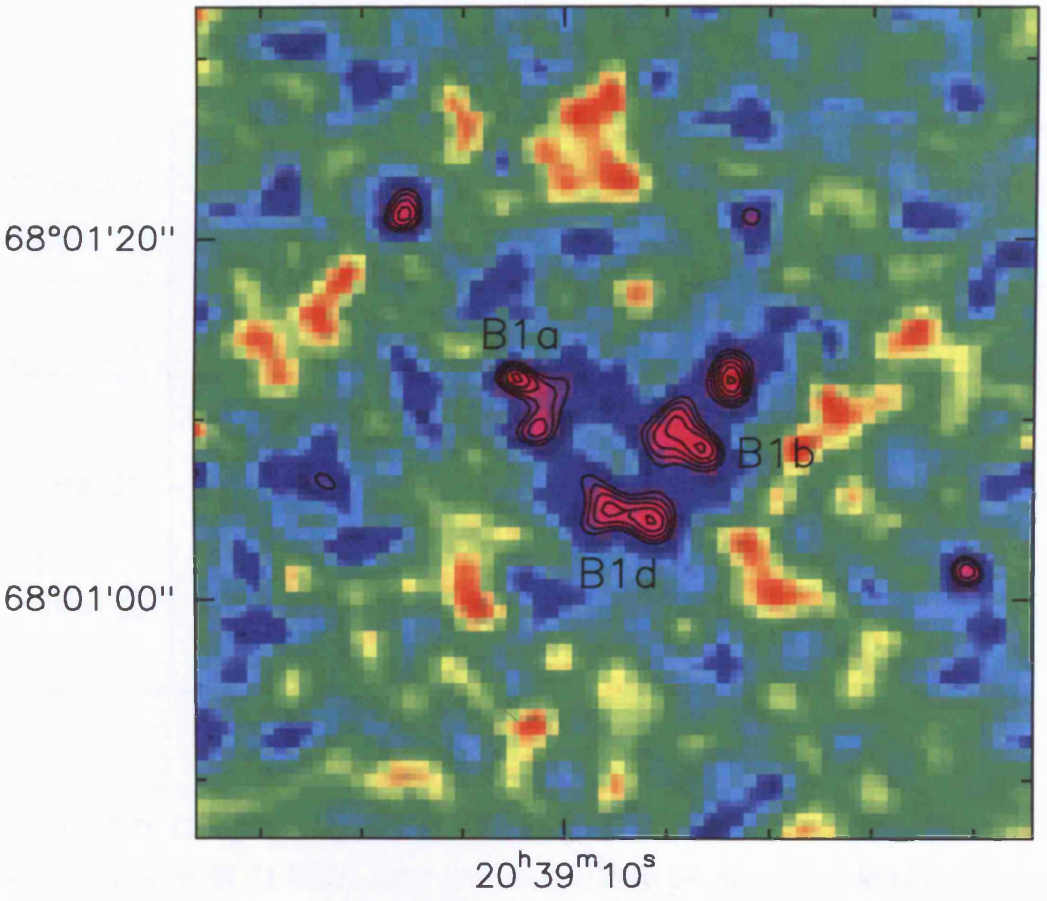

Figure 5.6: Map of the B1 clump of the L1157 outflow in the ^{34}SO (3_2–2_1) line at 97.71 GHz. First level is 0.0075 Jy beam^{-1} (3σ), level steps are 0.001 Jy beam^{-1}.

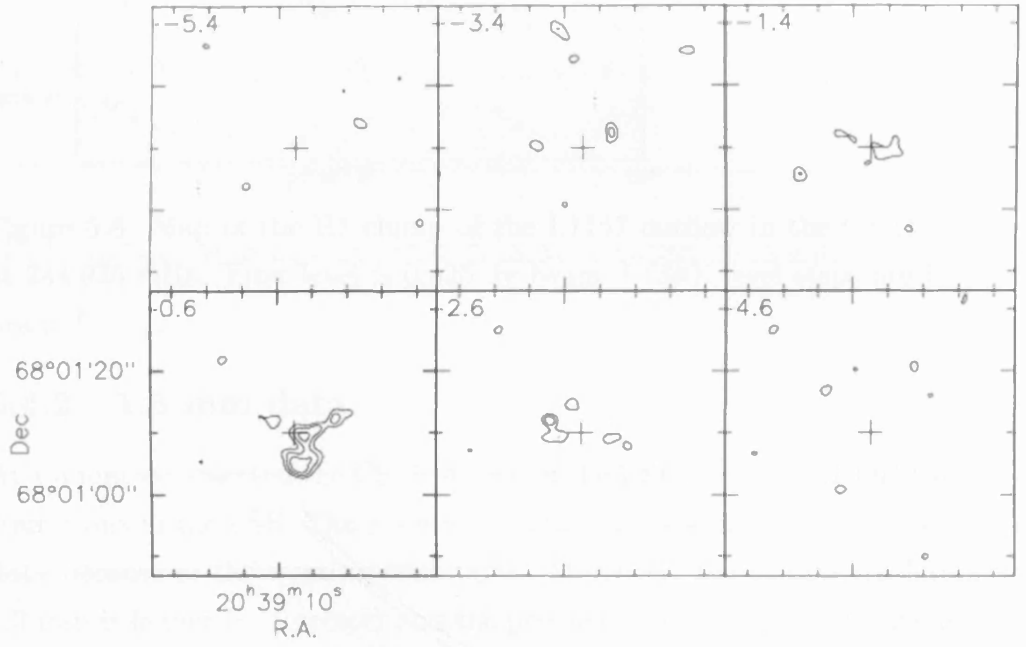

Figure 5.7: Channel map of the B1 clump of the L1157 outflow in the ^{34}SO (3_2–2_1) line at 97.71 GHz. First level is 0.015 Jy beam^{-1} (3σ), level steps are 0.005 Jy beam^{-1}.

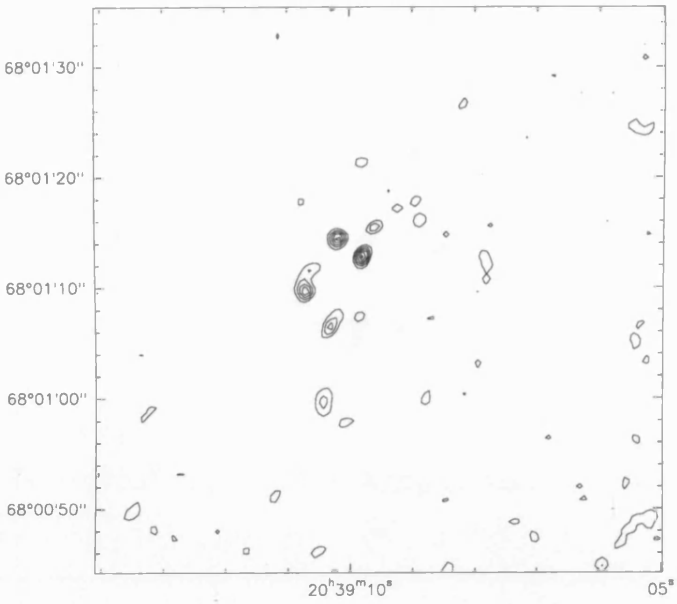

Figure 5.8: Map of the B1 clump of the L1157 outflow in the CS (5–4) line at 244.935 GHz. First level is 0.025 Jy beam^{-1} (3σ), level steps are 0.02 Jy beam^{-1}.

5.4.2 1.3 mm data

At 1.3 mm we observed the CS (5–4) line in the USB and the CH_3OH (5_K–4_K) transitions in the LSB. The 1.3 mm data are of worse quality than the 3 mm data because of the weather conditions. Moreover, the spatial resolution at 1.3 mm is higher ($\sim$ 1 arcsec) and the primary beam is smaller ($\sim$ 20 arcsec) than at 3 mm. In interferometers the emission from structures extended more than 2/3 of the primary beam are filtered out by the interferometer, therefore only the very compact peaks ($\leq$15 arcsec) can be detected. The extended emission could be partially recovered by convolving the interferometric data with single dish observations. Unfortunately, single dish data for these lines are not available and in any case the coverage of the (u,v) plane at 1.3 mm is too poor to have a significant improvement from the convolution process.

In Fig 5.8 we show the map of the CS (5–4) line. One can see few small structures in the east side of the B1 lobe; however the quality of the image is so poor that no further analysis can be done. Similarly, in the CH_3OH (5_K–4_K) transitions few compact structures are detected but the quality is quite poor.

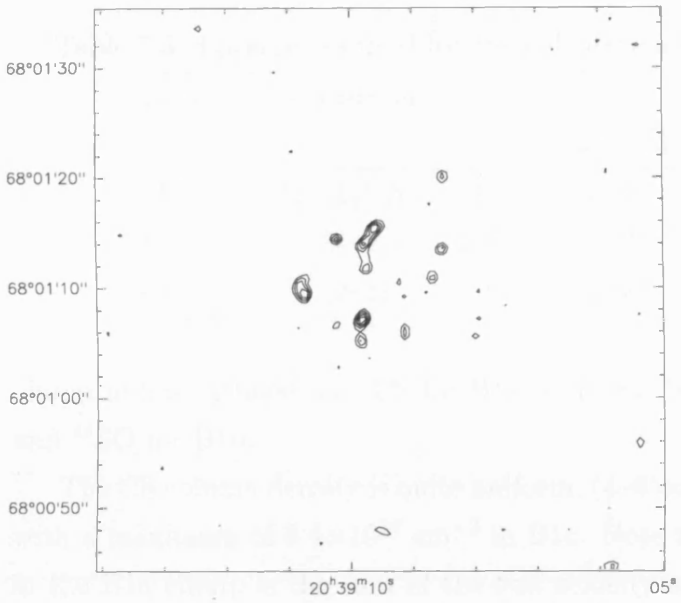

Figure 5.9: Map of the B1 clump of the L1157 outflow in the CH_3OH (5_{-1}–4_{-1}) E line at 241.767 GHz. First level is 0.02 Jy beam^{-1} (3σ), level steps are 0.01 Jy beam^{-1}.

The (5_{-1}–4_{-1}) E line at 241.767 GHz is shown in Fig. 5.9.

5.5 Column densities

In LTE conditions the molecular column density can be derived from the integrated intensity of an emission line assuming that the it is optically thin, using the formula Eq. 3.4 that is reproduced here for ease of reading

$$N = 1.67 \times 10^{14} \frac{Q(T_{rot})}{\mu^2 \nu S} exp\left(\frac{E}{kT_{rot}}\right) \int T_{MB}\, dv \qquad (5.1)$$

where $Q(T_{rot})$ is the partition function, μ is the dipole momentum, ν is the frequency, S is the line strength and E is the energy of the upper level of the transition. The value of these parameters for the observed lines are listed in Table 5.3. In Table 5.4 the column densities toward the detected sub–clumps for the three observed molecules are reported. For all the clumps we assume the temperature of 80 K derived in B1 by means of NH_3 data (Tafalla & Bachiller, 1995). The area used to calculate the column density is the same for all the molecules in each clump and it has been defined using the molecule where the

Table 5.3: Parameters used for the calculation of the column densities.

molecule	transition	S	μ (debeys)	E/k (K)	Q(80K)
CH_3OH	$(2_1–1_1)$ A^-	1.5	0.885	21.56	916
^{34}SO	$(3_2–2_1)$	2.435	1.55	9.09	216
CS	(2–1)	2	1.96	7.06	68

clump is best defined, i.e. CS for B1a, B1c and B5, CH_3OH for B1b and B4 and ^{34}SO for B1d.

The CS column density is quite uniform, $(4–6)\times10^{14}$ cm^{-2}, in all the clumps with a maximum of 6.4×10^{14} cm^{-2} in B1c. Note that the CS column density in the B1a clump is the sum of the two velocity components detected in this position. On the other hand, the methanol column density shows a higher value, 1.2×10^{16} cm^{-2}, in the B1b clump with respect to the typical value of the other clumps, $(2–5)\times10^{15}$ cm^{-2}. The ^{34}SO column density is about 3×10^{13} cm^{-2} in B1a and B1c while is slightly higher, $(8–9)\times10^{14}$ cm^{-2}, in B1b and B1d.

Bachiller & Pérez–Gutiérrez (1997) derived the column density of the same molecules averaged over the whole B1 clump using the single dish IRAM–30m data. In particular, they estimated N(CS) = 2.7×10^{14} cm^{-2} and N(CH_3OH) = $(0.5–2.6)\times10^{15}$ cm^{-2}. They observed ^{32}SO instead of ^{34}SO. However, if we multiply N(^{34}SO) by the isotopic ratio $^{32}S/^{34}S = 22$ we can estimate N(^{32}SO) = $(6–20)\times10^{14}$ cm^{-2}, comparable with the value of Bachiller & Pérez–Gutiérrez (1997) of $(3–5)\times10^{14}$ cm^{-2}. The two sets of estimates are in agreement if one considers that the values derived from the Plateau de Bure interferometer data are calculated over the small peaks of the sub–clumps while the values derived from the IRAM–30m observations are averaged over the larger area of the whole B1 clump. The fact that the single dish and the interferometric data give similar values of the column densities testifies that the large scale emission filtered out by the interferometer is negligible.

Table 5.4: Molecular column densities in the detected clumps and column density ratio.

clump	$N(CH_3OH)$ (cm^{-2})	$N(^{34}SO)$ (cm^{-2})	$N(CS)$ (cm^{-2})	$\frac{N(CH_3OH)}{N(CS)}$	$\frac{N(CH_3OH)}{N(^{34}SO)}$	$\frac{N(^{34}SO)}{N(CS)}$
B1a	3.4×10^{15}	3.6×10^{13}	5.5×10^{14}	6	94	0.06
B1b	1.2×10^{16}	8.3×10^{13}	4.1×10^{14}	29	145	0.20
B1c	3.5×10^{15}	2.6×10^{13}	6.4×10^{14}	6	135	0.04
B1d	5.0×10^{15}	9.0×10^{13}	3.1×10^{14}	16	56	0.29
B4	3.6×10^{15}	...	...	...	...	...
B5	2.3×10^{15}	...	5.3×10^{14}	4.3	...	...

5.6 Analysis of the maps

B1 has a well defined arch–shaped form with the four sub–clumps (B1a, B1c, B1d and B1b in anti–clockwise order) outlining the arch. The arch spatially corresponds with the apex of the C2 cavity observed in the high resolution CO (1–0) map (Gueth et al., 1996). The C2 cavity, as well as the other similar structure C1 detected in the B2 position, have been likely created by the propagation of large bow–shocks due to a highly collimated jet. Our maps support this scenario since the arch–shaped clumps at the apex of the cavity may trace the front of the bow–shock.

The observed molecules peak in different parts of the arch. In particular, the CS emission is brighter east–side while CH_3OH is brighter west–side. Considering also the other interferometric maps found in the literature (SiO (2–1) (Zhang et al. 1995; Gueth et al. 1998), NH_3 (3,3) (Tafalla & Bachiller, 1995), HCN (1–0), CH_3OH (2_K–1_K), HC_3N (11–10) and OCS (7–6) (Pérez–Gutiérrez, 1999)) we can identify two groups of molecules, one peaking west–side and the other peaking east–side. In particular, the B1a clump is brighter in HC_3N (11–10), HCN (1–0), NH_3 (3,3) and SiO (2–1) while B1b is brighter in CH_3OH (2_K–1_K), OCS (7–6) and ^{34}SO (3_2–2_1). The B1c clump is well defined and bright only in the CS (2–1) map. The different behaviour between the east and west parts of the map is still evident among the column densities (see Table 5.4). Indeed the $N(CH_3OH)/N(CS)$ ratio is significantly higher in the

west part (29 in B1b and 16 in B1d) than in the east part (6 in B1a and B1c and 4 in B5). Similarly N(^{34}SO)/N(CS) is higher in the west (0.20 in B1b and 0.29 in B1d) than in the east (0.06 in B1a and 0.044 in B1c). Since the CS column density is quite constant throughout the map the difference in the ratio is an indication of an overabundance of methanol and sulfur oxide in the west part of the B1 clump, especially in B1b for CH_3OH and in B1d for ^{34}SO. This result is independent of the assumption that the temperature of 80 K is constant throughout the B1 clump. In fact, this temperature was derived from the NH_3 lines (Tafalla & Bachiller, 1995) so it is suitable for the east clumps where the ammonia peaks but it may not be suitable for methanol, which peaks in the west. If the temperature in the B1b clump is lower than 80 K the methanol column density could be lower than the derived value of 1.2×10^{16} cm^{-2}. However, even assuming $T = 10$ K, the methanol column density does not change significantly.

Our original plan was to use the two lines (2–1) and (5–4) of CS to derive the density and the methanol lines to derive the temperature. Unfortunately the 1.3 mm data are not usable for this purpose. However, some qualitative conclusions can be made from the available maps that show the clumpiness of the B1 clump and the inhomogeneity of the physical conditions of the observed sub–clumps. In particular, we find that the density is different among the sub–clumps; indeed molecules such as CS, HC_3N, and HCN, that have a high critical density, peak on the east side of B1, indicating that B1a and B1c could be the sites of highest density.

The high spatial resolution maps show also the presence of a chemical structure inside the B1 clump that represent the apex of the bow shock. In particular, molecules such as SiO, NH_3, and CH_3OH that are considered shock tracers show a different spatial distribution, with SiO and NH_3 peaking about 10 arcsec east of the peak of CH_3OH. Moreover the CS peak is displaced about 7 arcsec from the NH_3 peak, which is unexpected since the two molecules should trace the same high density gas. We believe that these displacements cannot be fully accounted for by the lower spatial resolution of the SiO and NH_3 maps (9 arcsec and 5 arcsec, respectively) with respect to the CS and CH_3OH maps (3 arcsec).

A displacement between the CS and NH_3 peaks is usually observed in starless cores (Pastor et al. 1991; Myers et al. 1991b; Morata et al. 1997). Two interpretations have been proposed: *i)* chemical differentiation inside the cores, with the drop of the CS abundance toward the core center due to the depletion of this molecule onto dust grains at a density of (2–6) $\times 10^{4}$ cm^{-3} (Tafalla et al., 2002); *ii)* different time dependencies of the chemistry of the two molecules; in fact ammonia is slow to form with respect to CS and it is possible that several cores have time to develop CS but that some of them are destroyed before appreciable NH_3 is formed (Taylor et al., 1996). Of course clumps along outflows are different from starless cores, and in our case, it is possible that the displacement would be due to a difference in the density of the B1a and B1c sub–clumps, indeed CS should trace higher density gas than NH_3 since its critical density is slightly higher ($\sim 10^5$ cm^{-3} for CS and $\sim 10^3$ cm^{-3} for NH_3). Alternatively, it could be an indication of a different age of the two sub–clumps, with the B1a clump being old enough to have had time to form more ammonia.

Ammonia and methanol are abundant on grain ice mantles (Charnley et al., 1992) and they evaporate in the gas phase as the temperature increases above 120 K (Collings et al., 2004). In the chemical models described in Chapter 4 we see that their abundance does not change significantly for at least 10^5 years independent of the presence or the absence of the non–dissociative shock (i.e. a high temperature phase with $T \sim 1000$ K). On the other hand, SiO is rapidly formed in the gas phase after the release of significant amounts of silicon from the refractory cores of dust grains at the passage of the shock front (Pineau des Forêts et al., 1997). SiO reacts with OH to form SiO_2 and after 10^4 yr its abundance rapidly decays. The fact that methanol and ammonia can survive better than SiO after the passage of the shock suggests that the east side of the B1 clump where the density is higher and the SiO is more abundant would be the zone much closer to the shock front, while the B1b clump is more distant.

For a few tracers (CS and ^{34}SO) the emission is elongated toward the south, showing a linear structure also visible in the SiO map (Gueth et al., 1998). Gueth et al. (1998) suggested that this protuberance is the magnetic precursor of the shock. The presence of a diffuse CS emission in this zone

is consistent with this picture, indicating an enhancement of the density as a consequence of the precursor of the shock.

The two B4 and B5 clumps observed north of B1 are located at the walls of the C2 cavity. Their observational properties are similar to what is observed in B1. The CS emission is detected only in B5 and this clump is bright also in the HCN (1–0) (see Fig. 5.1) and NH_3 (3,3) (Tafalla & Bachiller, 1995) transitions indicating that this east clump has a high density. On the other hand, the west B4 clump is bright in CH_3OH (2_K–1_K) and NH_3 (1,1) but it is less intense in HCN (1–0) and NH_3 (3,3) and it is not observed at all in CS (2–1). This indicates that the density in the west B4 clump could be less than that in the east B5 clump.

In summary, our observations of the B1 clump in the L1157 outflow confirms what was found in the analysis of the the low–velocity clumps observed in the CB3 and L1157 outflows (see Chapter 4). What is seen as a single molecular clump with size of the order of 0.1 – 0.04 pc by the single dish telescope, when observed at high resolution shows a structure both in its physical conditions and in its chemical composition on a scale of the order of 0.02 pc.

5.7 Chemical modelling

Chemical modelling of the Plateau de Bure observations can be done using the chemical models developed for the IRAM–30m data on the CB3 clumps, scaled for the different distance and size of the clumps of L1157.

In order to have an idea of how the observed column densities are sensitive to the model parameters we selected five models, varying the density, the temperature and the percentage of freeze–out. The other parameters are fixed: free–fall collapse, instantaneous evaporation, depleted sulphur initial abundance X(S) = 1.3×10^{-7}. Since we want to model the small sub–clumps that have sizes of the order of 0.02 pc, we can reasonably assume that the density and the temperature are constant in the clump. We consider only the best case scenario from the previous analysis i.e. the clump is believed to be pre–existent to the advent of the outflow and undergoes a phase of non–dissociative shock. The parameters of the selected models are summarized in

Table 5.5: List of models and their parameters.

model	n(H_2) 10^5 (cm^{-3})	T (K)	FR (%)
As1	5	210	30
As2	1	210	30
B2	10	110	60
B7	10	210	60
B10	10	210	20
B12	5	210	60

Table 5.5.

The theoretical column densities at $t = 10^5$ yr for CS, SO, NH_3, and CH_3OH are derived using the formula given in Eq. 3.5 of Chapter 3 and listed in Table 5.6. The theoretical column densities are compared with with the observed column density in each sub–clump (see Table 5.4). One can see that the model As2 with the lower density ($n(H_2) = 10^5$) cm^{-3}, predicts too low column densities. All the other models predict SO column densities lower than the observed one but within the same order of magnitude. The models with higher density, $n(H_2) = 10^6$ cm^{-3}, are the ones that produce the higher CH_3OH column density with the same value observed in B1b while the models with $n(H_2) = 5{\times}10^5$ cm^{-3} give a value similar to what is observed in the B1a, B1c and B5 clumps. Model As1 is also able to reproduce the CS column density of the B1a, B1c and B5 clumps. The models have a temperature of 200 K, higher than the value of 80 K derived from the NH_3 lines; however the B2 model that has a lower temperature of 100 K gives a worse agreement with the CS and SO data with respect to the model B7 that has the same parameters but a higher temperature.

In Fig. 5.10 we show how the column densities evolve with time for the 4 models As1, B2, B7 and B10. As already mentioned ammonia and methanol remain constant as the two species are formed on the grain mantles and are injected into the gas phase during the high temperature phase. On the other hand CS and SO are more time dependent. The fact that the SO column

Table 5.6: Column densities (in cm^{-2}) for a selected set of molecules at $t = 10^5$ yr.

mol	As1	As2	B2	B7	B10	B12
CS	6.10(14)	7.08(13)	1.35(15)	5.64(14)	2.28(15)	2.08(14)
SO	1.45(14)	3.39(13)	8.09(13)	3.12(14)	3.13(14)	1.74(14)
NH_3	6.10(17)	1.57(17)	1.32(18)	1.48(18)	8.98(17)	9.58(17)
CH_3OH	4.22(15)	6.19(14)	1.31(16)	1.09(16)	1.08(16)	4.37(15)

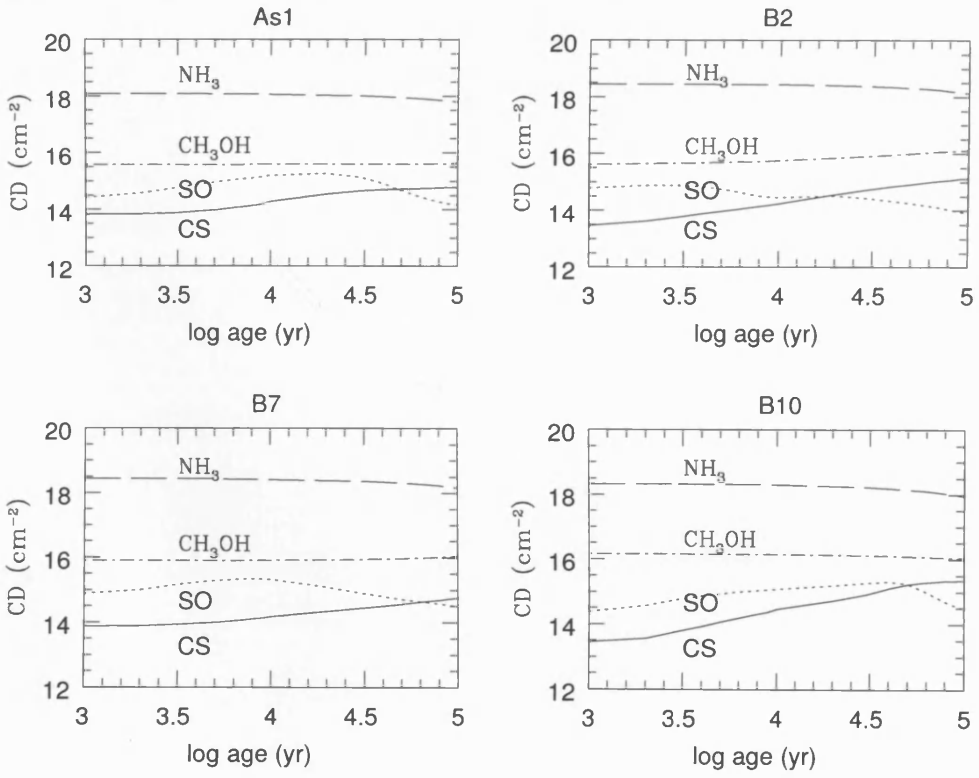

Figure 5.10: The column densities for a selection of species versus time.

density at t=10^5 yr is lower than the observed values suggest that the clump in L1157 may be younger than 10^5 yr.

In summary, from this very first analysis we can say that the temperature of the clumps could be higher than the previous estimate of 80 K by Tafalla & Bachiller (1995) from the NH_3 lines and that the clump B1b seems to have a higher density than the B1a and B1c clumps. However, this is in contrast with the qualitative analysis of the maps (see Sect. 5.6) since we expected to find a higher gas density in the clumps where molecules with higher critical density peak, i.e. in B1a and B1c. A more detailed modelling needs to be developed for constraining the physical parameters of the gas in the sub–clumps.

Chapter 6

Conclusions and Future work

6.1 Conclusions

We have presented the first detailed modelling of the small ($d \leq 0.1$ pc), low velocity ($v \leq 10$ km s^{-1}) clumps observed along the lobes of the chemically active outflows such as CB3 and L1157. In Chapter 3 we developed a time dependent chemical model where the chemical evolution of these clumps was explored. Two scenarios for the clump formation and evolution were investigated: *i)* the clumps are partially pre–existing to the outflow, meaning that the density structure is formed before the advent of the outflows, or alternatively *ii)* the clumps are newly formed by the impact of the outflow on the surrounding medium. The effects of the impact of the outflow are reproduced by density and temperature changes in the clump. The chemical abundances predicted by the chemical model have been used to derive the theoretical column densities that have been compared with the observed ones derived by IRAM-30m data. This preliminary study was aimed at finding some observable tracers that could help us understanding the origin of the clumps with respect to the outflow.

The first results indicate that the initial sulphur abundance of the gas forming the clump can not be solar but it must be depleted of a factor of $\sim$ 100 and that a substantial freeze out must occur during the formation of the clump, regardless of its mode of formation. Moreover, we find that it is not possible for the outflow clumps to have a uniform high density within the 0.12

pc size: a density gradient inside the large single dish beam is needed in order to account for the observed emission of most species.

The shortcomings of such an analysis are that the estimates of the column densities derived from the chemical models, as well as those derived from the observations, suffer from high uncertainties due to the fact that some of the parameters required to calculate them may be unknown. In particular, to estimate the observed column densities arbitrary assumptions have to be made regarding LTE conditions, excitation temperatures and the lines being optically thin. On the other hand, the theoretical calculation of column densities from the chemical model required knowledge of the geometry of the emitting region. However, when dealing with small emitting regions, such as the low velocity clumps along molecular outflows, the observations (in our case single dish with spatial resolution of few tens of arcsec) do not constrain such geometry.

One way to reduce the number of arbitrary assumptions is to model directly the observed line emission using a radiative transfer model that predicts the line profile. In Chapter 4 we attempt such an approach by coupling the time dependent chemical model with the radiative transfer code SMMOL to model in detail the S1 clump of the CB3 outflow.

Different scenarios for the formation of the clump have been investigated within a large range of physical conditions. The models that better reproduce all the observed lines are those where the clump is formed, at least partially prior to the advent of the outflow. The advent of the outflow on the clump leads to a short phase of high temperature ($T \sim 1000$ K) followed by fast cooling down to temperatures of ~ 200 K, the consequent release of the icy mantle together with the high temperature chemistry leads to the observed chemical enrichment.

In addition to the large scale outflowing gas traced by the non–Gaussian wings detected in the CO (2–1) line, at least two other components inside the large IRAM-30m beam are identified. The extended component ($d = 0.12$ pc) is traced by CS and SO and probably by the lower energy transitions (3_K–2_K and 2_K–1_K) of CH_3OH. The second component is more compact, with size $\sim$ 0.05 pc, and it is traced by SO_2, H_2CO and the CH_3OH 5_K–4_K lines. Since the

compact component is traced by the higher energy transitions of CH_3OH, it is probably at higher excitation and may trace the zone of stronger interaction between the outflow and the clump.

The presence of sub–structures in the clumps detected with the large beam of the single dish telescope has been observationally proved by the high spatial resolution maps obtained with the Plateau de Bure interferometer toward the B1 clump of the nearby L1157 outflow. B1 is seen as a single clump with size of 0.04 pc by previous IRAM-30m observation while our interferometric observations reveal that it is formed by four sub–clumps with a clear arch-shape form displaced at the apex of a bow shock. We find that the observed molecules peak in different parts of the arch. In particular, the CS emission is brighter east–side while CH_3OH is brighter west–side. Qualitative considerations based on the distribution of the molecular emission and first quantitative estimates computed applying the chemical models developed for CB3 and rescaled for the different size and distance of the L1157 clumps, indicate that a gradient in gas density and chemical composition is present among the sub–clumps detected in B1.

Understanding the nature of these clumps may have wider implications than just constraining their origin. If the pre–existing nature of the low velocity clumps observed along outflows is correct, they may indeed be a further evidence of the clumpiness of dark molecular clouds.

6.2 Future work

In Chapter 5 we did a very preliminary analysis of the Plateau de Bure data in the L1157 outflow using the chemical models developed for the CB3 data and considering the different size and distance in the calculation of the column density. However, a more detailed analysis is possible. New chemical and radiative transfer models should be developed exploring a parameter space more appropriate for the clumps of L1157 outflow.

From the analysis of the interferometric maps we inferred that the chemical and physical conditions are different among the observed sub–clumps. Our goal is to try to derive the physical parameters and the chemical abundances of the

sub–clumps. In fact, this is quite difficult because we have detected only one transition in each molecule. However, we have obtained from Prof. Bachiller other Plateau de Bure data of the blue lobe of L1157 containing HCN (1–0), CH_3OH (2_K–1_K), HC_3N (11–10) and OCS (7–6) transitions. These data have been collected by Dr. Pérez–Gutiérrez in his PhD thesis but they have never been published in a journal. We are confident that using the multi–species analysis and applying the method used for CB3 we will be able to constrain the different physical conditions among the sub–clumps detected in the L1157 outflows. Indeed, the work done on CB3 has proved that the coupling of the chemical and the radiative transfer models is a powerful tool in constraining the physical and chemical parameters of the gas.

Our original goal was to derive an estimate of the gas density from the CS (2–1) and (5–4) transitions. This is not possible because the (5–4) data are not usable. Nevertheless, we have data for other species, such as HCN, that like CS are high density tracers and that can be useful. An estimate of the temperature will be possible from the four detected lines of the hyperfine transitions (2_K–1_K) of CH_3OH. In fact, the radiative transfer code that we used for CB3 did not take into account the fact that the lines are blended because they are close in wavelength and broad. Dr. Yates and Dr. Gray have modified the SMMOL code in order to take into account the effects of line–overlap (Gray & Yates, in prep) so this new code will be used in our analysis.

L1157 outflow has been selected to be observed by two of the guaranteed time Key Projects of the Herschel satellite and the chemical modelling that we will do will be extensively used in this framework in particular for the prediction of the line emission.

In these last three years I have been heavily involved in the Herschel mission, a cornerstone of the European Space Agency (ESA), both with a technical and a scientific role. In particular, I have worked on the planning of three of the guaranteed time Key Projects of star formation: "Unbiased spectral survey of star forming regions", "Water in star forming regions", and "A wide–field photometric survey of nearby star forming cloud complexes". In the following subsections I will briefly present the instruments onboard the satellite and the

scientific projects where I am involved.

6.2.1 Herschel Space Observatory

Herschel is the far–infrared and submillimetre satellite that will be launched in the early 2008. The satellite has a telescope of 3.5 m aperture working at the diffraction limit, and three instruments at the focal plane.

- PACS (Photodetector Array Camera and Spectrometer) composed of a bolometric camera with three bands centered at 75, 110 and 170 μm and a photoconductor imaging spectrometer covering the spectral range between 57 and 210 μm at medium resolution (R = 1000 - 5000).
- HIFI (Heterodyne Instrument for the Far–Infrared) a heterodyne spectrometer of high spectral resolution (up to R = 10^7) covering the spectral range between 157 and 625 μm.
- SPIRE (Spectral and Photometric Imaging Receiver) a bolometer camera for the simultaneous observation of three bands centered at 250, 350 and 500 μm and an imaging Fourier Transformer Spectrometer (FTS) covering the range between 200 and 670 μm with low resolution (R = 20 - 1000).

6.2.2 Unbiased spectral survey of star forming regions Key Project

The Key Project called "Unbiased spectral survey of star forming regions" is aimed at having an inventory of the most abundant molecular species in star forming regions in order to study the gas chemical composition as function of the evolutionary state and the mass. As we have extensively stated in this thesis the chemical composition of the gas is a powerful tool to probe the physical conditions in star forming regions. The project foresees to use the two spectrometers on–board, HIFI and PACS, to observe the spectral range between 55 to 620 μm, in a relatively small, but well selected sample of objects, representing the most important classes of star formation, i.e. pre–stellar cores,

low–mass Class 0 and Class I protostars, intermediate–mass Class 0 protostars, embedded Herbig Ae/Be stars and outflows. The results of these observations will provide a legacy database to guide follow up observations with Herschel. See Ceccarelli et al. (2006) for a detailed description of the project.

As a typical chemically rich outflow from Class 0 protostar, L1157 has been selected and our interferometric observations have been used to define the best coordinates for the pointing. Indeed the B1 clump in the blue lobe will be observed. My major contribution has consisted in defining the best PACS observing mode for this project. There are several possibilities to cover the full PACS wavelength range with different spectral sampling and sensitivity. An estimate of the observing times and sensitivities of the different observing modes has been performed. It turned out that to cover the full PACS spectral range at the highest spectral sampling requires too much time (about 15 hours), so the poorer Nyquist sampling has been selected. The range mode with Nyquist sampling is faster (about 50 min) and the spectral sampling can be improved by repeating the observation several times with a slightly different (a fraction of the FWHM) starting wavelength.

6.2.3 Water in star forming regions Key Project

Water is one of the most important molecules in interstellar chemistry in general, and in star forming regions in particular. A high water abundance has been found in the envelopes of protostars and in the outflows (e.g. Harwit et al. 1998, Boonman & van Dishoeck 2003, Nisini et al. 2000). This high abundance makes water a unique probe of the physical structure of star forming regions and of the fundamental chemical processes within the gas and between the gas and the grains. Water is not only chemically interesting; it plays an active role in the energy balance (e.g. Goldsmith & Langer 1978, Neufeld & Kaufman 1993, Doty & Neufeld 1997). Because water has a very large dipole moment, its emission lines can be efficient coolants of the gas, perhaps even the major one in some parts of the star forming regions. The large dipole momentum also favors the opposite effect, i.e. water molecules can heat the gas through absorption of infrared radiation followed by collisional de–excitation. It is therefore of paramount importance to study the water vapour lines and

comparing its cooling and heating efficiency quantitatively with that of other species.

The "Water in star forming regions" Key Project proposes a comprehensive set of water lines observations both with HIFI and PACS towards a large sample of protostars, covering a wide range of masses and luminosities, from the lowest to the highest mass protostars, and a large range of evolutionary stages, from the first ones represented by the pre–stellar cores to the last stages represented by the PMS stars surrounded by their protostellar disks. See van Dishoeck et al. (2006) for a detailed description of the project.

A deep study has been done for the definition of the observing strategy. In particular I worked on the comparison between PACS and HIFI spectroscopic capabilities (see Appendix A) in order to establish which is the most efficient between the two instruments in their overlapping spectral range between 157 and 210 μm

My major interest in this project is in the water observations in outflows. I have participated to the selection of the sources sample, the definition of the lines to observe and the calculation of the detailed estimate of the integration time for the selected transitions.

6.2.4 A wide–field photometric survey of nearby star forming cloud complexes Key Project

Understanding the initial conditions for individual protostellar collapse and the origin of the initial mass function (IMF), i.e. the distribution in masses of the prestellar condensations is a key and still unanswered question of modern astronomy. While IRAS, ISO and ground–based near–IR telescopes have provided a fairly complete census of Class I–III YSOs in nearby clouds, no such census exists yet for cold prestellar cores and Class 0 protostars. The Herschel imaging instruments SPIRE and PACS will provide unique tools to address this fundamental issue, because prestellar cores and Class 0 protostars emit the bulk of their luminosity between 80 and 400 μm, i.e. in the spectral range covered by the two instruments onboard Herschel.

This Key Project foresees an extensive imaging survey of the densest por-

tion of the Goult Belt complexes with SPIRE at 250 – 500 μm and PACS at 110 – 170 μm. The regions of the nearby ($d \leq 500$ pc) cloud complexes of our Galaxy with $A_v \geq 3$ mag (about 140 deg^2) will be mapped with SPIRE (filed of view of 4 × 4 arcmin^2) while with PACS that has a smaller field of view (3.5 × 1.75 arcmin^2) the zone with $A_v \geq 6$ mag will be mapped (about 80 deg^2). The sensitivity limits of the survey will permit to have a census of objects down to $M \sim 0.01$ M$_\odot$. See André et al. (2006) for a detailed description of the project.

I have been involved in planning of the project and in particular I am the leader of the team responsible for the Lupus complex. The Lupus molecular cloud complex is a very extended region located from $l \sim 335$ deg to $l \sim 348$ deg and from $b \sim 0$ deg to $b \sim 25$ deg. It is the nearest star forming region ($d \sim 150$ pc) and it is composed by nine subgroups. A detailed search of the literature has been carried out aimed at collecting up to date information on the region. Despite the fact that this regions is poorly studied – mostly because its very southern position in the sky (dec ∼ -45 deg) – surveys in the optical, NIR and millimetre are available (Hughes et al. 1994; Andreazza & Vilas-Boas 1996; Tachihara et al. 1996; Vilas-Boas et al. 2000; Nakajima et al. 2000). On the basis of these maps the most interesting zones (3 deg^2 with SPIRE and 1 deg^2 with PACS) to observe in the Lupus I, III and IV clouds have been selected.

Bibliography

Adams F.C., Lada C.J., Shu F.H., 1987, ApJ, 312, 788

André P., Ward–Thompson D., Barsony M., 1993, ApJ, 406, 122

André P., 1994, *The Cold Universe*, ed. T. Montemerle, C.J. Lada, I.F. Mirabel, J. Tran Thanh, Editions Frontieres, p. 179

André P., Saraceno P., et al., 2006, *A wide–field photometric survey of nearby star forming cloud complexes Key Project proposal*

Andreazza C.M., Vilas-Boas J.W.S., 1996, A&ASS, 116, 21

Arce H.G., Goodman A.A., 2001, ApJ, 554, 132

Arce H.G., Goodman A.A., 2002, ApJ, 575, 928

Bachiller R., Tafalla M., 1988, *The origin of stars and planetary systems*, ed. C. Lada, N.D. Kylafis, Kluwer Academic Publishers, p. 227

Bachiller R., Chernicharo J., Martín–Pintado J., Tafalla M., Lazareff B., 1990, A&A, 231, 174

Bachiller R., Martín–Pintado J., Fuente A., 1991, A&A, 243, L121

Bachiller R., Liechti S., Walmsley C.M., Colomer F., 1995, A&A, 295, L51

Bachiller R., Pérez–Gutiérrez M., 1997, ApJ, 487, L93

Bachiller R., Codella C., Colomer F., Liechti S., Walmsley C.M., 1998, A&A, 335, 266

Bachiller R., Pérez Gutierrez M., Kumar M.S.N., Tafalla M., 2001, A&A, 372, 899

Bally J., Lada C.J., 1983, ApJ, 265, 824

Bates D.R., Spitzer L., 1951, ApJ, 113, 441

Behrend R., Maeder A., 2001, A&A, 373, 190

Benedettini M., Yates J.A., Viti S., Codella C., 2006, MNRAS, 370, 229

Benson P.J., Myers P.C., 1989, ApJSS, 71, 89

Bergin E.A., Langer W.D., Goldsmith P.F., 1995, ApJ, 441, 222

Bergin E.A., Langer W.D., 1997, ApJ, 486, 316

Bergin E. A., Neufeld D. A., Melnick G. J., 1999, ApJ, 499, 777

Bergin E.A., Alves J., Huard T., Lada C.J., 2002, ApJ, 570, L101

Bernes C., 1979, A&A, 73, 67

Beuther H., Schilke P., Sridharan T.K., Menten K.M., Walmsley C.M., Wyrowski F., 2002a, A&A, 383, 892

Beuther H., Schilke P., Gueth F., McCaughrean M., Andersen M., Sridharan T.K., Menten K.M., 2002b, A&A, 387, 931

Beuther H., Schilke P., Stanke T., 2003, A&A, 408, 601

Black J.H., 1994, *The first symposium on the infrared cirrus and diffuse interstellar clouds*, ed. Cutri R.M., Latter W.B., ASP Conf. Ser. Vol. 58, p. 355

Blake G.A., Sandell G., van Dishoeck E.F., Groesbeck T.D., Mundy L.G., Aspin C., 1995, ApJ, 441, 689

Bonnell I.A., Bate M.R., 2002, MNRAS, 336, 659

Bontemps S., Andre P., Terebe, S., Cabrit S., 1996, A&A, 311, 858

Boonman A.M., van Dishoeck E. F., 2003, A&A, 403, 1003

Bourke T.L., Garay G., Lehtinen K.K., et al., 1997, ApJ, 476, 781

Cabrit S., Bertout C., 1986, ApJ, 307, 313

Cabrit S., Bertout C., 1992, A&A, 261, 276

Cardelli J.A., Meyer D.M., Jura M., Savege B.D., 1996, ApJ, 467, 334

Carlsson M., 1986, Upps. Astron. Obs., Rep. 33

Caselli P., Hasegawa T.I., Herbst E., 1994, ApJ, 421, 206

Caselli P., Walmsley C.M., Tafalla M., Dore L., Myers P.C., 1999, ApJ, 523, L165

Ceccarelli C., Hollenbach D.J., Tielens A.G.G.M., 1996, ApJ, 471, 400

Ceccarelli C., et al., 2006, *Unbiased spectral survey of star forming regions Key Project proposal*

Cesaroni R., Walmsley C.M., Koempe C., Churchwell E., 1991, A&A, 252, 278

Cesaroni R., Neri R., Olmi L., Testi L., Walmsley C.M., Honfer P., 2005, A&A, 434, 1039

Charnley S.B., Tielens A.G.G.M., Millar T.J., 1992, ApJ, 399, L71

Charnley S.B., 1997, ApJ, 481, 396

Charnley S.B., Rodgers S.D., Ehrenfreund P., 2001, A&A, 378, 1024

Chiar J.E., Gerakines, P.A., Whittet D.C.B., et al., 1998, ApJ, 498, 716

Codella C., Bachiller R., Reipurth B, 1999a, A&A, 343, 585

Codella C., Bachiller R., 1999b, A&A, 350, 659

Codella C., Scappini F., Bachiller R., Benedettini M., 2002, MNRAS, 331, 893

Codella C., Bachiller R., Benedettini M., Caselli P., Viti S., Wakelam V., 2005, MNRAS, 361, 244

Coffey D., Bacciotti F., Woitas J., Ray T.P., Eislöffel J., 2004, Ap&SS, 292, 553

Collings M.P., Anderson M.A., Chen R., et al., 2004, MNRAS, 354, 1133

Doty S.D., Neufeld D.A., 1997, ApJ, 489, 122

Doty S.D., Schöier F.L., van Dishoeck E.F., 2004, A&A, 418, 1021

Dougados C., Cabrit S., Lavalley C., Menard F., 2000, A&A, 357, L61

Draine B.T., Roberge W.G., Dalgarno A., 1983, ApJ, 264, 485

Dutrey A., Guilloteau S., Bachiller R., 1997, A&A, 317, L55

Edwards S., Snell R.L., 1982, ApJ, 261, 151

Edwards S., Snell R.L., 1983, ApJ, 270, 605

Edwards S., Snell R.L., 1984, ApJ, 281, 237

Falle S.A.E.G., Hartquist T.W., 2002, MNRAS, 329, 195

Fiege J.D., Henriksen R.N., 1996, MNRAS, 281, 1005

Garrod R. T., Williams D. A., Hartquist T. W., Rawlings J. M. C., Viti S., 2005, MNRAS, 356, 654

Giannini T., Lorenzetti D., Tommasi E., et al., 1999, A&A, 346, 617

Giannini T., Nisini B., Lorenzetti D., 2001, ApJ, 555, 40

Goldsmith P. F., Langer W.D., 1978, ApJ, 22, 881

Guellin M., Langer W.D., Wilson R.W., 1982, A&A, 107, 107

Gueth F., Guilloteau S., Bachiller R., 1996, A&A, 307, 891

Gueth F., Guilloteau S., Bachiller R., 1998, A&A, 333, 287

Gueth F., Guilloteau S., 1999, A&A, 343, 571

Harper G.M., 1994, MNRAS, 268, 894

Harwit M., Neufeld D.A., Melnick G., Kaufman M.J., 1998, ApJ, 497, L105

Hatchell J., Thompson M.A., Millar T.J., MacDonald G.H., 1998, A&A, 338, 713

Hatchell J., Viti S., 2002, A&A, 381, L33

Herbst E., Klemperer W., 1973, ApJ, 185, 505

Herbst E., Chang Q., Cuppen H.M., 2005, JPh Conference Serires, 6, 18

Hirth G.A., Mundt R., Solft J., 1997, A&ASS, 126, 437

Hogerheijde M.R., van der Tak F.F.S., 2000, A&A, 362, 697

Hollenbach D., McKee C.F., 1979, AJSS, 41, 555

Hollenbach D.J., Tielens A.G.G.M., 1997, Annu.Rev.A&A, 35, 179

Howe D.A., Taylor S.D., Williams D.A., 1996, MNRAS, 279, 143

Huges J., Hartigan P., Krautter J., Kelemen J., 1994, AJ, 108, 1071

Jijina J., Nyera P.C., Adams F.C., 1999, ApJSS, 125, 161

Jørgesen J.K., Schöier F.L., van Dishoeck E.F., 2004, A&A, 416, 603

Jørgesen J.K., Schöier F.L., van Dishoeck E.F., 2005, A&A, 437, 501

Juvela M., 1997, A&A, 322, 943

Kalenskii S.V., Dzura A.M., Booth R.S., Winnberg A., Alakoz A.V., 1997, A&A, 321, 311

Kramer C., Alves J., Lada C.J., Lada E.A., et al., 1999, A&A, 342, 257

Krumholz M.R., McKee C.,F., Klein R.I., 2005, ApJ, 618, L33

Kwan J., Scoville N., 1976, ApJ, 210, L39

Lada C.J., Wilking B.A., 1984, ApJ, 287, 610

Lada C.J., 1985, ARAA, 23, 267

Langer W.D., Castes A., Lefloch B., 1996, ApJ, 471, 111

Launhardt R., Henning T., 1997, A&A, 326, 329

Lavalley–Fouquet C., Cabrit S., Dougados C., 2000, A&A, 356, L41

Lerate M.R., Barlow M., Swinyard B.M., et al., in preparation

Leurini S., Schilke P., Menten K.M., Flower D.R., Pottage J.T., Xu L.H., 2004, A&A, 422, 573

Levreault R.M., 1988, ApJSS, 67, 283

Lintott C.J., Viti S., Williams D.A., Rawlings J.M.C., Ferreras I., 2005, MNRAS, 360, 1527L

Lizano S., Shu F.H., 1989, ApJ, 342, 834

Martin–Píntado J., Bachiller R., Fuente A., 1992, A&A, 254, 315

Masson C.R., Chernin L.M., 1993, ApJ, 414, 230

Mathis J.S., 1990, ARA&A, 28, 48

McCaughrean M.J., Rayner J.,T., Zinnecker H., 1994, ApJ, 436, 189

McKee C.F., 1999, *The origin of stars and planetary system*, ed. C.L. Lada and N.D. Kylafis, Kluwer Accademic Publishers, Serie C Vol. 540, 29

Mellema G., Adam F., 1997, MNRAS, 292, 795

Menten K.M., Walmsley C.M., Henkel C., Wilson T.L., 1988, A&A, 198, 253

Mestel L., Spitzer L., 1956, MNRAS, 116, 505

Millar T.J., Nejad L.A.M., 1985, MNRAS, 217, 507

Millar T.J., Rawlings J.M.C., Bennett A., Brown P.D., Charnley S.B., 1991, A&ASS, 87, 585

Millar T.J., Farquhar P.R.A., Willacy K., 1997, A&ASS, 121, 139

Millar T. J., Hatchell J., 1998, Faraday Discussions n. 109, *Chemistry and Physics of Molecules and Grains in Space*, p. 15

Mizuno A., Onishi T., Hayashi T., Oshashi N., Sunada K., Hasegawa T., Fukui Y., 1994, Nature, Vol. 368, no. 6473, 719

Molinari S., Testi L., Rodríguez L.F., Zhang Q., 2002, ApJ, 570, 758

Morata O., Estalella R., Lopez R., Planesas P., 1997, MNRAS, 292, 120

Morata O., Girart J. M., Estalella R., 2003, A&A, 397, 181

Moriarty–Schieven G.H., Snel R.L., 1988, ApJ, 332, 364

Müller H.S.P., Thorwirth S., Roth D.A., Winnewisser G., 2001, A&A, 370, L49

Mundy L.G., Looney L.W., Welch W.J., 2000, *Protostars and Planetes IV*, ed. Mannings V., Boss A.P., Russell S.S., University of Arizzona Press, p. 355

Myers P.C., 1991, *Fragmentation of molecular clouds and star formation*, ed. E. Falagarone F. Boulanger, G. Duvert, Kluwer Accademic Publishers, p. 221

Myers P.C., Fuller G.A., Goodman A.A., Benson P.J., 1991, ApJ, 376, 561

Myers P.C., 1995, *Molecular Clouds and star formation*, ed. C. Yuand and J.H. You, World Scientific, p. 47

Nakajima Y., Tamura M., Oasa Y., Nakajima T., 2000, AJ, 119, 873

Nakano T., 1979, PASJ, 31, 697

Neufeld D.A., Kaufman M.J., 1993, ApJ, 413, 145

Nisini B., Benedettini M., Giannini T., Codella C., Lorenzetti D., di Giorgio A.M., Richer J.S., 2000, A&A, 360, 297

Nisini B., Giannini T., Lorenzetti D., 2002, ApJ, 574, 246

Ohashi M., Irvine W.M., Kaifu N., 1992, *Astrochemistry of cosmisc phenomena*, ed. Sing D., Kluwer Academic Publishers, IAU Symp., 150, 171

Ossenkopf V., Trojan C., Stutzki J., 2001, A&A, 378, 608

Pastor J., Buj J., EstalellaR., Lopez R., Anglada G., Planesas P., 1991, A&A, 252, 320

Pérez–Gutiérrez M., 1999, *Química de choques en al fluio bipolar L1157*, Ph.D. Thesis, Universidad Complutense, Madrid

Pickett H.M., Poynter R.L., Cohen E.A., et al., 1998, J. Quant. Spectrosc. & Rad. Transfer, 60, 883

Pineau des Forêts G., Roueff E., Schilke P., Flower D., 1993, MNRAS, 262, 915

Pineau des Forêts G., Flower D.R., Chièze J.P., 1997, IAUS, 182, 199

Pratap P., Dickens J.E., Snell R.L., et al., 1997, ApJ, 486, 862

Raga A.C., Cabrit S., 1993, A&A, 278, 267

Rawling J.M.C., Hartquist T.W., Menten K.M., Williams D.A., 1992, MNRAS, 255, 471

Rawling J.M.C., Yates J.A., 2001, MNRAS, 326, 1423

Redman M.P., Viti S., Cau P., Williams D.A., 2003, MNRAS, 345, 1291

Richer J.S., Shepherd D.S., Cabrit S., Bachiller R., Churchwell E., 2000, *Protostars and Planetes IV*, ed. Mannings V., Boss A.P., Russell S.S., University of Arizzona Press, p. 867

Rothman L.S., Barbe A., Chris Benner D., et al., 2003, J. Quant. Spectrosc. & Rad. Transfer, 82, 5

Rowan–Robinson M., 1980, ApJS, 44, 403

Ruffle D. P., Hartquist T. W., Caselli P., Williams D. A., 1999, MNRAS, 306, 691

Rybicki G.B., Hummer D.G., 1991, A&A, 245, 171

Saniago-Garcia J., Tafalla M., Johnstone D., Bachiller R., 2006a, *Science with ALMA: a new era for astrophysics*, Madrid 13–17 November 2006

Saniago-Garcia J., Tafalla M., Bachiller R., 2006b, *Science with ALMA: a new era for astrophysics*, Madrid 13–17 November 2006

Saraceno P., André P., Ceccarelli C., Griffin M., Molinari S., 1996 ,A&A, 309, 827

Scharmer G.B., Carlsson M., 1985, *Progress in stellar spectral line formation theory*, Dordrech, D. Reidel Publishing Co., p. 189

Schöier F.L., Jørgesen J.K., van Dishoeck E.F., Blake G.A., 2002, A&A, 390, 1001

Schöier F.L., van der Tak F.F.S., van Dishoeck E.F., Black J.H., 2005, A&A, 432, 369

Shepherd D., Churchwell E., Wilner D.J., 1997, ApJ, 482, 355

Shepherd D., 2003, *Galactic star formation across the stellar mass spectrum*, ed. J.M. De Buizer, N.S. van der Bliek, Astronomical Society of the Pacific, p. 333

Shinn J.H., Seon, K.I., Lee D.H., Min K.W., 2004, IAUS, 217, 192

Shu F.H., 1977, ApJ, 214, 488

Shu F.H., Ruden S.P., Lada C.J., Lizano S., 1991, ApJ, 370, L31

Snell R.L., Howe J.E., Ashby M.L.N., et al., 2000, ApJ, 539, L101

Sofia U.J., Meyer D.M., 2001, AAS, 33, 1438

Sonnentrucker P., Friedman S.D., Welty D.E., York D.G., Snow T.P., 2002, AAS, 34, 767

Spitzer L.J., 1978, *Physical process in the Interstellar Medium*, New York, Wilay

Suzuki H., Yamamoto S., Ohishi M., et al., 1992, ApJ, 392, 551

Tachihara K., Dobashi K., Mizuno A., Ogawa H., Fukui Y., 1996, PASJ, 48, 489

Tafalla M., 1993, *Dense gas around bipolar outflow sources*, Ph.D. Thesis, University of California, Berkely

Tafalla M., Bachiller R., 1995, ApJ, 443, L37

Tafalla M., Myers P. C., Caselli P., Walmsley C. M., Comito C., 2002, ApJ, 569, 815

Tafalla M., Myers P.C., Caselli P., Walmsley C.M., 2004, Ap&SS, 292, 347

Tan J.C., McKee C.F., 2002, *Hot star workshop III: the earliest stages of massive star birth*, ed. P.A. Crowther, ASP Conference Proceedings, 267, 267

Taylor S.D., Morata O., Williams D.A., 1996, A&A, 313, 269

Teixeira T.C., Enerson J.P., Palumbo M.E., 1998, A&A, 330, 711

Umemoto T., Iwata T., Fukui Y., et al., 1992, ApJ, 392, L83

van Dishoeck E.F., Blake G.A., 1998, Annu.Rev.A&A, 36, 317

van Dishoeck E. W., 1998, *The Molecular Astrophysics of Stars and Galaxies*, ed. T. W. Hartquist, D. A. Williams, Clarendon Press, Oxford, p. 53

van Dishoeck E.F., et al., 2006, *Water in star forming regions Key Project proposal*

van Zadelhoff G.J., Dullemond C.P., van der Tak F.F.S., et al., 2002, A&A, 395, 373

Vilas-Boas J.W.S., Myers P.C., Fuller G.A., 2000, ApJ, 532, 1038

Viti S., Williams D.A., 1999a, MNRAS, 310, 517

Viti S., Williams D.A., 1999b, MNRAS, 305, 755

Viti S., Caselli P., Hartquist T.W., Williams D.A., 2001, A&A, 370, 1017

Viti S., Natarajan, S., Williams D.A., 2002, MNRAS, 336, 797

Viti S., Girart J. M., Garrod R., Williams D. A., Estalella R., 2003, A&A, 399, 187

Viti S., Codella C., Benedettini M., Bachiller R., 2004, MNRAS, 350, 1029

Wakelam V., Caselli P., Ceccarelli C., Herbst E., Castes A., 2004, A&A, 422, 159

Wakelam V., Ceccarelli C., Castes A., Lefloch B., Loinard L., Faure A., Schneider N., Benayoun J., 2005, A&A, 437, 149

Walmsley C.M., Pineau des Forêts G., Flower D.R., 1999, A&A, 342, 542

Wootten H.A., Loren R.B., Snell R.L., 1982, ApJ, 255, 160

Yorke H.W., Sonnhalter C., 2002, ApJ, 569, 846

Yun J.L, Clemens D.P., 1995, AJ, 109, 742

Zhang Q., Ho P.T.P., Wright M.C.H., Wilner D.J., 1995, ApJ, 451, L71

Zhang Q., Ho P.T.P., Wright M.C.H., 2000, AJ, 119, 1345

Zhang Q., Hunter T.R., Brand J., Sridharan T.K., Molinari S., Kramer M.A., Cesaroni R., 2001, ApJ, 552, 167

Zuckerman B., Kuiper T.B.H., Rodriguez Kuiper E.N., 1976, ApJ, 209, L137

Appendix A

A comparison between HIFI and PACS spectroscopic capabilities.

One of the first question that people asked when started planning the spectroscopic scientific projects with Herschel was which was the best instrument to use between PACS and HIFI. In fact, the two instruments have a complementary spectral range but a small overlapping wavelength range between 157 and 210 μm and a different spectral resolution. In the following their spectroscopic capabilities are compared in order to establish which is the most efficient in the overlapping spectral range.

This work was done in 2004 when the sensitivity of the instruments was not well defined and the way how to do the measurement was still under development. This means that all the overheads, such as the time for pointing, calibration, line tuning, etc., was unknown. However, the two consortia delivered a "simple time estimator" to roughly estimate the efficiency of the observation in each observing mode by adding fixed overheads to the pure integration time given by the sensitivity.

The HIFI time estimator was simply the classical formula connecting the rms noise to the integration time. The rms noise level is calculated by the formula:

$$T_{rms} = \frac{T_{sys}}{\sqrt{A\Delta\nu t_{tot}}} \tag{A.1}$$

where T_{sys} is the system temperature, $\Delta\nu$ is the frequency resolution in Hz, t_{tot} is the total observing time in seconds and A is an efficiency factor that

takes into account the overheads. The HIFI observing modes are: Frequency Switching, Position Switching and On The Fly (OTF) scans.

To estimate the PACS time we used a preliminary version of HSPOT V0.54, the software tool that will be distributed as a time estimator for the mission. The PACS spectroscopic observing modes are Line Spectroscopy and Range Spectroscopy.

To compare the HIFI and PACS spectroscopic capabilities in the common wavelength range (157 – 210 μm), we consider the Frequency Switching observing mode for HIFI and the Line Spectroscopy with chopping and nodding for PACS. The following strategy has been applied:

- Five different lines in the 157 – 210 μm range are considered: [CII] ($^2P_{3/2} - ^2P_{1/2}$) at 157.60 μm, OH ($\Pi_{\frac{1}{2}} 3/2 - 1/2$) at 163.20 μm, H_2O (2_{21}-1_{01}) at 179.53 μm, CO (14-13) 185.99 μm and [NII] ($^3P_1 - ^3P_0$) at 205.00 μm.

- For each line we calculate the PACS observation time to perform a single pointing observation, i.e. to observe one PACS field of view (FOV) of 47×47 arcsec^2 at a spatial resolution of 9.4 arcsec. The minimum observing time for Line Spectroscopy mode is used to reach a typical rms of 0.3 Jy which correspond to a line flux of 2×10^{-21} W cm^{-2} at signal to noise ratio (S/N) of 5 (about 10 times less than the typical line flux observed by the Long Wavelength Spectrometer on-board ISO).

- With HIFI the same region of the PACS FOV is mapped. However, since the FOV of HIFI is smaller that the PACS one at these wavelengths, several pointings are needed to observe the same area. We impose to HIFI to do the same map in the same time used by PACS observations. Frequency switching observing mode and the Wide Band Spectrometer (WBS) with 1 MHz spectral resolution are used to calculate the T_{rms}.

- In order to improve the HIFI sensitivity the spectral resolution is reduced. No advantage in the S/N can be obtained rebinning the HIFI data to a resolution higher than the linewidth, therefore the HIFI data are rebinned at the linewidth and the corresponding T_{rms} is calculated.

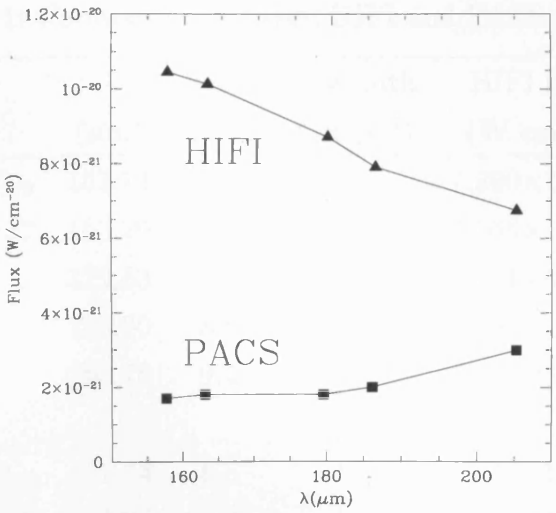

Figure A.1: Comparison between PACS ad HIFI sensitivity for a line with FWHM = 10 km s^{-1}. The HIFI data are rebined at a resolution equal to the linewidth.

- Then the correspondent line fluxes are calculated, assuming S/N = 5 and different line widths: 5, 10, 40, 80 km s^{-1}.
- Finally, we compare the line fluxes observed by HIFI and PACS in the same integration time, with the same S/N, and covering the same area in the sky.

In Table A.1 the results of the sensitivity estimates are reported. The transition and its wavelength are listed in column 1 and 2, respectively; column 3 gives the observing time; column 4 gives the linewidth; column 5 gives the line flux measured by HIFI with S/N = 5, rebing the data at a spectral resolution equal to the linewidth; column 6 lists the PACS line flux with S/N = 5. As an example in Fig. A.1 we show the comparison between PACS and HIFI line sensitivity for a line with FWHM = 10 km s^{-1}.

Some scientific programs foresee the mapping of an extended area – typical sizes are few arcmin square – this requires more than one PACS pointing. Then the comparison strategy explained before has been applied also to the PACS mapping mode. An area of 1.57×1.57 $arcmin^2$ (corresponding to 2×2

Table A.1: Comparison between HIFI and PACS sensitivities.

line	λ (μm)	Time (min)	linewidth (km s^{-1})	HIFI flux (W cm^{-2})	PACS flux (W cm^{-2})
CII $^2P_{3/2} - ^2P_{1/2}$	157.74	8.5	5	7.390×10^{-21}	1.7×10^{-21}
OH 1/2 3/2-1/2	163.20	8.3	5	7.166×10^{-21}	1.8×10^{-21}
H_2O 2_{21}-1_{01}	179.53	8.6	5	6.161×10^{-21}	1.8×10^{-21}
CO 14-13	186.00	8.8	5	5.597×10^{-21}	2.0×10^{-21}
NII $^3P_1 - ^3P_0$	205.18	9.4	5	4.774×10^{-21}	3.0×10^{-21}
CII $^2P_{3/2} - ^2P_{1/2}$	157.74	8.5	10	1.045×10^{-20}	1.7×10^{-21}
OH 1/2 3/2-1/2	163.20	8.3	10	1.013×10^{-20}	1.8×10^{-21}
H_2O 2_{21}-1_{01}	179.53	8.6	10	8.713×10^{-21}	1.8×10^{-21}
CO 14-13	186.00	8.8	10	7.916×10^{-21}	2.0×10^{-21}
NII $^3P_1 - ^3P_0$	205.18	9.4	10	6.751×10^{-21}	3.0×10^{-21}
CII $^2P_{3/2} - ^2P_{1/2}$	157.74	8.5	20	1.478×10^{-20}	1.7×10^{-21}
OH 1/2 3/2-1/2	163.20	8.3	20	1.433×10^{-20}	1.8×10^{-21}
H_2O 2_{21}-1_{01}	179.53	8.6	20	1.232×10^{-20}	1.8×10^{-21}
CO 14-13	186.00	8.8	20	1.119×10^{-20}	2.0×10^{-21}
NII $^3P_1 - ^3P_0$	205.18	9.4	20	9.556×10^{-21}	3.0×10^{-21}
CII $^2P_{3/2} - ^2P_{1/2}$	157.74	8.5	40	2.090×10^{-20}	1.7×10^{-21}
OH 1/2 3/2-1/2	163.20	8.3	40	2.027×10^{-20}	1.8×10^{-21}
H_2O 2_{21}-1_{01}	179.53	8.6	40	1.743×10^{-20}	1.8×10^{-21}
CO 14-13	186.00	8.8	40	1.583×10^{-20}	2.0×10^{-21}
NII $^3P_1 - ^3P_0$	205.18	9.4	40	1.350×10^{-20}	3.0×10^{-21}
CII $^2P_{3/2} - ^2P_{1/2}$	157.74	8.5	80	2.956×10^{-20}	1.7×10^{-21}
OH 1/2 3/2-1/2	163.20	8.3	80	2.866×10^{-20}	1.8×10^{-21}
H_2O 2_{21}-1_{01}	179.53	8.6	80	2.464×10^{-20}	1.8×10^{-21}
CO 14-13	186.00	8.8	80	2.239×10^{-20}	2.0×10^{-21}
NII $^3P_1 - ^3P_0$	205.18	9.4	80	1.909×10^{-20}	3.0×10^{-21}

Table A.2: As Table A.1 but using PACS in the mapping observing mode.

line	λ (μm)	Time (min)	linewidth (km s^{-1})	HIFI flux (W cm^{-2})	PACS flux (W cm^{-2})
CII$^2P_{3/2} - ^2P_{1/2}$	157.74	14.15	5	1.146×10^{-20}	2.5×10^{-21}
OH 1/2 3/2-1/2	163.20	13.88	5	1.101×10^{-20}	2.5×10^{-21}
H_2O 2_{21}-1_{01}	179.53	14.48	5	9.345×10^{-21}	2.6×10^{-21}
CO 14-13	186.00	14.82	5	8.780×10^{-21}	2.8×10^{-21}
NII$^3P_1 - ^3P_0$	205.18	16.02	5	7.314×10^{-21}	4.3×10^{-21}
CII$^2P_{3/2} - ^2P_{1/2}$	157.74	14.15	10	1.620×10^{-20}	2.5×10^{-21}
OH 1/2 3/2-1/2	163.20	13.88	10	1.557×10^{-20}	2.5×10^{-21}
H_2O 2_{21}-1_{01}	179.53	14.48	10	1.322×10^{-20}	2.6×10^{-21}
CO 14-13	186.00	14.82	10	1.242×10^{-20}	2.8×10^{-21}
NII$^3P_1 - ^3P_0$	205.18	16.02	10	1.034×10^{-20}	4.3×10^{-21}
CII$^2P_{3/2} - ^2P_{1/2}$	157.74	14.15	20	2.291×10^{-20}	2.5×10^{-21}
OH 1/2 3/2-1/2	163.20	13.88	20	2.202×10^{-20}	2.5×10^{-21}
H_2O 2_{21}-1_{01}	179.53	14.48	20	1.869×10^{-20}	2.6×10^{-21}
CO 14-13	186.00	14.82	20	1.756×10^{-20}	2.8×10^{-21}
NII$^3P_1 - ^3P_0$	205.18	16.02	20	1.464×10^{-20}	4.3×10^{-21}
CII$^2P_{3/2} - ^2P_{1/2}$	157.74	14.15	40	3.240×10^{-20}	2.5×10^{-21}
OH 1/2 3/2-1/2	163.20	13.88	40	3.114×10^{-20}	2.5×10^{-21}
H_2O 2_{21}-1_{01}	179.53	14.48	40	2.643×10^{-20}	2.6×10^{-21}
CO 14-13	186.00	14.82	40	2.483×10^{-20}	2.8×10^{-21}
NII$^3P_1 - ^3P_0$	205.18	16.02	40	2.069×10^{-20}	4.3×10^{-21}
CII$^2P_{3/2} - ^2P_{1/2}$	157.74	14.15	80	4.582×10^{-20}	2.5×10^{-21}
OH 1/2 3/2-1/2	163.20	13.88	80	4.403×10^{-20}	2.5×10^{-21}
H_2O 2_{21}-1_{01}	179.53	14.48	80	3.738×10^{-20}	2.6×10^{-21}
CO 14-13	186.00	14.82	80	3.512×10^{-20}	2.8×10^{-21}
NII$^3P_1 - ^3P_0$	205.18	16.02	80	2.926×10^{-20}	4.3×10^{-21}

PACS pointings with a step of 47 arcsec in both x and y directions) has been considered. In Table A.2 we show the results in the same format as in Table A.1.

Looking at the two Tables A.1 and A.2 the main conclusion are:

- PACS has a better sensitivity with respect to HIFI over all the considered wavelength range, being the observation time, S/N and covered area the same (compare the last two columns of Table A.1 and A.2).
- The difference between the HIFI and the PACS line flux sensitivity decreases as the wavelength increases.
- For HIFI the best flux limit is reached for the narrow lines (because the flux is spread over a lower number of channels).
- If one wants to map a large area and thus to use PACS in the Line Mapping mode, the differences between the two instruments is similar to the case of Line Spectroscopy observing mode.
- Since the PACS spectral resolution in the considered wavelength range is 140 – 240 km s^{-1}, most of the lines observed with PACS will be unresolved whereas with HIFI, even if we rebin the data we can have a rough estimate of the linewidth.
- For lines at $\lambda > 200$ μm, the HIFI line flux is higher than PACS line flux of a factor of 2 – 6 (depending on the line with) while the difference became as large as a factor 18 for the broadest lines at 157 μm.

Recently new versions of the time estimator for the two instruments have been relised. Then in few cases the above estimates have been recalculated. Although the numbers are slightly different, the final conclusion that PACS is most efficient instrument is still valid.